Turbulence without vortex stretching

Tong Wu

N° d'ordre NNT: 2023ECDL0038

THÈSE DE DOCTORAT DE L'UNIVERSITÉ DE LYON

opérée au sein de

L'ÉCOLE CENTRALE DE LYON

ÉCOLE DOCTORALE No.162 MEGA

Mécanique, Énergétique, Génie civil, Acoustique

Spécialité: Mécanique des Fluides

Soutenue publiquement le 16/10/2023 par :

Tong WU

Turbulence without vortex stretching

Devant le jury composé de:

Bos Wouter	Directeur de Recherche CNRS	Directeur de Thèse
Musacchio Stefano	Professeur, Université de Torino	Rapporteur
Plunian Franck	Professeur, Université Grenoble-Alpes	Rapporteur
Canet Léonie	Professeure, Université Grenoble-Alpes	Examinateur
Herbert Corentin	Chargé de Recherche CNRS	Examinateur
Lévêque Emmanuel	Directeur de Recherche CNRS	Examinateur
Fang Le	Professeur, Université de Beihang	Examinateur invité

Acknowledgements

Acknowledgements

First and foremost, I would like to express my profound gratitude to my supervisor, Wouter Bos. His guidance and mentorship throughout my doctoral research journey have been invaluable. His approach to research, driven by a deep-seated interest and love for scientific exploration, has left a significant mark on my own perspective toward research. Not only has he enlightened me with his clear explanations of complex problems and important theoretical knowledge of turbulence, but his enthusiasm for scientific discovery has been a guiding light that has deeply influenced me. Additionally, his extensive support was instrumental in my application for a postdoctoral position, for which I am profoundly grateful.

I am fortunate to have worked with a group of exceptional colleagues who have made this journey both insightful and enjoyable. Wesley Agoua, the first colleague I met upon joining the lab, deserves special mention for his infectious enthusiasm and companionship that enabled me to swiftly integrate into the laboratory environment. I am thankful for his efforts in enriching my doctoral life, both within and outside the lab.

I would also like to extend my heartfelt thanks to my colleagues Bruce Yin, Ryo Araki, Smiron Varghese, and Henri Lam, a graduate Ph.D. of our group. Bruce helped me to correct a crucial problem in the vorticity equation, the divergence-free condition of the vorticity. Ryo's dedication to his work has been a constant source of inspiration, motivating me to strive for excellence. Smiron's companionship has been enriching my research life. Henri assisted me with running the code of our lab.

I also wish to extend my gratitude to Professor Le Fang, my master's supervisor, whose recommendation led me to this lab and whose guidance was essential to my project on

turbulence.

I extend my appreciation to Doctors Tomos David and Antoine Venaille, who provided me invaluable insights on point-vortex statistical mechanics theory and pertinent references on statistical mechanics applied to turbulence, respectively. Additionally, I am grateful to Professor Joachim Peinke for our collaboration on the project of turbulence in an elongated domain.

I extend my deepest gratitude to Professor Musacchio, who agreed to serve as one of the reporters for my thesis amidst his busy schedule. Immense thanks go to Professor Plunian, the other esteemed reporter on my committee. I am also profoundly thankful to Professor Canet, Doctor Herbert and Doctor Lévêque for agreeing to be a member of the jury.

A special acknowledgment goes to the IT department, particularly Pouilloux Laurent and Anne Cadiou, for their technical assistance.

I am extremely grateful to the China Scholarship Council for their support of my doctoral research. Furthermore, I would like to extend my gratitude to the staff maintaining the facilities of the PMCS2I (cluster of École Centrale de Lyon) and IDRIS (French national cluster), where simulations of my thesis were conducted.

Dedication

I dedicate this work to my parents, who have provided unfailing spiritual support throughout my life. Their unwavering respect for my choices and their complete support as I grew up has been invaluable. Despite their worries about me pursuing a Ph.D. abroad, a path they have never taken, they chose to support me unconditionally. For this, my gratitude is immeasurable.

To Bowen Yang, I express my heartfelt thanks for his constant company and support. Despite the geographical distance with him in Austria and me in France, our daily video calls discussing life and work have been a source of comfort and strength. As the first person I share both joys and sorrows with, his spiritual support has been instrumental in helping me navigate the challenges of living and studying in a foreign country.

I am immensely grateful to my Chinese friends in France, whose help and companionship have been a beacon of warmth and familiarity. Our shared meals every Spring Festival have been a taste of home, for which I am deeply thankful.

A special thanks to Gaopan Kong, whom I had the pleasure of meeting at the 14th European Fluid Mechanics Conference. His assistance in spreading the word about my work

on social media has been greatly appreciated.

Lastly, I would like to express my gratitude to ChatGPT. ChatGPT has significantly enhanced my essay writing efficiency by helping polish the language and correct grammatical errors. I consider myself extremely fortunate to be part of the first generation of witnesses to this AI era.

Abstract

Vortex stretching is widely acknowledged as a vital part of the energy cascade in three-dimensional (3D) turbulence. We examine the influence of this vortex-stretching mechanism by eliminating it and comparing the resultant system with standard turbulence.

First, we explore the dynamics of the spectrally truncated system without viscosity. We employ tools from statistical mechanics to predict the energy, helicity, and enstrophy spectra at the absolute equilibrium state and later validate these analytical predictions through simulations. We find two inviscid invariants: enstrophy and helicity. In the absence of helicity, an equipartition of enstrophy is detected at the final equilibrium state. In contrast, in a helical system, most helicity (and energy) is concentrated at the first mode in Fourier space, suggesting the final state can be interpreted as an Arnold–Beltrami–Childress flow.

In the second part, we investigate cascades associated with nonlinear transfer. It is shown that enstrophy cascades from larger to smaller scales, while helicity undergoes an inverse cascade towards larger scales. Dimensional analysis allows us to derive scaling laws for the energy spectrum. In the inertial range of the enstrophy cascade, the energy spectrum $E(k)$ is proportional to k^{-3}, and for the helicity cascade, $E(k)$ is proportional to $k^{-7/3}$.

In the third part, we investigate large-scale structure formation. Since helicity undergoes an inverse cascade towards larger scales and carries energy, the absence of large-scale friction leads to a state characterized by a condensation structure. We generalize a point-vortex model to predict a hyperbolic sine relationship between vorticity and velocity during this condensation state. Both forced and freely-decaying cases are assessed through direct numerical simulations, confirming the predicted functional relationship.

Lastly, we investigate spectrally truncated two-dimensional three-component (2D3C) flows using statistical mechanics and numerical simulations. In particular, we find that helicity determines the large-scale behavior of the energy distribution of the third velocity component.

Résumé

L'étirement de vorticité est largement reconnu comme une partie essentielle de la cascade d'énergie dans la turbulence tridimensionnelle (3D). Nous examinons l'influence de ce mécanisme d'étirement de vorticité en l'éliminant et en comparant le système résultant avec la turbulence non-modifiée.

D'abord, nous explorons la dynamique du système tronqué spectralement sans viscosité. Nous utilisons des outils de la mécanique statistique pour prédire les spectres d'énergie, d'hélicité et d'enstrophie à l'état d'équilibre absolu, puis validons ces prédictions analytiques à travers des simulations. Nos résultats révèlent l'existence de deux invariants non visqueux : l'enstrophie et l'hélicité. En l'absence d'hélicité, une équipartition de l'enstrophie est observée. En revanche, dans un système hélicoïdal, la plupart de l'hélicité (et de l'énergie) est concentrée sur le premier mode dans l'espace de Fourier, suggérant que l'état final peut être interprété comme un écoulement Arnold–Beltrami–Childress.

Dans la deuxième partie, nous étudions les cascades associées au transfert non linéaire. Il est démontré que l'enstrophie est transférée des échelles plus grandes vers les plus petites, tandis que l'hélicité subit une cascade inverse vers les échelles plus grandes. L'analyse dimensionnelle nous permet de déduire les lois d'échelle du spectre d'énergie. Dans la zone inertielle de la cascade d'enstrophie, le spectre d'énergie $E(k)$ est proportionnel à k^{-3}, et pour la cascade d'hélicité, $E(k)$ est proportionnel à $k^{-7/3}$.

Dans la troisième partie, nous étudions la formation de structures à grande échelle. Comme l'hélicité subit une cascade inverse vers des échelles plus grandes et transporte de l'énergie, l'absence de friction à grande échelle conduit à un état caractérisé par une structure de condensation. Nous généralisons un modèle de vortex ponctuel pour prédire une relation fonctionnelle de la forme d'un sinus hyperbolique entre la vorticité et la vitesse durant cet état de condensation. Les cas forcés et en décroissance libre sont évalués par des simulations

numériques directes, confirmant la relation prédite.

Enfin, nous étudions les écoulements bidimensionnels à trois composants (2D3C) en utilisant la mécanique statistique et les simulations numériques. En particulier, nous constatons que l'hélicité détermine le comportement à grande échelle de la distribution d'énergie de la troisième composante de vitesse.

Contents

Nomenclature

α, β	Lagrange multipliers
$\boldsymbol{\omega}$	Vorticity vector
$\boldsymbol{a}, \boldsymbol{b}$	Arbitrary and homogeneous vector fields
$\boldsymbol{d}$	Damping term in physical space
$\boldsymbol{e}_z$	Unit vector in z-direction
$\boldsymbol{f}$	External force in physical space
$\boldsymbol{g}, \boldsymbol{h}$	Arbitrary, homogeneous and incompressible vector fields
$\boldsymbol{k}$	Wave vector
$\boldsymbol{u}$	Velocity vector
$\boldsymbol{u}_a, \boldsymbol{u}_b, \boldsymbol{u}_c$	Velocity fields
$\hat{\boldsymbol{\omega}}$	Fourier coefficient associated with the vorticity
$\hat{\boldsymbol{u}}$	Fourier coefficient associated with the velocity
S	Strain-rate tensor
S^F	Filtered strain-rate tensor
$\boldsymbol{h}_+, \boldsymbol{h}_-$	Bases of helical-mode decomposition

$\boldsymbol{k}_n$	The nth Wave vector
$\boldsymbol{r}_i$	Position of cell i
ϵ	Energy dissipation rate
ϵ_H	Helicity dissipation rate
ϵ_H^μ	Helicity dissipation rate associated with the large-scale friction
ϵ_H^ν	Helicity dissipation rate associated with the hyperviscous damping
ϵ_W	Enstrophy dissipation rate
ϵ_W^μ	Enstrophy dissipation rate associated with the large-scale friction
ϵ_W^ν	Enstrophy dissipation rate associated with the hyperviscous damping
ϵ_{ijk}	Levi-Civita symbol
η	Kolmogorov length scale
$\hat{\boldsymbol{d}}$	Damping term in Fourier space
$\hat{\boldsymbol{f}}$	Forcing term in Fourier space
$\hat{\boldsymbol{\kappa}}$	Unit vector parallel to $\boldsymbol{k}$
$\hat{\boldsymbol{w}}$	Unit vector perpendicular to $\boldsymbol{k}$
$\hat{u}_+(\boldsymbol{k}), \hat{u}_-(\boldsymbol{k})$	Coefficients of $\hat{u}(\boldsymbol{k})$ under helical-mode decomposition
$\mathcal{L}$	Integral length scale
i	Imaginary unit
$\mathscr{W}$	Number of microstates
ν	Kinematic viscosity
ω	Vorticity
ω_i	i-component of vorticity vector

Π_H Flux of helicity

Π_W Flux of enstrophy

ρ Density

τ Characteristic time scale

A, B, C Parameters of an ABC flow

a, b Arbitrary and homogeneous scalar fields

C_n, C_E, k_0, λ Constants

$E(k)$ Kinetic energy spectrum at wavenumber k

E Kinetic energy

E_n Modal energy

$H(k)$ Helicity spectrum at wavenumber k

H Helicity

H_n Modal helicity

I Identity matrix

k Wavenumber

k_f Wavenumber where the external force is applied

$k_{\max}$ Maximum wavenumber

$k_{\min}$ Minimum wavenumber

k_μ Wavenumber where damping mechanisms is added (at large length-scales)

k_ν Wavenumber where damping mechanisms is added (at small length-scales)

L Length of side of the computational domain

M Number of point vortices

M_p Number of grid points in the p direction

$M_{i,p}^+, M_{i,p}^-$ Numbers of positive and negative point vortices in the p direction inside cell i

N Total number of modes in a truncated system

N_{grid} Number of grid points in each direction in a 3D cubic domain

N_k Number of modes in each direction in a 3D cubic domain

P Probability density

p Pressure

P_n Partial probability density for mode n

R Filter width

R_λ Taylor-scale Reynolds number

R_c Critical filter width

R_H Scale separation in the inverse helicity cascade

R_W Scale separation in the forward enstrophy cascade

R_{ij} Two-point velocity correlation

Re Reynolds number

S Entropy

S_n Function of the constants of motion

t Time

U Fourier distribution of kinetic energy

u_i i-component of velocity vector

V Total volume of the computational domain

$W(k)$ Enstrophy spectrum at wavenumber k

W Enstrophy

W_n Modal enstrophy

x_i i-component of position vector

$y_{n_1}, y_{n_2}, y_{n_3}, y_{n_4}$ Independent real coefficients describing each Fourier mode

Z_n Integral of partial probability density for mode n

Abbreviations

2D3C Two-dimensional three-component

2D Two dimensional

3D Three dimensional

DNS Direct Numerical Simulation

LHS Left-hand side

RHS Right-hand side

RMS Robert-Miller-Sommeria

Operators

$[\bullet]$ Rounding operation

$\bullet^*$ Conjugate transpose

Δ Laplace operator

$\langle\bullet\rangle$ Ensemble average

$\langle\bullet\rangle_p$ Space average in the p-direction

$\mathbb{P}$ Projection operator

$\mathcal{F}[\bullet]$ Fourier transform

$\mathrm{Im}[\bullet]$ Imaginary part of a complex number

$\mathrm{Re}[\bullet]$	Real part of a complex number
∇	Nabla operator
$\sum_k$	Spherical domain consisting of all wave vectors whose lengths are smaller than k.

List of Figures

List of Tables

Chapter 1

Introduction and outline

1.1 How does turbulence behave without vortex stretching?

Turbulence, an intricate phenomenon, manifests itself in numerous natural flows, including atmospheric [1], oceanic [2, 3], and galactic systems [4]. It plays a major role in diverse engineering applications, encompassing aerodynamics [5], wind energy systems [6, 7], and civil engineering [8]. Turbulence is characterized by unsteady, irregular, and chaotic flow involving intense energy exchange between different-sized eddies, a process referred to as the "energy cascade". In light of the widespread influence of turbulence, there is a crucial need to comprehend the intricate mechanism underlying energy cascades. Such knowledge is essential to enable more precise turbulence control, and to refine turbulence models.

The concept of the energy cascade was first introduced by Richardson [9], whose well-known verse eloquently encapsulates the energy transfer phenomenon within turbulent systems: "Big whorls have little whorls that feed on their velocity, and little whorls have smaller whorls and so on to viscosity—in the molecular sense." However, subsequent research has indicated that this assertion is not entirely precise. The energy cascade process can vary depending on the dimensionality of the turbulence, and the dynamics of two- and three-dimensional turbulence is dramatically different. In three-dimensional (3D) turbulence, kinetic energy shows the tendency to cascade towards the small scales, called the forward energy cascade [10]. In contrast, two-dimensional (2D) turbulence exhibits a tendency for energy to accumulate in large-scale vortical structures [11,12], resulting from an inverse energy cascade.

So, what drives this difference between 2D and 3D turbulence dynamics? The fundamental governing equations that describe fluid dynamics point to the vortex stretching term as a crucial differential factor. In 2D turbulence, the vortex stretching is naturally zero because the velocity gradient is perpendicular to the vorticity, which is not the case in 3D turbulence. Consequently, vortex stretching is often considered to be associated with the forward energy cascade, also referred to as the direct energy cascade in some publications. A vast body of literature has reported on the role of vortex stretching in 3D turbulence dynamics [13–22].

However, a question arises - is this different behavior between 2D and 3D turbulence a direct consequence of the change in dimension, or is it caused by the geometrical fact that, in 2D flows, the velocity gradient is perpendicular to the vorticity? In the framework of the Navier-Stokes equations, these two possibilities seem equivalent because the change from three to two dimensions leads to the suppression of vortex stretching. To disentangle this conundrum, we apply a force that compensates for the vortex-stretching term to the 3D Navier-Stokes equations and then compare the modified systems with classical 3D flows. Indeed, recently an important body of research has focused on the decimation of turbulence to investigate its dynamics [23–25]. Additionally, Kraichnan's test-field model [26] is based on the removal of a particular feature of the turbulent dynamics, the incompressibility constraint, to measure the Lagrangian decorrelation induced by pressure fluctuations.

In this thesis, we thus investigate 3D turbulence without vortex stretching. Comprehensive analytical analyses are accompanied by numerical simulations, validating the theoretical predictions.

1.2 Outline

This thesis is organized as follows:

Chapter 2 provides background knowledge of classical 3D and 2D turbulence, which helps us to investigate 3D turbulence without vortex stretching. We present the governing equations both in physical and Fourier space, highlighting the vortex-stretching term. A discussion of three important quadratic quantities—energy, enstrophy, and helicity—is undertaken, and we introduce basis concepts for investigations in Fourier space, such as energy, enstrophy, and helicity spectra. We further elaborate on two prevalent statistical methods employed in traditional turbulence research: the statistical analysis of the spectrally truncated sys-

tem and the point-vortex model. Throughout this thesis, we will adapt and generalise these statistical methods to study turbulence without vortex stretching.

In Chapter 3, we construct the theoretical framework for our study. In this chapter, we define the system to be explored in this thesis, provide the governing equation for turbulence without vortex stretching, and identify the global inviscid invariants—enstrophy and helicity—associated with this equation. This chapter also outlines the numerical method that will be applied in subsequent chapters.

In Chapter 4, we investigate turbulence without vortex stretching within an inviscid, spectrally truncated framework. Using a statistical physics approach, we estimate the final (or absolute equilibrium state) of this system, which is subsequently assessed through numerical simulations.

In Chapter 5, we explore the cascades of the two inviscid invariants (enstrophy and helicity) in viscous turbulence without vortex stretching. We begin by analytically predicting cascade directions based on the spectra at the absolute equilibrium state. Thereafter, we predict the forms of energy and helicity spectra. To validate these analytical predictions, we perform numerical simulations, and we observe a forward cascade of enstrophy and an inverse cascade of helicity.

Chapter 6 delves into the condensation of energy at large scales, caused by the inverse helicity cascade elucidated in Chapter 5. We generalise the point-vortex model to 3D turbulence and predict a hyperbolic sine relationship between vorticity and velocity. This prediction is tested through further numerical simulations.

Chapter 7 examines a two-dimensional three-component (2D3C) turbulent system where the third component is passively advected by the associated 2D flow. Given the absence of vortex stretching in the 2D component of 2D3C turbulence, this system constitutes a "real-world system" resembling turbulence without vortex stretching. We predict the final state of 2D3C turbulence in an inviscid, spectrally truncated system, and these predictions are verified through numerical simulations.

Chapter 8 presents a comprehensive conclusion of the thesis and offers perspectives on future work in this area.

1.3 Related articles

This PhD work has resulted in several journal and conference articles, which are published, submitted, or in preparation:

- Tong Wu, and Wouter JT Bos. "Statistical mechanics of the Euler equations without vortex stretching." *Journal of Fluid Mechanics* 929 (2021): A11.
- Tong Wu, and Wouter JT Bos. "Cascades of enstrophy and helicity in turbulence without vortex stretching." *Physical Review Fluids* 7.9 (2022): 094601.
- Tong Wu, Tomos David, and Wouter JT Bos. "Point-vortex statistical mechanics applied to turbulence without vortex stretching." (Submitted)
- Tong Wu, and Wouter JT Bos. "Turbulence without vortex stretching." *14th European Fluid Mechanics Conference*, 13-16 September 2022, Athens, Greece.
- Tong Wu, and Wouter JT Bos. "Point vortex statistical mechanics applied to turbulence without vortex stretching." *Réunion 2022 du GDR Navier-Stokes 2.00*, 2-4 November 2022, Lille, France.
- Tong Wu, and Wouter JT Bos. "Turbulence without vortex stretching." *Réunion 2021 du GDR Navier-Stokes 2.00*, 27-29 Octobre 2021, Paris-Saclay, France.
- Tong Wu, and Wouter JT Bos. "Turbulence without vortex stretching." *Euromech colloquium 620: Extreme dissipation and intermittency in turbulence*, 17-19 May 2021, online.

Chapter 2

Theoretical background

Before examining turbulence without vortex stretching, this section provides a necessary background of classical 2D and 3D turbulence. The methodologies used to explore classical turbulence can provide valuable insights when studying turbulence without vortex stretching.

In Section 2.1, we focus on the theoretical foundations of turbulence in physical space. We elucidate the governing equations of flow, and introduce inviscid invariants — energy and enstrophy in 2D turbulence, energy and helicity in 3D turbulence. In Section 2.2, we present the fundamental knowledge required for analyzing turbulence in Fourier space. We derive governing equations in Fourier space, explain the spectra of inviscid invariants and their fluxes, and introduce the helical decomposition method. Lastly, in Section 2.3, we introduce statistical mechanics methods applied to turbulence studies.

Moreover, we emphasize that, throughout this thesis, our focus remains on incompressible, homogeneous, and isotropic flows.

2.1 Turbulence in physical space

In this section, we first investigate the governing equations of continuity, velocity, and vorticity in physical space, and explain the fundamental differences between 2D and 3D turbulence in Subsection 2.1.1. Subsequently, in Subsection 2.1.2, we introduce several useful identities valid in statistically homogeneous flows. Finally, in Subsection 2.1.3, we provide the definitions of energy, enstrophy, and helicity, elaborate on their conservation properties in inviscid 2D or 3D turbulence.

2.1.1 Governing equations

Fluids are considered continuous media, and as such, the volume continuity equation, one of the principal governing equations, is formulated as

$$\frac{\partial \rho}{\partial t} + \nabla \cdot (\rho \boldsymbol{u}) = 0 \tag{2.1}$$

where $\boldsymbol{u}$ is the velocity, t means the time, and ρ indicates the density. Equation (2.1) represents the law of mass conservation. Throughout this thesis, we focus on incompressible fluids. For such flows, the density remains constant across time and space. Thus Eq. (2.1) simplifies to

$$\nabla \cdot \boldsymbol{u} = 0. \tag{2.2}$$

This incompressible field is also called "solenoidal" or "divergence-free". The evolution of the velocity field is governed by the well-known Navier-Stokes equation [27]

$$\frac{\partial \boldsymbol{u}}{\partial t} + (\boldsymbol{u} \cdot \nabla)\boldsymbol{u} = -\frac{1}{\rho}\nabla p + \nu \Delta \boldsymbol{u} \tag{2.3}$$

where p signifies the pressure, ν is the kinematic viscosity, and no external force is applied. Eq. (2.3) is a direct consequence of Newton's second law applied to a fluid particle. An important difference between 2D and 3D flows can be noted on the level of the governing equation of vorticity. Vorticity, which describes the local spinning motion of a fluid, is defined as the curl of the velocity. Formally, the dynamics of the vorticity $\boldsymbol{\omega}$ is governed by the curl of Eq.(2.3)

$$\frac{\partial \boldsymbol{\omega}}{\partial t} + (\boldsymbol{u} \cdot \nabla)\boldsymbol{\omega} = (\boldsymbol{\omega} \cdot \nabla)\boldsymbol{u} + \nu \Delta \boldsymbol{\omega} \tag{2.4}$$

with $\boldsymbol{\omega} = \nabla \times \boldsymbol{u}$. In the case of a 2D flow, with velocity evolving in the plane perpendicular to the z axis, the vorticity is given by $\boldsymbol{\omega} = \omega \boldsymbol{e}_z$. In this case, the vorticity vector is always perpendicular to the velocity and velocity gradients, as shown in Fig. 2.1, so that the first term on the right-hand side of Eq. (2.4) is trivially zero.

To better understand the physical implications of this term, we consider an elemental vortex tube, which is defined as a material volume moving with the fluid in such a manner that the vorticity vector remains tangent to the surface of the tube. We denote the difference of velocity between two endpoints, A and B, as $\delta \boldsymbol{u} = \boldsymbol{u}_A - \boldsymbol{u}_B$. When the angle between $\boldsymbol{\omega}$

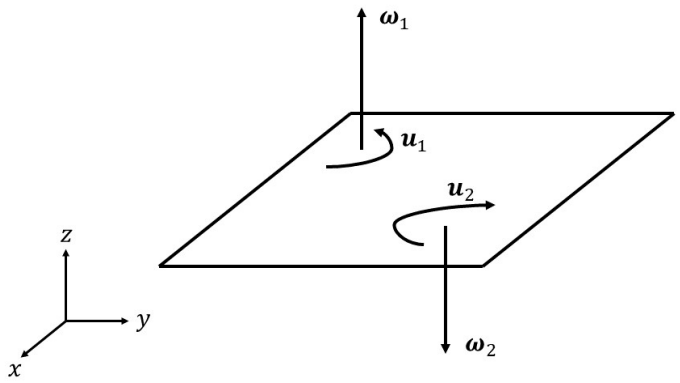

Figure 2.1: A sketch of a 2D flow. In 2D flows, vorticity is perpendicular to the velocity (and its gradients).

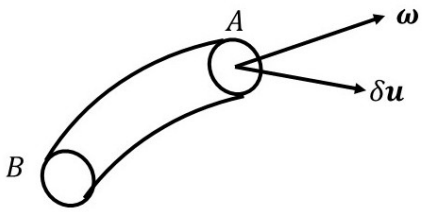

Figure 2.2: A sketch of the vortex-stretching mechanism. $\delta \boldsymbol{u}$ is the difference of velocity between two endpoints, A and B.

and $\delta \boldsymbol{u}$ is less than 90°, as shown in Figure 2.2, the vorticity tube will be stretched. In this scenario, the term $(\boldsymbol{\omega} \cdot \nabla)\boldsymbol{u} > 0$ signifies an increase of the magnitude of ω. This phenomenon is called "vortex stretching", which is the key process investigated in this thesis, and the term $(\boldsymbol{\omega} \cdot \nabla)\boldsymbol{u}$ is referred to as the vortex-stretching term. Hence, we can say that in 2D flows the vortex-stretching term is naturally null, which is not the case in 3D turbulence.

Moreover, in 2D turbulence, we can define a stream function Ψ as

$$u_x = \frac{\partial \Psi}{\partial y}, \quad u_y = -\frac{\partial \Psi}{\partial x} \tag{2.5}$$

with u_x and u_y the x- and y-components of velocity, respectively. From the definitions of vorticity and stream function, we can establish a relationship between them

$$\omega = -\Delta \Psi. \tag{2.6}$$

Here, the vorticity, ω, is presented as a scalar, not a vector, since in 2D turbulence $\boldsymbol{\omega} = \omega \boldsymbol{e_z}$.

2.1.2 Fundamental identities of homogeneous fields

Homogeneity is an essential concept in the study of turbulent flows. Throughout this thesis, we focus on statistically homogeneous turbulence.

A field is called statistically homogeneous if all statistics remain invariant under a shift in position [27], i.e., the space derivatives of all statistics are null. In the case of turbulent systems, a field $\boldsymbol{a}$ can be decomposed into a mean value $\langle \boldsymbol{a} \rangle$ and a fluctuation term $\boldsymbol{a}'$, i.e., $\boldsymbol{a} = \langle \boldsymbol{a} \rangle + \boldsymbol{a}'$ where $\langle \bullet \rangle$ is the ensemble average.

The definition of homogeneity implies that the gradient of a space-averaged value is zero. This intrinsic property allows us to derive some fundamental identities that prove valuable within the scope of this thesis. These identities, referenced extensively in Ref. [28], serve as indispensable tools in our subsequent discussions and analyses.

The first identity is

$$\langle a \nabla b \rangle = - \langle b \nabla a \rangle \tag{2.7}$$

where a and b are arbitrary and homogeneous scalar fields and $\langle \bullet \rangle$ indicates the ensemble average. Eq. (2.7) can be easily proved by combining the left-hand-side (LHS) and right-hand-side (RHS) terms and then applying the homogeneity condition.

The second identity is

$$\langle \boldsymbol{a} \cdot (\nabla \times \boldsymbol{b}) \rangle = \langle (\nabla \times \boldsymbol{a}) \cdot \boldsymbol{b} \rangle \tag{2.8}$$

where $\boldsymbol{a}$ and $\boldsymbol{b}$ are arbitrary and homogeneous vector fields. Eq. (2.8) can be proved with the help of Levi-Civita permutation tensor. The LHS can be rewritten as $\langle \boldsymbol{a} \cdot (\nabla \times \boldsymbol{b}) \rangle = \langle \epsilon_{ijk} \frac{\partial b_k}{\partial x_j} a_i \rangle$ under the Einstein summation convention. In this identity, a_i, b_i and x_i are the i-component of $\boldsymbol{a}$, $\boldsymbol{b}$ and position vector respectively. From Eq. (2.7), we can obtain $\langle \epsilon_{ijk} \frac{\partial b_k}{\partial x_j} a_i \rangle = -\langle \epsilon_{ijk} \frac{\partial a_i}{\partial x_j} b_k \rangle$. The definition of the Levi-Civita symbol shows $-\epsilon_{ijk} = \epsilon_{kji}$. Thus we have $\langle \boldsymbol{a} \cdot (\nabla \times \boldsymbol{b}) \rangle = \langle \epsilon_{kji} \frac{\partial a_i}{\partial x_j} b_k \rangle = \langle (\nabla \times \boldsymbol{a}) \cdot \boldsymbol{b} \rangle$.

Finally, if $\boldsymbol{h}$ and $\boldsymbol{g}$ are arbitrary, homogeneous, and incompressible vector fields with the relation $\boldsymbol{g} = \nabla \times \boldsymbol{h}$, we can derive

$$\frac{d}{dt} \langle \boldsymbol{h} \cdot \boldsymbol{g} \rangle = 2 \left\langle \boldsymbol{h} \cdot \left(\frac{\partial \boldsymbol{g}}{\partial t} \right) \right\rangle . \tag{2.9}$$

Applying homogeneity and incompressibility, we have $\frac{d}{dt} \langle \boldsymbol{h} \cdot \boldsymbol{g} \rangle = \frac{\partial}{\partial t} \langle \boldsymbol{h} \cdot \boldsymbol{g} \rangle = \langle \frac{\partial \boldsymbol{h}}{\partial t} \cdot \boldsymbol{g} \rangle + \langle \frac{\partial \boldsymbol{g}}{\partial t} \cdot \boldsymbol{h} \rangle$. Then using Eq. (2.8), we can derive $\langle \frac{\partial \boldsymbol{h}}{\partial t} \cdot \boldsymbol{g} \rangle = \langle \frac{\partial \boldsymbol{h}}{\partial t} \cdot (\nabla \times \boldsymbol{h}) \rangle = \langle (\nabla \times \frac{\partial \boldsymbol{h}}{\partial t}) \cdot \boldsymbol{h} \rangle = \langle \frac{\partial \nabla \times \boldsymbol{h}}{\partial t} \cdot \boldsymbol{h} \rangle = \langle \frac{\partial \boldsymbol{g}}{\partial t} \cdot \boldsymbol{h} \rangle$. Finally, Eq. (2.9) is proved.

Note that the identities (2.7), (2.8), and (2.9) can also be demonstrated under periodic conditions with $\langle \bullet \rangle$ the spatial average. The homogeneous condition is applied, given that all turbulent flows investigated in this thesis are homogeneous.

2.1.3 Inviscid invariants

In this subsection, we aim to elaborate on the concept of inviscid invariants, a fundamental concept in the study of turbulence. *Inviscid invariants* are the quantities that remain conserved throughout the turbulence evolution in the absence of external energy input or viscous stresses. For us, their importance stems from their definitive role in establishing the spectra at the absolute equilibrium state, a topic that will be further expounded in Chapter 4, as well as in determining the cascade properties of a turbulent system, with a detailed exploration to be provided in Chapter 5.

In 3D turbulence, the quadratic inviscid invariants are energy and helicity, whereas energy and enstrophy are conserved in 2D turbulence. The remainder of this subsection will be devoted to introducing these quadratic inviscid invariants and providing proof of their conservation.

Kinetic energy

The mean turbulent kinetic energy per unit mass, denoted as $E(t)$, is defined as

$$E(t) \equiv \frac{1}{2} \langle \boldsymbol{u}(\boldsymbol{x}, t) \cdot \boldsymbol{u}(\boldsymbol{x}, t) \rangle \tag{2.10}$$

where $\langle \bullet \rangle$ presents the ensemble average. For a statistically homogeneous field, it is also the spatial average.

Next, we demonstrate the conservation of energy under the Euler equation. By multiplying the velocity equation (Eq.(2.3)) by $\boldsymbol{u}$, and setting the viscosity ν to 0, and then applying an average, we derive the energy equation

$$\frac{\mathrm{d}E}{\mathrm{d}t} = -\frac{1}{\rho} \langle \boldsymbol{u} \cdot \nabla p \rangle \,. \tag{2.11}$$

Employing Eq. (2.7) and the incompressibility condition given by Eq.(2.2), the RHS of Eq. (2.11) simplifies to 0. This leads us to the conservation of energy for homogeneous, inviscid flows

$$\frac{\mathrm{d}E}{\mathrm{d}t} = 0. \tag{2.12}$$

This conservation law is universally applicable for turbulence in both 2D and 3D cases.

Enstrophy

Similar to energy, the local enstrophy $\Omega(\boldsymbol{x}, t)$ is defined as

$$\Omega(\boldsymbol{x}, t) \equiv \frac{1}{2}\boldsymbol{\omega}(\boldsymbol{x}, t) \cdot \boldsymbol{\omega}(\boldsymbol{x}, t), \tag{2.13}$$

which quantifies the "strength" of vorticity.

In 2D turbulence, the vortex-stretching term $(\boldsymbol{\omega} \cdot \nabla)$ is null, thereby simplifying the vorticity equation in an inviscid system to

$$\frac{\mathrm{d}\boldsymbol{\omega}}{\mathrm{d}t} = 0. \tag{2.14}$$

By multiplying Eq. (2.14) by $\boldsymbol{\omega}$, we straightforwardly deduce

$$\frac{\mathrm{d}\Omega}{\mathrm{d}t} = 0. \tag{2.15}$$

Upon averaging Eq. (2.15), we ascertain that the mean enstrophy per unit mass, $W(t) = \langle\Omega(\boldsymbol{x}, t)\rangle$, remains conserved in 2D homogeneous and inviscid flows. The vortex-stretching term breaks the conservation of enstrophy in 3D turbulence.

Moreover, in contrast to energy which is conserved only over the total domain, enstrophy is Not only conserved over the total domain, but also along individual trajectories, a conclusion substantiated by Eq. (2.15). Eq. (2.14) allows us to express

$$\frac{\mathrm{d}\omega^n}{\mathrm{d}t} = 0 \tag{2.16}$$

with n a positive integer. Here, the vorticity, ω, is again presented as a scalar defined as $\boldsymbol{\omega} = \omega \boldsymbol{e_z}$. Eq. (2.16) shows that, in fact, all quantities ω^n are inviscid invariants in 2D turbulence. These quantities are referred to as Casimirs.

Helicity

The local helicity $h(\boldsymbol{x}, t)$ is defined by

$$h(\boldsymbol{x}, t) \equiv \frac{1}{2}\boldsymbol{u}(\boldsymbol{x}, t) \cdot \boldsymbol{\omega}(\boldsymbol{x}, t). \tag{2.17}$$

A positive product of $\boldsymbol{u} \cdot \boldsymbol{\omega}$ corresponds to fluid particles with a velocity component along the direction of the rotation axis, representing a right-handed screw motion. Conversely, a

Figure 2.3: A figure in Ref. [27]. Sketches of positive helicity ($\boldsymbol{u} \cdot \boldsymbol{\omega} > 0$) on the left and negative helicity ($\boldsymbol{u} \cdot \boldsymbol{\omega} < 0$) on the right.

negative product indicates a velocity component along the opposite direction of the rotation axis, signifying a left-handed screw motion. Figure 2.3 depicts these motions for positive and negative helicity scenarios.

The mean helicity is defined as $H(t) = \langle h(\boldsymbol{x}, t) \rangle$. We now demonstrate the conservation of mean helicity by the Euler equation. Utilizing Eq. (2.9), the evolution of H can be expressed as

$$\frac{\mathrm{d}H}{\mathrm{d}t} = \left\langle \frac{\partial \boldsymbol{\omega}}{\partial t} \cdot \boldsymbol{u} \right\rangle . \tag{2.18}$$

By multiplying the vorticity equation, Eq. (2.4), by $\boldsymbol{u}$ with $\nu = 0$ and averaging, we derive

$$\frac{\mathrm{d}H}{\mathrm{d}t} = -\langle \boldsymbol{u} \cdot (\boldsymbol{u} \cdot \nabla)\boldsymbol{\omega} \rangle + \langle \boldsymbol{u} \cdot (\boldsymbol{\omega} \cdot \nabla)\boldsymbol{u} \rangle. \tag{2.19}$$

Using the vector triple product identity, we write

$$\nabla \times (\boldsymbol{u} \times \boldsymbol{\omega}) = \boldsymbol{u}(\nabla \cdot \boldsymbol{\omega}) - \boldsymbol{\omega}(\nabla \cdot \boldsymbol{u}) + (\boldsymbol{\omega} \cdot \nabla)\boldsymbol{u} - (\boldsymbol{u} \cdot \nabla)\boldsymbol{\omega}. \tag{2.20}$$

For incompressible fluids, we have the conditions $\nabla \cdot \boldsymbol{\omega} = 0$ and $\nabla \cdot \boldsymbol{u} = 0$. Thus Eq. (2.20) can be simplified to

$$\nabla \times (\boldsymbol{u} \times \boldsymbol{\omega}) = (\boldsymbol{\omega} \cdot \nabla)\boldsymbol{u} - (\boldsymbol{u} \cdot \nabla)\boldsymbol{\omega}. \tag{2.21}$$

Thus, the time-evolution of helicity can be rewritten as

$$\frac{\mathrm{d}H}{\mathrm{d}t} = \langle \boldsymbol{u} \cdot (\nabla \times (\boldsymbol{u} \times \boldsymbol{\omega})) \rangle . \tag{2.22}$$

The RHS of Eq. (2.22) is formally identical to the LHS of Eq. (2.8). Substituting $\boldsymbol{a}$ with $\boldsymbol{u}$ and $\boldsymbol{b}$ with $\boldsymbol{u} \times \boldsymbol{\omega}$, we deduce that $\langle \boldsymbol{u} \cdot (\nabla \times (\boldsymbol{u} \times \boldsymbol{\omega})) \rangle = \langle \boldsymbol{\omega} \cdot (\boldsymbol{u} \times \boldsymbol{\omega}) \rangle = 0$, yielding

$$\frac{\mathrm{d}H}{\mathrm{d}t} = 0. \tag{2.23}$$

This equation confirms helicity as an inviscid invariant in both 2D and 3D homogeneous turbulence. However, in 2D turbulence, the vorticity is perpendicular to the velocity, therefore helicity is always null and the conservation of helicity is trivial.

2.2 Turbulence in Fourier space

Solid walls and most other types of boundaries are incompatible with the notion of homogeneity. In theoretical and numerical studies, statistically homogeneous turbulence is therefore often studied using periodic boundary conditions, avoiding thereby the need of an infinitely large domain. The focus of this thesis is the study of homogeneous turbulence within such a periodic box. For periodic systems, undertaking investigations within Fourier space is convenient.

In this section, we firstly investigate governing equations in Fourier space. Then we focus on the spectra of energy, enstrophy, and helicity, and their respective fluxes. Finally, we introduce a practical tool for exploring turbulence within Fourier space — the helical decomposition.

2.2.1 Governing equations in Fourier space

We consider a flow in a periodic cubic domain of size L^3. The velocity can be represented by the Fourier series as follows

$$\boldsymbol{u}(\boldsymbol{x}, t) = \sum_{\boldsymbol{k}} \hat{\boldsymbol{u}}(\boldsymbol{k}, t) e^{\mathrm{i}\boldsymbol{k}\cdot\boldsymbol{x}} \tag{2.24}$$

where $\boldsymbol{k}$ is the wave vector, defined as $\boldsymbol{k} = (2\pi n_x/L, 2\pi n_y/L, 2\pi n_z/L)$ with n_x, n_y, n_z integers. Given $\boldsymbol{u}(\boldsymbol{x})$, the Fourier coefficients can be determined as

$$\hat{\boldsymbol{u}}(\boldsymbol{k}, t) = \frac{1}{L^3} \iiint \boldsymbol{u}(\boldsymbol{x}, t) e^{-\mathrm{i}\boldsymbol{k}\cdot\boldsymbol{x}} \mathrm{d}\boldsymbol{x}. \tag{2.25}$$

Note that because the velocity is a real quantity, the Fourier coefficients of velocity satisfy conjugate symmetry

$$\hat{\boldsymbol{u}}(\boldsymbol{k},t) = \hat{\boldsymbol{u}}^*(-\boldsymbol{k},t) \tag{2.26}$$

where the asterisk symbol $\bullet^*$ denotes the complex conjugate. Utilizing the Fourier derivative formula, the vorticity can be reformulated within Fourier space as

$$\hat{\boldsymbol{\omega}} = \mathrm{i}\boldsymbol{k} \times \hat{\boldsymbol{u}}(\boldsymbol{k},t), \tag{2.27}$$

and the divergence-free equation in Fourier space is represented as

$$\mathrm{i}\boldsymbol{k} \cdot \hat{\boldsymbol{u}}(\boldsymbol{k},t) = 0. \tag{2.28}$$

Eq. (2.28) indicates that in an incompressible fluid, the velocity vector is orthogonal to its corresponding wave vector.

In order to obtain the velocity equation for incompressible fluids in Fourier space, the Navier-Stokes equation is first converted into Fourier space. Then the transformed equation is projected onto the plane orthogonal to $\boldsymbol{k}$, yielding

$$\frac{\partial \hat{u}_i(\boldsymbol{k},t)}{\partial t} = -\mathrm{i}k_m P_{ij}(\boldsymbol{k}) \sum_{\boldsymbol{p}+\boldsymbol{q}=\boldsymbol{k}} \hat{u}_j(\boldsymbol{p},t)\hat{u}_m(\boldsymbol{q},t) - \nu k^2 \hat{u}_i(\boldsymbol{k},t) \tag{2.29}$$

where $P_{ij}(\boldsymbol{k})$ is the projection tensor $P_{ij}(\boldsymbol{k}) = \delta_{ij} - \frac{k_i k_j}{k^2}$. The convolution comes from the advection term, with the set of wave vectors $\boldsymbol{k}, \boldsymbol{p}, \boldsymbol{q}$ referred to as a triad, satisfying $\boldsymbol{p}+\boldsymbol{q} = \boldsymbol{k}$.

2.2.2 Energy, enstrophy, and helicity spectra

The theoretical framework developed in this thesis considers a continuous Fourier domain. However, the numerical simulations that we employ are executed within a discrete Fourier space. Hence, in this subsection, we present the definitions of energy, enstrophy, and helicity spectra within the continuous Fourier space, followed by their counterparts in discrete Fourier space. Furthermore, we provide a concise overview of the scaling laws that govern these spectra in 2D and 3D isotropic turbulence.

Spectra in continuous fields

In a continuous Fourier space, an arbitrary function $f(\boldsymbol{x})$ can be represented as the integral over its Fourier coefficients, as follows

$$f(\boldsymbol{x}) = \int_{-\infty}^{\infty} \hat{f}(\boldsymbol{k}) e^{\mathrm{i}2\pi \boldsymbol{k}\cdot\boldsymbol{x}} \mathrm{d}\boldsymbol{k}, \tag{2.30}$$

and the Fourier coefficients are calculated as

$$\hat{f}(\boldsymbol{k}) = \int_{-\infty}^{\infty} f(\boldsymbol{x}) e^{-\mathrm{i}2\pi \boldsymbol{k}\cdot\boldsymbol{x}} \mathrm{d}\boldsymbol{x}. \tag{2.31}$$

Within this context, the energy spectrum in a continuous Fourier space is defined as [27]

$$E(k) = \frac{1}{2} \int_{|\boldsymbol{k}|=k} \langle \hat{u}_i^*(\boldsymbol{k}) \hat{u}_i(\boldsymbol{k}) \rangle \mathrm{d}\mathcal{S}(k) \tag{2.32}$$

where $\langle \bullet \rangle$ means the ensemble average, and $\mathcal{S}(k)$ indicates the surface area of a sphere with a radius of k in 3D turbulence and the circumference of a circle with radius k in 2D turbulence. The energy spectrum is closely associated with the two-point velocity correlation, defined as $R_{ij}(\boldsymbol{r}) \equiv \langle u_i(\boldsymbol{x}) u_j(\boldsymbol{x}+\boldsymbol{r}) \rangle$. Applying the convolution theorem, the Fourier coefficient of $R_{ij}(\boldsymbol{r})$ with respect to the wave number $\boldsymbol{k}$ is expressed as $\hat{R}_{ij}(\boldsymbol{k}) = \hat{u}_i^*(\boldsymbol{k}) \hat{u}_j(\boldsymbol{k})$. Thus the energy spectrum, $E(k)$, is a statistical measure that signifies the density of energy content of turbulent structures associated with a length scale around $2\pi/k$. Moreover, mean kinetic energy per unit mass, E, can be calculated as the integration of the energy spectrum

$$E = \frac{1}{2} \langle u_i(\boldsymbol{x}) u_i(\boldsymbol{x}) \rangle = \frac{1}{2} R_{ii}(\boldsymbol{0}) = \frac{1}{2} \langle R_{ii}(\boldsymbol{0}) \rangle = \frac{1}{2} \iiint \langle \hat{R}_{ii}(\boldsymbol{k}) \rangle \mathrm{d}\boldsymbol{k} = \int_{-\infty}^{\infty} E(k) \mathrm{d}k. \tag{2.33}$$

Analogous to the energy spectrum, the enstrophy spectrum is defined as

$$W(k) = \frac{1}{2} \int_{|\boldsymbol{k}|=k} \langle \hat{\omega}_i^*(\boldsymbol{k}) \hat{\omega}_i(\boldsymbol{k}) \rangle \mathrm{d}\mathcal{S}(k). \tag{2.34}$$

Substituting Eq. (2.27) into Eq. (2.34), we can establish a relation between the enstrophy spectrum and the energy spectrum as follows

$$W(k) = \frac{1}{2} \int_{|\boldsymbol{k}|=k} k^2 \langle \hat{u}_i^*(\boldsymbol{k}) \hat{u}_i(\boldsymbol{k}) \rangle \mathrm{d}\mathcal{S}(k) = k^2 E(k). \tag{2.35}$$

Further, the helicity spectrum is defined as

$$H(k) = \frac{1}{2} \int_{|\boldsymbol{k}|=k} \langle \hat{\omega}_i^*(\boldsymbol{k}) \hat{u}_i(\boldsymbol{k}) \rangle \mathrm{d}\mathcal{S}(k). \tag{2.36}$$

We note that $\hat{\omega}_i^*(\boldsymbol{k})\hat{u}_i(\boldsymbol{k})$ is a complex number, however, the RHS of Eq. (2.36) always yields a real number, ensuring that $H(k)$ is real. This is due to the fact that for any wave vector $\boldsymbol{k}$ included in the integration, its opposite wave vector $-\boldsymbol{k}$ is also included, and the summation of the terms $\hat{\omega}_i^*(\boldsymbol{k})\hat{u}_i(\boldsymbol{k})$ and $\hat{\omega}_i^*(-\boldsymbol{k})\hat{u}_i(-\boldsymbol{k})$ gives a real number. Moreover, the helicity spectrum can also be defined as $H(k) = \frac{1}{2}\int_{|\boldsymbol{k}|=k}\langle\hat{\omega}_i(\boldsymbol{k})\hat{u}_i^*(\boldsymbol{k})\rangle \mathrm{d}\mathcal{S}(k)$, which is equivalent to Eq. (2.36) because $\mathrm{Re}[\hat{\omega}_i^*(\boldsymbol{k})\hat{u}_i(\boldsymbol{k})] = \mathrm{Re}[\hat{\omega}_i(\boldsymbol{k})\hat{u}_i^*(\boldsymbol{k})]$.

Spectra in discrete fields

In the context of numerical simulations, fluid fields are discretized. Thus we also need to investigate discrete forms of spectra. Within a discrete Fourier space, the Fourier series representation of velocity is given by Eq. (2.24). As a result, the mean kinetic energy per unit mass can be calculated as

$$E = \frac{1}{2}\langle u_i(\boldsymbol{x})u_i(\boldsymbol{x})\rangle = \frac{1}{2}R_{ii}(\boldsymbol{0}) = \frac{1}{2}\sum_{\boldsymbol{k}}\langle\hat{R}_{ii}(\boldsymbol{k})\rangle e^{\mathrm{i}\boldsymbol{k}\cdot\boldsymbol{0}} = \frac{1}{2}\sum_{\boldsymbol{k}}\langle\hat{u}_i^*(\boldsymbol{k})\hat{u}_i(\boldsymbol{k})\rangle. \tag{2.37}$$

Note that, in isotropic turbulence, the ensemble average term $\langle\hat{u}_i^*(\boldsymbol{k})\hat{u}_i(\boldsymbol{k})\rangle$ depends only on k. If the unit wave number, $\Delta k = 2\pi/L$, is sufficiently small (i.e., $\Delta k \ll k$), the number of wave vectors enclosed between spherical shells of radii $k - \Delta k/2$ and $k + \Delta k/2$ is approximately $4\pi k^2\Delta k/(\Delta k)^3$. Therefore, in 3D isotropic turbulence, the energy spectrum can be defined as [29]

$$E(k) = 2\pi\frac{k^2}{(\Delta k)^3}\langle\hat{u}_i^*(\boldsymbol{k})\hat{u}_i(\boldsymbol{k})\rangle. \tag{2.38}$$

The mean energy per unit mass can then be calculated as $E = \sum_k E(k)\Delta k$. Note that for small values of k, the discrete nature of Fourier space can induce anisotropy in the statistics [30, 31].

Within the numerical simulations carried out in this thesis, the energy spectrum is defined directly from Eq. (2.37), as follows

$$E(k) = \frac{1}{\Delta k}\sum_{k-\Delta k/2\le|\boldsymbol{k}|<k+\Delta k/2}\frac{1}{2}\hat{u}_i^*(\boldsymbol{k})\hat{u}_i(\boldsymbol{k}). \tag{2.39}$$

When $\Delta k \ll k$, the expression (2.39) approximates (2.38). Similarly, enstrophy and helicity spectra are defined as

$$W(k) = \frac{1}{\Delta k}\sum_{k-\Delta k/2\le|\boldsymbol{k}|<k+\Delta k/2}\frac{1}{2}\hat{\omega}_i^*(\boldsymbol{k})\hat{\omega}_i(\boldsymbol{k}), \tag{2.40}$$

and

$$H(k) = \frac{1}{\Delta k} \sum_{k-\Delta k/2 \leq |\boldsymbol{k}| < k+\Delta k/2} \frac{1}{2} \hat{\omega}_i^*(\boldsymbol{k}) \hat{u}_i(\boldsymbol{k}), \tag{2.41}$$

respectively.

Analogous to 3D turbulence, the expression for the energy spectrum in 2D isotropic turbulence can be expressed as [29]

$$E(k) = \pi \frac{k}{(\Delta k)^2} \langle \hat{u}_i^*(\boldsymbol{k}) \hat{u}_i(\boldsymbol{k}) \rangle. \tag{2.42}$$

2.2.3 Inviscid invariants in Fourier space

In Sec. 2.1.3, we made a demonstration in physical space that the quadratic inviscid invariants are energy and helicity in 3D turbulence, and energy and enstrophy are conserved in 2D turbulence. In this subsection, we prove that these inviscid invariants are also conserved triad by triad in Fourier space.

In Fourier space, the total energy can be calculated as $E = \frac{1}{2} \sum_{\boldsymbol{k}} \hat{u}_i(\boldsymbol{k}) \hat{u}_i^*(\boldsymbol{k})$, as introduced in Sec. 2.2.2. To derive the time derivative of energy, we begin by considering the time evolution equations for $\hat{u}_i(\boldsymbol{k})$ (Eq.(2.29)) and $\hat{u}_i^*(\boldsymbol{k})$, then multiplying respectively by $\hat{u}_i^*(\boldsymbol{k})$ and $\hat{u}_i(\boldsymbol{k})$, and adding the two equations. Adding the equations for different $\boldsymbol{k}$, we obtain the following expression for the time derivative of energy in an inviscid system:

$$\frac{\partial E}{\partial t} = \frac{1}{2} \sum_{\boldsymbol{k}} \left(-\mathrm{i} k_m P_{ij}(\boldsymbol{k}) \hat{u}_i^*(\boldsymbol{k}, t) \sum_{\boldsymbol{p}+\boldsymbol{q}=\boldsymbol{k}} \hat{u}_j(\boldsymbol{p}, t) \hat{u}_m(\boldsymbol{q}, t) + \mathrm{i} k_m P_{ij}(\boldsymbol{k}) \hat{u}_i(\boldsymbol{k}, t) \sum_{\boldsymbol{p}+\boldsymbol{q}=\boldsymbol{k}} \hat{u}_j^*(\boldsymbol{p}, t) \hat{u}_m^*(\boldsymbol{q}, t) \right) \tag{2.43}$$

where $P_{ij}(\boldsymbol{k}) = \delta_{ij} - \frac{k_i k_j}{k^2}$. For a more symmetrical form, we use the relation $\hat{\boldsymbol{u}}(-\boldsymbol{k}) = \hat{\boldsymbol{u}}^*(\boldsymbol{k})$, leading to the following expression for the time derivative of energy:

$$\frac{\partial E}{\partial t} = \sum_{\boldsymbol{p}+\boldsymbol{q}+\boldsymbol{k}=\boldsymbol{0}} \mathrm{Im}[\mathcal{T}(\boldsymbol{k}, \boldsymbol{p}, \boldsymbol{q}, t)] \tag{2.44}$$

with $\mathcal{T}(\boldsymbol{k}, \boldsymbol{p}, \boldsymbol{q}, t) = k_m P_{ij}(\boldsymbol{k}) \hat{u}_i(\boldsymbol{k}, t) \hat{u}_j(\boldsymbol{p}, t) \hat{u}_m(\boldsymbol{q}, t)$ and $\mathrm{Im}[\bullet]$ denoting the imaginary part of a complex number. Considering the incompressibility condition $\mathrm{i} k_i \hat{u}_i(\boldsymbol{k}) = 0$ (Eq.(2.28)), the expression of $\mathcal{T}(\boldsymbol{k}, \boldsymbol{p}, \boldsymbol{q})$ simplifies to $\mathcal{T}(\boldsymbol{k}, \boldsymbol{p}, \boldsymbol{q}) = k_m \hat{u}_i(\boldsymbol{k}) \hat{u}_i(\boldsymbol{p}) \hat{u}_m(\boldsymbol{q})$, with time t omitted

for simplicity. For any given set of triad-interaction wave vectors $\{\boldsymbol{k}, \boldsymbol{p}, \boldsymbol{q}\}$, we can observe that

$$\begin{aligned}\mathcal{T}(\boldsymbol{k},\boldsymbol{p},\boldsymbol{q}) + \mathcal{T}(\boldsymbol{k},\boldsymbol{q},\boldsymbol{p}) + \mathcal{T}(\boldsymbol{p},\boldsymbol{k},\boldsymbol{q}) + \mathcal{T}(\boldsymbol{p},\boldsymbol{q},\boldsymbol{k}) + \mathcal{T}(\boldsymbol{q},\boldsymbol{k},\boldsymbol{p}) + \mathcal{T}(\boldsymbol{q},\boldsymbol{p},\boldsymbol{k}) = \\ k_m\hat{u}_m(\boldsymbol{p})\hat{u}_i(\boldsymbol{q})\hat{u}_i(\boldsymbol{k}) + k_m\hat{u}_m(\boldsymbol{q})\hat{u}_i(\boldsymbol{p})\hat{u}_i(\boldsymbol{k}) + p_m\hat{u}_m(\boldsymbol{k})\hat{u}_i(\boldsymbol{q})\hat{u}_i(\boldsymbol{p}) + \\ p_m\hat{u}_m(\boldsymbol{q})\hat{u}_i(\boldsymbol{k})\hat{u}_i(\boldsymbol{p}) + q_m\hat{u}_m(\boldsymbol{k})\hat{u}_i(\boldsymbol{p})\hat{u}_i(\boldsymbol{q}) + q_m\hat{u}_m(\boldsymbol{p})\hat{u}_i(\boldsymbol{k})\hat{u}_i(\boldsymbol{q}).\end{aligned} \tag{2.45}$$

By applying the condition $\boldsymbol{k} + \boldsymbol{p} + \boldsymbol{q} = \boldsymbol{0}$, we can simplify the term $k_m\hat{u}_m(\boldsymbol{p})\hat{u}_i(\boldsymbol{q})\hat{u}_i(\boldsymbol{k}) + q_m\hat{u}_m(\boldsymbol{p})\hat{u}_i(\boldsymbol{k})\hat{u}_i(\boldsymbol{q}) = -p_m\hat{u}_m(\boldsymbol{p})\hat{u}_i(\boldsymbol{q})\hat{u}_i(\boldsymbol{k})$. We then utilize the incompressibility condition, which gives $p_m\hat{u}_m(\boldsymbol{p}) = 0$, to show that $\mathcal{T}(\boldsymbol{k},\boldsymbol{p},\boldsymbol{q}) + \mathcal{T}(\boldsymbol{q},\boldsymbol{p},\boldsymbol{k}) = 0$. Similarly, the other terms in the equation can be simplified. After these simplifications, we obtain that $\mathcal{T}(\boldsymbol{k},\boldsymbol{p},\boldsymbol{q}) + T(\boldsymbol{k},\boldsymbol{q},\boldsymbol{p}) + \mathcal{T}(\boldsymbol{p},\boldsymbol{k},\boldsymbol{q}) + \mathcal{T}(\boldsymbol{p},\boldsymbol{q},\boldsymbol{k}) + \mathcal{T}(\boldsymbol{q},\boldsymbol{k},\boldsymbol{p}) + \mathcal{T}(\boldsymbol{q},\boldsymbol{p},\boldsymbol{k}) = 0$, which demonstrates that energy is conserved by each triad of interacting wave vectors in Fourier space.

Using the same method, we can prove the triad-by-triad conservation of helicity in 3D turbulence and enstrophy in 2D turbulence.

2.2.4 Energy cascade in Fourier space

The cascade process in turbulence was initially suggested by Richardson [9] and Kolmogorov [10]. Let us define a Reynolds number $Re = \frac{\mathcal{U}\mathcal{L}}{\nu}$, where $\mathcal{U}$ and $\mathcal{L}$ represent characteristic velocity and length scales, respectively. In cases where Re is sufficiently high, an "inertial range" of scales l emerges, with l being substantially smaller than the flow scale $\mathcal{L}$ and considerably larger than the length scale of the smallest eddies η, also known as the Kolmogorov length scale. Within the inertial range, turbulent motions were assumed by Kolmogorov to be isotropic. The energy cascades from the large flow scale down along this inertial range. Simultaneously, $\eta \ll l$ ensures no dissipation within the inertial range. Thus all the energy from large scales will be transferred toward the Kolmogorov scale, and there is a flux of energy between scales.

Fluxes

The energy flux can be calculated from the governing equations in Fourier space. In discrete Fourier space, the energy within wave vector $\boldsymbol{k}$ can be calculated as $\hat{E}(\boldsymbol{k},t) = \frac{1}{2}\hat{u}_i(\boldsymbol{k},t)\hat{u}_i^*(\boldsymbol{k},t)$. The time evolution of $\hat{E}(\boldsymbol{k},t)$ can be derived from Eq. (2.29), which results in the following:

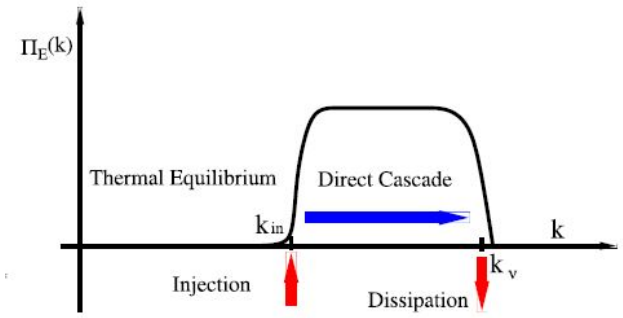

Figure 2.4: Sketch of the spectrum of energy flux in 3D turbulence presented in Ref. [32].

$$\frac{\partial \hat{E}(\boldsymbol{k},t)}{\partial t} = T(\boldsymbol{k},t) - 2\nu k^2 \hat{E}(\boldsymbol{k},t), \tag{2.46}$$

where $T(\boldsymbol{k},t)$ represents a transfer of energy amongst Fourier modes, expressed as

$$T(\boldsymbol{k},t) = -k_m P_{ij}(\boldsymbol{k}) \sum_{\boldsymbol{p}+\boldsymbol{q}=\boldsymbol{k}} \mathrm{Im}[\hat{u}_i(\boldsymbol{k},t)\hat{u}_j^*(\boldsymbol{p},t)\hat{u}_m^*(\boldsymbol{q},t)] \tag{2.47}$$

with Im[•] the imaginary part of the quantity in the bracket. Accordingly, the flux of energy transferred through a wave number k can be defined as

$$\Pi_E(k,t) = -\sum_{|\boldsymbol{k}|\leq k} T(\boldsymbol{k},t). \tag{2.48}$$

$\Pi_E(k,t)$ is thus characterized as the energy flux. As energy is an inviscid invariant, in the cases where $\nu = 0$, the total energy of the system remains constant, leading to $\frac{\mathrm{d}E}{\mathrm{d}t} = -\sum_{\boldsymbol{k}} T(\boldsymbol{k},t) = 0$, which assures $\Pi_E(k_{\max},t) = 0$. Fig. 2.4 is a sketch of the spectrum of energy flux in 3D turbulence. Noticeably, both $\Pi_E(k_{\max},t)$ and $\Pi_E(k_{\min},t)$ are zero. Moreover, in the inertial range ($k_{in} \ll k \ll k_\nu$ in Fig. 2.4), neither dissipation nor energy input is present, which ensures the constancy of $\Pi_E(k)$ within the inertial range. This constancy is depicted as a plateau in Fig. 2.4.

In continuous Fourier space, the evolution of energy spectrum can be written as

$$\frac{\partial E(k,t)}{\partial t} = T(k,t) - 2\nu k^2 E(k,t) \tag{2.49}$$

with $T(k,t) = \int_{|\boldsymbol{k}|=k} \left(k_m P_{ij}(\boldsymbol{k}) \iint_{\boldsymbol{p}+\boldsymbol{q}=\boldsymbol{k}} \mathrm{Im}[\hat{u}_i(\boldsymbol{k},t)\hat{u}_j^*(\boldsymbol{p},t)\hat{u}_m^*(\boldsymbol{q},t)]\mathrm{d}\boldsymbol{p}\mathrm{d}\boldsymbol{q} \right) \mathrm{d}\mathcal{S}(k)$. The spectrum of energy flux is defined by the integration of $T(k,t)$ as

$$\Pi(k,t) = -\int_0^k T(k',t)\mathrm{d}k'. \tag{2.50}$$

Applying the same methodology allows for the definition of spectra for helicity and enstrophy fluxes in discrete and continuous Fourier space.

Dissipation

The second term on the RHS of Eq. (2.46) corresponds to energy dissipation by viscosity. Thus we can define the dissipation rate of energy as

$$\epsilon = \int 2\nu k^2 E(k,t)\mathrm{d}k. \tag{2.51}$$

Due to the k^2 term in the integral, dissipation at large scales (i.e., small wave numbers) is typically much smaller than at small scales (i.e., large wave numbers)[1]. Thus, the majority of viscous dissipation occurs at smaller scales.

Analogous to the energy dissipation rate, we can define the dissipation rates of enstrophy and helicity as

$$\epsilon_W = \int 2\nu k^2 W(k,t)\mathrm{d}k = \int 2\nu k^4 E(k,t)\mathrm{d}k, \tag{2.52}$$

and

$$\epsilon_H = \int 2\nu k^2 H(k,t)\mathrm{d}k, \tag{2.53}$$

respectively.

Scaling laws

Under the energy cascade procedure, Kolmogorov proposed that the statistical properties within the inertial range are universally determined by the dissipation rate of energy [10]. Employing dimensional analysis allows us to derive the energy spectrum formula within the inertial range [27]:

$$E(k) = C\epsilon^{2/3}k^{-5/3} \tag{2.54}$$

with C a universal constant.

Two-dimensional (2D) turbulence differs from its 3D counterpart, presenting a counter-direction dual cascade of two inviscid invariants: energy and enstrophy. This difference

[1] This assumes that the energy spectrum is shallower than k^{-3}

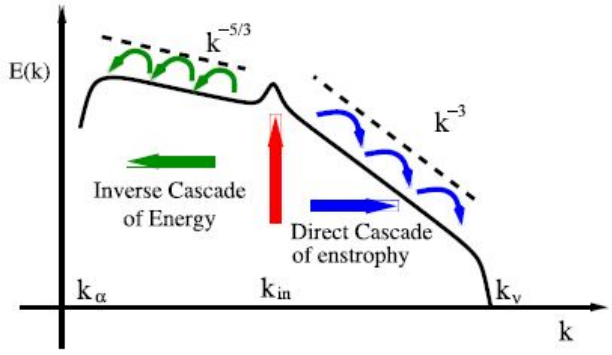

Figure 2.5: Log–log sketch of the energy spectrum in 2D turbulence from Ref. [32]. k_{in} indicates the wave number where energy is input. k_α and k_ν represent the wave number where the large-scale friction and small-scale dissipation occur, respectively.

necessitates energy cascading from smaller scales towards larger scales, while enstrophy cascades in the opposite direction, leading to two inertial ranges in 2D turbulence. In the inertial range of energy cascade, the statistics depend only on the 2D energy dissipation rate, ϵ_{2D}. The dimensional analysis provides the following energy spectrum formula:

$$E(k) = C_{2D}\epsilon_{2D}^{2/3}k^{-5/3} \tag{2.55}$$

with C_{2D} a universal constant. Notably, the energy spectrum formula in 2D turbulence (Eq. (2.55)) is analogous to the formula for 3D turbulence (Eq. (2.54)), but with different universal constants. In the inertial range of the enstrophy cascade, statistics only depend on the dissipation rate of enstrophy ϵ_W, and dimensional analysis yields the energy spectrum formula:

$$E(k) = C_W\epsilon_W^{2/3}k^{-3} \tag{2.56}$$

with C_W a universal constant. Fig. 2.5 presents a sketch of the energy spectrum in 2D turbulence.

For 3D turbulence, helicity, in addition to energy, is also an inviscid invariant. Numerical simulations reveal that both energy and helicity cascade forward in classic 3D turbulence, and the helicity spectrum is proportional to $k^{-5/3}$ [29, 32, 33], expressed as

$$H(k) \propto k^{-5/3}. \tag{2.57}$$

2.2.5 Helical decomposition

The helical decomposition technique is an instrumental tool for analyzing incompressible flow in Fourier space. In Chapter 4, we utilize this method to derive the equilibrium spectra. In this section, we introduce the details of this decomposition method.

The concept of helical decomposition was introduced by Cambont & Jacquin [34] and Waleffe [35], and has since been used by many researchers [24,36,37]. A similar decomposition method was proposed by Craya and Herring [38], and this Craya-Herring decomposition and helicity decomposition can be converted into each other.

In 3D turbulence, the most prevalent decomposition of velocity in Fourier space employs Cartesian coordinates with a basis $(\boldsymbol{e_x}, \boldsymbol{e_y}, \boldsymbol{e_z})$. The three velocity components $\hat{u}_x, \hat{u}_y, \hat{u}_z$ are complex numbers, with the total velocity expressed as $\hat{\boldsymbol{u}}(\boldsymbol{k}) = \hat{u}_x(\boldsymbol{k})\boldsymbol{e_x} + \hat{u}_y(\boldsymbol{k})\boldsymbol{e_y} + \hat{u}_z(\boldsymbol{k})\boldsymbol{e_z}$. However, for an incompressible fluid, an additional condition arises: $\nabla \cdot \boldsymbol{u} = 0$. In Fourier space, this condition becomes $\boldsymbol{k} \cdot \hat{\boldsymbol{u}}(\boldsymbol{k}) = \boldsymbol{0}$, signifying that the velocity vector is orthogonal to its corresponding wave vector. From this insight, Waleffe proposed a novel decomposition of velocity known as the helical decomposition.

The first step in this decomposition requires a new set of three basis vectors. Given the incompressibility, $\hat{\boldsymbol{u}}(\boldsymbol{k})$ can be decomposed on the plane orthogonal to $\boldsymbol{k}$. The first basis vector is chosen as the unit vector, $\boldsymbol{\kappa}$, in the direction of $\boldsymbol{k}$, i.e., $\boldsymbol{k} = k\boldsymbol{\kappa}$. The remaining two basic vectors are selected to be orthogonal to $\boldsymbol{k}$, ensured by the curl operation. Waleffe chose these two basic vectors as $\boldsymbol{h}_s(\boldsymbol{k}) = \boldsymbol{\zeta} \times \boldsymbol{\kappa} + \mathrm{i}s\boldsymbol{\zeta}$, where $s = \pm$ is a sign coefficient and $\boldsymbol{\zeta} = (\boldsymbol{z} \times \boldsymbol{\kappa}) / ||\boldsymbol{z} \times \boldsymbol{\kappa}||$, with $\boldsymbol{z}$ as an arbitrary vector nonparallel to $\boldsymbol{\kappa}$. This selection yields an orthogonal basis $(\boldsymbol{k}, \boldsymbol{h}_+(\boldsymbol{k}), \boldsymbol{h}_-(\boldsymbol{k}))$, satisfying the orthogonality conditions: $\boldsymbol{k} \cdot \boldsymbol{h}_+(\boldsymbol{k}) = 0, \boldsymbol{k} \cdot \boldsymbol{h}_-(\boldsymbol{k}) = 0$, and $\boldsymbol{h}_+(\boldsymbol{k}) \cdot \boldsymbol{h}_-^*(\boldsymbol{k}) = 0$. Note that $\boldsymbol{h}_+(\boldsymbol{k})$ and $\boldsymbol{h}_-(\boldsymbol{k})$ are complex, three-dimensional orthogonal vectors. This helical basis exhibits several properties, with straightforward proofs, including:

- $\boldsymbol{h}_s(\boldsymbol{k}) \cdot \boldsymbol{h}_s^*(\boldsymbol{k}) = 2$
- $\boldsymbol{h}_s^*(\boldsymbol{k}) = \boldsymbol{h}_{-s}(\boldsymbol{k})$
- $\boldsymbol{h}_s(-\boldsymbol{k}) = \boldsymbol{h}_s^*(\boldsymbol{k})$
- $\mathrm{i}\boldsymbol{k} \times \boldsymbol{h}_s(\boldsymbol{k}) = sk\boldsymbol{h}_s(\boldsymbol{k})$

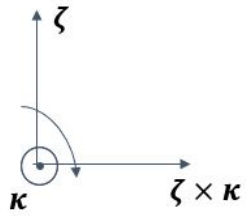

Figure 2.6: Sketch of the real-space velocity corresponding to $\boldsymbol{h}_+$ when $\boldsymbol{k}\cdot\boldsymbol{x}$ increases.

The helical components of velocity in Fourier space can then be defined as

$$\hat{u}_s(\boldsymbol{k}) = \frac{\boldsymbol{h}_s^*(\boldsymbol{k})\cdot\hat{\boldsymbol{u}}(\boldsymbol{k})}{\boldsymbol{h}_s^*(\boldsymbol{k})\cdot\boldsymbol{h}_s(\boldsymbol{k})}. \tag{2.58}$$

The total velocity is then expressed as

$$\hat{\boldsymbol{u}}(\boldsymbol{k}) = \hat{u}_+(\boldsymbol{k})\boldsymbol{h}_+(\boldsymbol{k}) + \hat{u}_-(\boldsymbol{k})\boldsymbol{h}_-(\boldsymbol{k}) \tag{2.59}$$

with $\hat{u}_+(\boldsymbol{k})$ and $\hat{u}_-(\boldsymbol{k})$ complex numbers.

The interpretation of this helical decomposition can be understood as separating the velocity into distinct helical modes. Consider the real-space velocity corresponding to $\boldsymbol{h}_+(\boldsymbol{k})$. Using the real-space basis $(\boldsymbol{\zeta}\times\boldsymbol{\kappa}, \boldsymbol{\zeta}, \boldsymbol{\kappa})$, we can denote this plus mode basis vector as $\boldsymbol{h}_+(\boldsymbol{k}) = \begin{pmatrix} 1 \\ \mathrm{i} \\ 0 \end{pmatrix}$. The corresponding real-space velocity can be then calculated as follows

$$\boldsymbol{h}_+(\boldsymbol{k})e^{\mathrm{i}\boldsymbol{k}\cdot\boldsymbol{x}} + \boldsymbol{h}_+^*(\boldsymbol{k})e^{-\mathrm{i}\boldsymbol{k}\cdot\boldsymbol{x}} = \begin{pmatrix} 1 \\ \mathrm{i} \\ 0 \end{pmatrix} e^{\mathrm{i}\boldsymbol{k}\cdot\boldsymbol{x}} + \begin{pmatrix} 1 \\ -\mathrm{i} \\ 0 \end{pmatrix} e^{-\mathrm{i}\boldsymbol{k}\cdot\boldsymbol{x}} = 2\begin{pmatrix} \cos(\boldsymbol{k}\cdot\boldsymbol{x}) \\ -\sin(\boldsymbol{k}\cdot\boldsymbol{x}) \\ 0 \end{pmatrix}. \tag{2.60}$$

This flow forms a clockwise rotation along the direction of $\boldsymbol{k}$, thus creating a left-handed helix as illustrated in Fig. 2.6. Similarly, the real-space velocity corresponding to $\boldsymbol{h}_-(\boldsymbol{k})$ will rotate in a counterclockwise direction, creating a right-handed helix as $\boldsymbol{k}\cdot\boldsymbol{x}$ increases.

2.3 Statistical mechanics

Throughout the investigation of turbulence without vortex stretching, we employ statistical mechanics methods widely utilized in the analysis of normal turbulent systems. Subsections

2.3.1 and 2.3.2 offer concise overviews of two traditional statistical physics methodologies: the truncated system statistical analysis and the point-vortex model, respectively.

2.3.1 Equilibrium statistical mechanics of truncated Euler flows

This section introduces existing theories of statistical mechanics applied to inviscid, spectrally truncated turbulence. Spectral truncation, also known as Galerkin truncation, refers to the discarding of Fourier modes of the system beyond a specific range $[k_{\min}, k_{\max}]$, which is common in numerical simulations.

Brief historical overview

Lee [39] first derived a prediction for the energy spectrum in absolute (or thermal) equilibrium, assuming the equipartition of energy among all the Fourier modes of the system under investigation. However, Lee did not consider the second inviscid invariant, helicity in 3D turbulence (and enstrophy in 2D turbulence). Indeed, the helicity was at that time not yet identified as an invariant of the Euler equation. Subsequently, Kraichnan proposed that helicity and enstrophy could be included in the equipartition, and he corrected the exact formulas of energy spectra at the absolute equilibrium state in 3D turbulence [40]. He also considered the case of 2D turbulence [41].

Building on this statistical approach proposed by Kraichnan, Frisch [42] derived absolute equilibrium spectra for inviscid magnetohydrodynamic turbulence and suggested the possibility of an inverse cascade of magnetic helicity. Furthermore, a large variety of problems has also been tackled using this statistical mechanics method such as the characterization of magnetohydrodynamic turbulence [42, 43] and random reversals in turbulent systems [44]. Zhu [45] employed a similar method to investigate absolute equilibria of incompressible neutral fluids and plasmas using helical decomposition [35]. In a recent paper [46], further motivations are given to study truncated turbulent systems using statistical mechanics.

Derivation of energy spectra at the absolute equilibrium state

Lee [39] showed that if the Galerkin-truncated Euler equations are analyzed, a Liouville equation can be formulated, which enables a direct application of equilibrium statistical mechanics. The reasoning, which we will discuss in more detail in this investigation, is that

if the Euler equations are represented by a finite number of Fourier modes, their dynamics is incompressible in phase-space. Applying then equilibrium statistical mechanics to the Fourier modes leads to the prediction of the most probable, thermal-equilibrium state, which corresponds to an equidistribution of energy over all accessible locations of phase space. The Fourier distribution of kinetic energy is given by

$$U(k) = \frac{1}{2}\langle \hat{\boldsymbol{u}}(\boldsymbol{k}) \cdot \hat{\boldsymbol{u}}^*(\boldsymbol{k}) \rangle, \tag{2.61}$$

with $\hat{\boldsymbol{u}}(\boldsymbol{k})$ the Fourier coefficient associated with the velocity at wave vector $\boldsymbol{k}$ and k the norm of this wave vector. Note that, for isotropic turbulence, $\langle \hat{\boldsymbol{u}}(\boldsymbol{k}) \cdot \hat{\boldsymbol{u}}^*(\boldsymbol{k}) \rangle$ depends only on k. Lee's result implies that the average energy distribution is simply constant,

$$U(k) = \text{constant} = 2/\alpha, \tag{2.62}$$

where the constant is named $2/\alpha$, for later convenience. The energy spectrum can be derived from Eq. (2.32). In 3D turbulence, the surface of a spherical shell with a radius k is calculated as $4\pi k^2$. Hence, the energy distribution (2.62) corresponds to a 3D isotropic kinetic energy spectrum,

$$E(k) = 4\pi k^2 U(k) = \frac{8\pi k^2}{\alpha}. \tag{2.63}$$

This analysis by Lee considered the kinetic energy of the 3D turbulent fluctuations as the only invariant of the system. In the 1960s, another invariant was shown to exist in a 3D bounded flow [47, 48]. This invariant is named helicity. After the introduction of the concept of helicity, it was anticipated by Kraichnan [40] using equilibrium statistical mechanics that the presence of helicity should not dramatically influence the dynamics. The principal reasoning to arrive at this insight was based on an analysis similar to that of Lee.

Before discussing 3D, we start by investigating 2D, inviscid, and spectrally truncated turbulence encompassing N Fourier modes. We recall that, in 2D turbulence, inviscid invariants are energy and enstrophy. The governing equation of velocity (Eq. (2.29)) with $\nu = 0$ can be interpreted as the equation governing a trajectory within the $4N$-dimensional phase space. The dimension is $4N$ because the velocity vector at each Fourier mode has two directional components, each containing a real and an imaginary part. Accordingly, the coordinates are denoted as $\boldsymbol{y} = (y_1, y_2, ..., y_{n_1}, y_{n_2}, y_{n_3}, y_{n_4}, ..., y_{N_4})$. The energy and enstrophy at the nth

wave vector $\boldsymbol{k}_n$ can subsequently be expressed as

$$E_n = \frac{1}{2}\hat{\boldsymbol{u}}(\boldsymbol{k}_n)\cdot\hat{\boldsymbol{u}}^*(\boldsymbol{k}_n) = \frac{1}{2}\hat{u}_i(\boldsymbol{k}_n)\hat{u}_i^*(\boldsymbol{k}_n) = \frac{1}{2}(y_{n_1}^2 + y_{n_2}^2 + y_{n_3}^2 + y_{n_4}^2), \tag{2.64}$$

$$W_n = \frac{1}{2}\hat{\boldsymbol{\omega}}(\boldsymbol{k}_n)\cdot\hat{\boldsymbol{\omega}}^*(\boldsymbol{k}_n) = \frac{k_n^2}{2}(y_{n_1}^2 + y_{n_2}^2 + y_{n_3}^2 + y_{n_4}^2) = k_n^2 E_n. \tag{2.65}$$

respectively. Within this framework, each point in phase space signifies a particular state of the whole system. $P(\boldsymbol{y})$ is used to represent the probability density for the state $\boldsymbol{y}$ within the phase space. The property of probability density function gives

$$\int P(\boldsymbol{y})\,\mathrm{d}\boldsymbol{y} = 1. \tag{2.66}$$

The entropy can be characterized by Gibbs entropy formula

$$S = -\int ... \int P(\boldsymbol{y})\ln P(\boldsymbol{y})\,\mathrm{d}y_1 ... \mathrm{d}y_{N_4}. \tag{2.67}$$

Energy and enstrophy remain invariant in each state, causing their average values to remain constant and be equal to their initial values. The averaged energy and enstrophy can be expressed as

$$\langle E\rangle = \tfrac{1}{2}\int ... \int (y_1^2 + ... y_{n_1}^2 + y_{n_2}^2 + y_{n_3}^2 + y_{n_4}^2 ... + y_{N_4}^2)P(\boldsymbol{y})\,\mathrm{d}y_1 ... \mathrm{d}y_{N_4}, \tag{2.68}$$

$$\langle W\rangle = \tfrac{1}{2}\int ... \int \left(k_1^2 y_1^2 + ... k_n^2(y_{n_1}^2 + y_{n_2}^2 + y_{n_3}^2 + y_{n_4}^2) ... + k_N^2 y_{N_4}^2\right) P(\boldsymbol{y})\,\mathrm{d}y_1 ... \mathrm{d}y_{N_4}, \tag{2.69}$$

respectively. When the system achieves an absolute equilibrium state, the entropy attains its maximum value. Therefore, to obtain $P(\boldsymbol{y})$ for the absolute equilibrium state, it is necessary to maximize Eq. (2.67) under constraints of Eq. (2.66), (2.68), and (2.69). Based on the principles of statistical physics, we know that this maximization yields for $P(\boldsymbol{y})$ the Boltzmann-Gibbs distribution,

$$P(\boldsymbol{y}) = C\exp[-(\alpha E + \beta W)], \tag{2.70}$$

where E and W are functions of $\boldsymbol{y}$, denoted as $E = \sum_{n=1}^{N}\sum_{i=1}^{4} y_{n_i}^2$ and $W = \sum_{n=1}^{N}\sum_{i=1}^{4} k_n^2 y_{n_i}^2$, respectively. C is a constant applied for normalization and is expressed as $C = 1/\int \exp[-(\alpha E + \beta W)]\mathrm{d}\boldsymbol{y}$. α, β serve as Lagrange multipliers.

Upon determining the formula for the probability density $P(\boldsymbol{y})$, the mean value of modal

energy can be computed as

$$
\begin{aligned}
\langle E_n \rangle &= \frac{1}{2}\int (y_{n_1}^2 + y_{n_2}^2 + y_{n_3}^2 + y_{n_4}^2) P(\boldsymbol{y}) \mathrm{d}\boldsymbol{y} \\
&= \frac{1}{2} \frac{\int (\sum_{i=1}^{4} y_{n_i}^2) \exp\left[-\sum_{j=1}^{N} (\alpha+\beta k_j^2) \left(\sum_{i=1}^{4} y_{j_i}^2 \right) \right] \mathrm{d}\boldsymbol{y}}{\int \exp\left[-\sum_{j=1}^{N} (\alpha+\beta k_j^2) \left(\sum_{i=1}^{4} y_{j_i}^2 \right) \right] \mathrm{d}\boldsymbol{y}} \\
&= \frac{1}{2} \frac{\left(\iiiint (\sum_{i=1}^{4} y_{n_i}^2) \exp\left[-(\alpha+\beta k_n^2) \left(\sum_{i=1}^{4} y_{n_i}^2 \right) \right] \mathrm{d}y_{n_1} \mathrm{d}y_{n_2} \mathrm{d}y_{n_3} \mathrm{d}y_{n_4} \right) \left(\int \exp\left[-\sum_{j \neq n} (\alpha+\beta k_j^2) \left(\sum_{i=1}^{4} y_{j_i}^2 \right) \right] \mathrm{d}y_1 ... \mathrm{d}y_{(n-1)_4} \mathrm{d}y_{(n+1)_1} ... \mathrm{d}y_{N_4} \right)}{\left(\iiiint \exp\left[-(\alpha+\beta k_n^2) \left(\sum_{i=1}^{4} y_{n_i}^2 \right) \right] \mathrm{d}y_{n_1} \mathrm{d}y_{n_2} \mathrm{d}y_{n_3} \mathrm{d}y_{n_4} \right) \left(\int \exp\left[-\sum_{j \neq n} (\alpha+\beta k_j^2) \left(\sum_{i=1}^{4} y_{j_i}^2 \right) \right] \mathrm{d}y_1 ... \mathrm{d}y_{(n-1)_4} \mathrm{d}y_{(n+1)_1} ... \mathrm{d}y_{N_4} \right)} \\
&= \frac{1}{2} \frac{\left(\iiiint (\sum_{i=1}^{4} y_{n_i}^2) \exp\left[-(\alpha+\beta k_n^2) \left(\sum_{i=1}^{4} y_{n_i}^2 \right) \right] \mathrm{d}y_{n_1} \mathrm{d}y_{n_2} \mathrm{d}y_{n_3} \mathrm{d}y_{n_4} \right)}{\left(\iiiint \exp\left[-(\alpha+\beta k_n^2) \left(\sum_{i=1}^{4} y_{n_i}^2 \right) \right] \mathrm{d}y_{n_1} \mathrm{d}y_{n_2} \mathrm{d}y_{n_3} \mathrm{d}y_{n_4} \right)} \\
&= \frac{1}{\alpha + \beta k_n^2}.
\end{aligned}
\tag{2.71}
$$

Consequently, using the definition in Eq. (2.32), we can deduce the energy spectrum for 2D isotropic turbulence in the absolute equilibrium state as:

$$
E(k) = \int_{k_n = k} \langle E_n \rangle \, \mathrm{d}\mathcal{S}(k_n) = \frac{2\pi k}{\alpha + \beta k^2}. \tag{2.72}
$$

The Lagrange multipliers α and β are defined by the two inviscid invariants: energy and enstrophy. Moreover, when computing the energy spectrum, we only need the partial density for mode n, which is defined as

$$
P_n(y_{n_1}, y_{n_2}, y_{n_3}, y_{n_4}) \equiv \iiint ... \int P(\boldsymbol{y}) \, \mathrm{d}y_1 ... \mathrm{d}y_{(n-1)_4} \mathrm{d}y_{(n+1)_1} ... \mathrm{d}y_{N_4}. \tag{2.73}
$$

For 2D turbulence, P_n is calculated as

$$
P_n(y_{n_1}, y_{n_2}, y_{n_3}, y_{n_4}) = C' \exp\left[-(\alpha E_n + \beta W_n) \right] \tag{2.74}
$$

where $C' = \iiiint \exp\left[-(\alpha + \beta k_n^2) \left(\sum_{i=1}^{4} y_{n_i}^2 \right) \right] \mathrm{d}y_{n_1} \mathrm{d}y_{n_2} \mathrm{d}y_{n_3} \mathrm{d}y_{n_4}$. The fourth line of Eq. (2.71) can be rewritten as

$$
\langle E_n \rangle = \frac{1}{2} \iiiint (y_{n_1}^2 + y_{n_2}^2 + y_{n_3}^2 + y_{n_4}^2) P_n(y_{n_1}, y_{n_2}, y_{n_3}, y_{n_4}) \mathrm{d}y_{n_1} \mathrm{d}y_{n_2} \mathrm{d}y_{n_3} \mathrm{d}y_{n_4}, \tag{2.75}
$$

which indicates that we can use directly the partial density to calculate the modal energy.

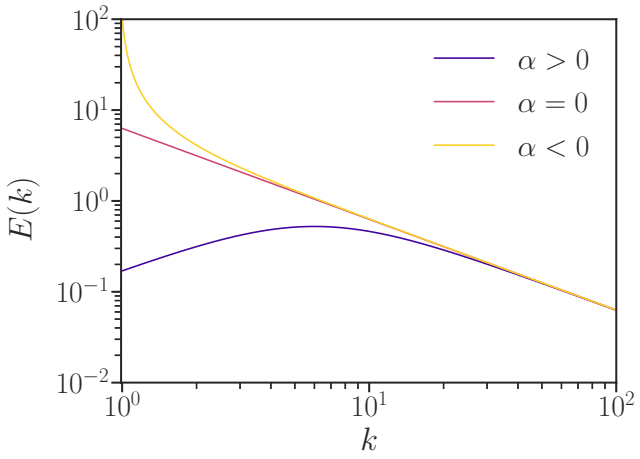

Figure 2.7: Absolute equilibrium energy spectra for 2D turbulence.

The energy spectrum with expression Eq. (2.72) is sketched in Fig. 2.7. The shape of the curve is determined by the values of α and β, which are related to the "temperature" of the system. In statistical mechanics, the temperature of a system can be defined as

$$\frac{1}{T} = \frac{\partial S}{\partial E}. \tag{2.76}$$

In the equilibrium state of 2D turbulence, we can deduce that $\alpha = 1/T$. In Fig. 2.7, β is consistently set to 1 for each curve. In the case where $\alpha = 0$, the energy spectrum is proportional to k^{-1}, signifying an equipartition of enstrophy. In the negative temperature regime where $\alpha < 0$ (specifically, $\alpha = -0.94$ in the example depicted in Fig. 2.7), most energy is concentrated at the largest scales. In contrast, in the positive temperature regime where $\alpha > 0$ (with $\alpha = 36$ as shown in Fig. 2.7), the bulk of the energy is located at $k = \sqrt{\alpha/\beta}$.

For 3D spectrally truncated turbulence, we can employ a similar methodology to derive the energy spectrum formula at the absolute equilibrium state. In 3D turbulence, the inviscid invariants are energy and helicity. The modal energy and helicity can be expressed as

$$E_n = \frac{1}{2}\hat{\boldsymbol{u}}(\mathbf{k}) \cdot \hat{\boldsymbol{u}}^*(\mathbf{k}) = \frac{1}{2}\hat{u}_i(\mathbf{k})\hat{u}_i^*(\mathbf{k}), \tag{2.77}$$

$$H_n = \frac{1}{2}\hat{\boldsymbol{u}}(\mathbf{k}) \cdot \hat{\boldsymbol{\omega}}^*(\mathbf{k}) = \frac{1}{2}\epsilon_{imj}k_m\hat{u}_i(\mathbf{k})\hat{u}_j^*(\mathbf{k}), \tag{2.78}$$

respectively, where ϵ_{imj} is the Levi-Civita symbol. Drawing parallels with the derivations in 2D turbulence, the partial density for mode n in 3D turbulence can also be formulated to

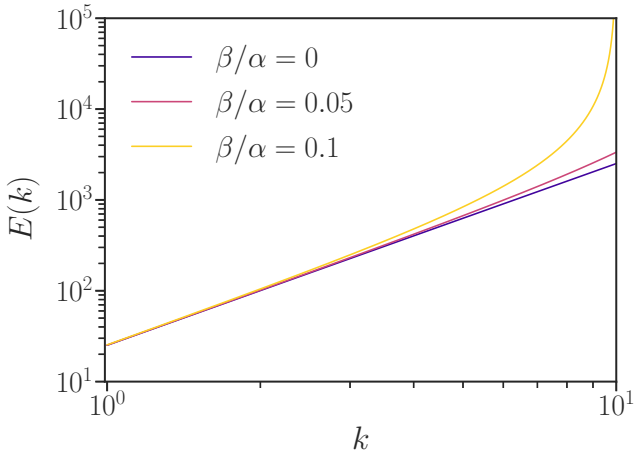

Figure 2.8: Absolute equilibrium energy spectra for 3D turbulence with and without helicity.

satisfy a Boltzmann-Gibbs equilibrium distribution, expressed as:

$$P_n \propto \exp\{-(\alpha E_n + \beta H_n)\}, \tag{2.79}$$

where α and β are Lagrange multipliers associated with energy and helicity, respectively. Then the kinetic energy spectrum at the equilibrium state is derived as

$$E(k) = \frac{8\pi\alpha k^2}{\alpha^2 - \beta^2 k^2}. \tag{2.80}$$

This expression is sketched in Fig. 2.8 with α consistently set to be 1 in all cases. We show how the presence of helicity alters the equilibrium prediction (2.63) for the kinetic energy spectrum for three cases: with value $\beta = 0$ denoting zero helicity, $\beta k_{\max}/\alpha = 1$ with $k_{\max}$ the maximum wavenumber in the truncated system (the maximum helical case), and an intermediate case. Even for the most helical case, the large scales are unaffected, and only the highest wave numbers display the influence of helicity on the energy distribution. These scales are in real turbulence damped by viscous dissipation. From this analysis, Kraichnan concluded that the influence of helicity on 3D turbulence should be small. This was confirmed soon after, using two-point closure [33], and later by direct numerical simulations [49].

Cascades predicted from the absolute equilibrium state

In 3D turbulence, expression (2.80) is radically different from observations of freely evolving 3D Navier-Stokes turbulence, which displays a close to $k^{-5/3}$ wavenumber dependence over

a wide range of scales. However, it can be concluded from this analysis that turbulence with kinetic energy at large scales (small k) will have a tendency to transfer turbulent excitation toward the smaller scales to approach this equilibrium state. Indeed, because the large scales of high-Reynolds-number turbulence are nearly unaffected by viscous stresses, these scales are approximately obeying the Euler equations. For instance, in forced 3D turbulence, an energy spectrum approximately proportional to k^2 (as expression (2.63)) is observed [29, 50] for wave numbers k smaller than the wavenumber associated with the forcing. It implies that if we let these large scales freely evolve, the tendency of the large scales, piloted by the Euler equations, will transfer energy to larger k. In natural systems, viscous dissipation will damp this energy if the wavenumber is large enough. Thus in 3D turbulence, energy transfers from large scales to small scales, where it is eventually dissipated through viscous mechanisms. The application of equilibrium statistical mechanics thus provides insightful perspectives on cascade directions.

In 2D turbulence, the cascade of the two inviscid invariants, energy and enstrophy, can also be predicted from the energy spectrum in the absolute equilibrium state. In the negative temperature case ($\alpha < 0$ in Eq. (2.72)), most energy is concentrated at the largest scales at the absolute equilibrium state, as illustrated in Fig. 2.7. Turbulence tends to approach this maximum entropy state, causing energy to cascade inversely from smaller to larger scales and then form a condensate. The enstrophy spectrum at the absolute equilibrium state can be derived from its relationship with the energy spectrum, $W(k) = k^2 E(k)$. This relationship reveals that most enstrophy is contained at small scales, indicating a forward cascade of enstrophy from larger to smaller scales. This dual cascade was initially predicted by Kraichnan [12] and has since been confirmed by a variety of experimental and numerical simulation studies [51–54]. However, in positive temperature cases ($\alpha > 0$ in Eq. (2.72)), the energy spectrum peaks at $k = \sqrt{\alpha/\beta}$, which complicates the prediction of cascade directions. Experimental observations reveal that the positive temperature results in a state where the both-sign vortices tend to be uniformly neutralized [55]. This phenomenon can be found in quantum turbulence [56, 57] but is relatively uncommon in 2D hydrodynamic turbulence.

2.3.2 Point-vortex statistical mechanics applied to 2D turbulence

The statistical mechanics method introduced in Sec. 2.3.1 yields numerous intriguing outcomes; however, the primary limitation of this method is its applicability solely within spec-

trally truncated systems. In this section, we will introduce another statistical mechanics method: the point-vortex model.

Brief historical overview

In 2D turbulence, the material derivative of vorticity is zero, leading to the conservation of vorticity along material streamlines. Starting from this observation, Onsager [11] used a point-vortex approach for analyzing 2D turbulence by considering continuous 2D turbulence as an ensemble of discrete point vortices. Subsequent research has refined and expanded upon this point-vortex model. Pointin and Lundgren [58] verified that this approach is also applicable to 2D turbulence within bounded containers. The issue of singularity was addressed through the use of regularized potentials [59], the equivalence of micro-canonical and canonical ensembles [60], or a micro-canonical point-vortex ensemble [61]. Building on these developments, Robert and Sommeria [62], along with Miller [63], considered all invariants and established a connection between discrete point vortices and continuous fields by considering coarse-grained 2D turbulence. This theory, later termed the RMS (Robert-Miller-Sommeria) theory, has become one of the most significant contributions to the statistical mechanics of 2D turbulence. The RMS theory has been successfully employed to address a wide array of problems.

The primary motivation behind developing this point-vortex model is to investigate the dynamic mechanisms in 2D turbulence, especially the inverse energy cascade associated with negative temperatures which is defined by Eq. (2.76). Onsager [11] predicted that the system would exhibit negative temperatures beyond a specific interaction energy threshold. Subsequently, Joyce and Montgomery [64] pointed out that, for 2D guiding-center plasma, the value of this energy threshold is zero. The following year, they derived a formula of the system temperature [65]. Yatsuyanagi [55] demonstrated that, in the negative temperature regime, condensation of same-sign vortices is observed, while a uniform distribution of vortex dipoles emerges in the positive temperature case. Apart from temperature, the point-vortex model also allows to derive a hyperbolic sine relation between vorticity and stream function. This hyperbolic sine relation is one of the crucial properties of the condensate in 2D turbulence and can be proved analytically and numerically [66, 67]. In the following, we will present a detailed derivation of this relationship.

This point-vortex model can be employed to investigate the dynamic mechanisms in

various other 2D fluid systems. For instance, this model has been successfully applied to explain the giant vortex clusters in 2D quantum fluids [57, 68], negative temperatures in 2D guiding-center plasmas [64, 69], and the properties of geophysical flows [70, 71].

Sinh relation between vorticity and stream function

Large-scale structuring in 2D and quasi-2D systems has been extensively studied using statistical mechanics [57, 70, 72]. At large but finite Reynolds numbers, a 2D Navier-Stokes fluid will relax to a quasi-static maximum entropy state where most energy is concentrated at large scales. During this evolution, vorticity ω and stream function Ψ relax towards a hyperbolic sine relationship, corresponding to a steady solution of the 2D Euler-equations. More precisely, observations in numerical simulations are consistent with a functional relation

$$\omega = -c^{-1} \sinh(b\Psi), \tag{2.81}$$

where c and b are constants ($c > 0, b < 0$) [66]. This relation was confirmed numerically [66, 67] and explained analytically [62, 73] by applying statistical mechanics to a point-vortex system.

The original idea to use such a point-vortex model came from Onsager. He considered a Hamiltonian system of N parallel point-vortices representing an incompressible and inviscid 2D fluid [11]. Then Joyce and Montgomery used this idea to study the 2D electrostatic guiding center plasma [64, 65], which is analogue to the 2D hydrodynamic turbulent system. The system of interacting point-vortices is equivalent to the system which describes the interaction of very long, uniformly charged rods aligned with a uniform magnetic field. Joyce and Montgomery considered N rods of charge $+e$ and N more of charge $-e$ in a spatial volume $V = L^2$. Then they imagined V subdivided into very small cells of volume $\Delta \ll V$. The cells were large enough, however, to contain many particles. If the locations of particles within one cell are not distinguished, the cell size can be considered zero. Then the entropy can be written as [74]

$$S = \ln \left\{ \left(N! \prod_i \frac{\Delta^{N_i^+}}{N_i^+!} \right) \left(N! \prod_i \frac{\Delta^{N_i^-}}{N_i^-!} \right) \right\} \tag{2.82}$$

where N_i^+ and N_i^- are the number of positive and negative charges inside cell i. All inviscid invariant of this system is the total energy $E = \frac{1}{2} \sum_{i,j} \left(N_i^+ - N_i^- \right) \phi_{ij} \left(N_j^+ - N_j^- \right)$ where

$\phi_{ij} = -(2e^2/l)\ln|\mathbf{r}_i - \mathbf{r}_j| + \text{const.}$ is the Coulomb interaction with $\mathbf{r}_i$ and $\mathbf{r}_j$ locations of the centers of the ith and jth cells. Furthermore, using the elementary combinatorial method of Boltzmann, Joyce and Montgomery assumed $\Gamma^+ = \Sigma_i N_i^+ = N = \text{const.}$ and $\Gamma^- = \Sigma_i N_i^- = N = \text{const.}$ The maximum entropy can be derived by optimization under constraints,

$$\delta S - \beta\delta E - \alpha^+\delta\Gamma^+ - \alpha^-\delta\Gamma^- = 0 \tag{2.83}$$

where β, α^+ and α^- are Lagrange multipliers. Treating the variations of N_i^+ and N_i as independent, we obtain

$$\begin{aligned} &\ln N_i^+ + \alpha^+ + \beta\Sigma_j\phi_{ij}\left(N_j^+ - N_j^-\right) = 0, \\ &\ln N_i^- + \alpha^- - \beta\Sigma_j\phi_{ij}\left(N_j^+ - N_j^-\right) = 0. \end{aligned} \tag{2.84}$$

Finally, this allows to obtain the relation

$$N_i^+ - N_i^- = \exp\left\{-\alpha^+ - \beta\Sigma_j\phi_{ij}\left(N_j^+ - N_j^-\right)\right\} - \exp\left\{-\alpha^- + \beta\Sigma_j\phi_{ij}\left(N_j^+ - N_j^-\right)\right\}, \tag{2.85}$$

which corresponds to a hyperbolic sine when $\alpha^+ = \alpha^-$. We can define a quantity analogous to the vorticity in classical 2D turbulence as

$$\omega = N_j^+ - N_j^-, \tag{2.86}$$

and another quantity analogous to the stream function as

$$\psi = \Sigma_j\phi_{ij}\left(N_j^+ - N_j^-\right). \tag{2.87}$$

This function is a solution to Poisson's equation

$$\nabla^2\psi = -\frac{4\pi e^2}{l}\left(N_j^+ - N_j^-\right). \tag{2.88}$$

Eq. (2.88) for electrostatics is equivalent to the relation between vorticity and stream function, denoted by Eq. (2.6), in 2D turbulence. Hence, relation (2.85) is equivalent to the one between vorticity and stream function in the point-vortex system, as expressed by (2.81).

Discussion

Navier-Stokes turbulence is a dissipative system, whereas the point-vortex dynamics constitute an ideal finite-dimensional Hamiltonian system. The agreement of theory with observations of freely evolving Navier-Stokes turbulence is therefore not a trivial fact. This is

even more the case when a turbulent system is continuously stirred by a body force. In such forced-dissipative systems invariants and Casimirs are continuously modified, so that the application of equilibrium statistical mechanics is not well founded in principle. Nevertheless, on average such approaches might work. Indeed, recently is was observed that maximum entropy theory can be applied to forced-dissipative geostrophic turbulence [75, 76]. Another indication that statistical mechanics might be applied to averaged turbulent systems is the success of the application of statistical mechanics of axisymmetric turbulence [77–79] to observations of experiments of turbulent flows, which are only axisymmetric on average [80]. These ideas will be tested in the following for the dynamics of our turbulence system without vortex stretching.

Chapter 3

Turbulence without vortex stretching

It is important to establish a precise definition of the subject under investigation. In Sec. 3.1, we introduce the governing equation for 3D turbulence without vortex stretching. The vital quantities of a turbulent system are its inviscid invariants, and from the governing equation, we derive the associated global inviscid invariants: enstrophy and helicity in Sec. 3.2. It is important to note that, unlike in classical 2D or 3D turbulence, energy is not conserved in 3D turbulence without vortex stretching. Our investigation of turbulence without vortex stretching includes both analytical studies and numerical simulations. The details of the numerical methods used for this thesis are presented in Sec. 3.3.

3.1 Governing equation

In Chapter 1, we introduced the preliminary concept of turbulence without vortex stretching. This section aims to provide a precise definition of this novel turbulent system by presenting a suitable governing equation.

3.1.1 Equations in physical space

Classical 3D turbulence is governed by the Navier-Stokes equation (2.3), with the vortex stretching mechanism explicitly displayed in the curl of the Navier-Stokes equation (2.4). A straightforward approach to eliminating vortex stretching is to remove it directly from Eq. (2.4). This removal can be obtained by applying an artificial forcing term $\boldsymbol{g}$ that counteracts

vortex stretching

$$\frac{\partial \boldsymbol{\omega}}{\partial t} + (\boldsymbol{u} \cdot \nabla)\boldsymbol{\omega} = (\boldsymbol{\omega} \cdot \nabla)\boldsymbol{u} - \boldsymbol{g}. \tag{3.1}$$

(Here, we first consider a system in the absence of external forces and viscosity.) Substituting directly $\boldsymbol{g} = (\boldsymbol{\omega} \cdot \nabla)\boldsymbol{u}$ eliminates vortex stretching but violates the divergence-free property of the vorticity field. Therefore we write

$$\boldsymbol{g} = (\boldsymbol{\omega} \cdot \nabla)\boldsymbol{u} + \nabla \mathcal{P}_w, \tag{3.2}$$

so that

$$\frac{\partial \boldsymbol{\omega}}{\partial t} + (\boldsymbol{u} \cdot \nabla)\boldsymbol{\omega} = -\nabla \mathcal{P}_w. \tag{3.3}$$

Taking the divergence of Eq. (3.3), we obtain

$$\Delta \mathcal{P}_w = -\nabla \cdot ((\boldsymbol{u} \cdot \nabla)\boldsymbol{\omega}). \tag{3.4}$$

We formally inverse this Poisson equation to obtain

$$\mathcal{P}_w = -\Delta^{-1} \left(\nabla \cdot ((\boldsymbol{u} \cdot \nabla)\boldsymbol{\omega})\right). \tag{3.5}$$

The resulting equation is then

$$\frac{\partial \boldsymbol{\omega}}{\partial t} + \mathbb{P}[(\boldsymbol{u} \cdot \nabla)\boldsymbol{\omega}] = 0 \tag{3.6}$$

where $\mathbb{P} = I - \nabla \Delta^{-1} \nabla \cdot$ represent the projection onto divergence-free fields, with I indicating the identity matrix.

In summary, the governing equation for turbulence without vortex stretching in a general case, incorporating force $\boldsymbol{f}$ and dissipation $\boldsymbol{d}$, is as follows:

$$\frac{\partial \boldsymbol{\omega}}{\partial t} + (\boldsymbol{u} \cdot \nabla)\boldsymbol{\omega} = -\nabla \mathcal{P}_w + \boldsymbol{f} - \boldsymbol{d}. \tag{3.7}$$

3.1.2 Equations in Fourier space

Equation (3.7) presents the form of the governing equation in physical space. However, as we apply the spectral method for numerical simulations in this thesis, it is essential to determine the velocity governing equation in Fourier space.

Using the Fourier representation, the velocity equation can be derived by uncurling Eq. (3.7). Indeed, for an incompressible vector field, we have a simple relation between vorticity and velocity $\nabla \times \boldsymbol{\omega} = \nabla \times \nabla \times \boldsymbol{u} = -\Delta \boldsymbol{u}$. By taking the curl of Eq. (3.7), we obtain the Laplacian of the velocity equation

$$\frac{\partial \Delta \boldsymbol{u}}{\partial t} - \nabla \times ((\boldsymbol{u} \cdot \nabla)\boldsymbol{\omega}) = \nabla \times (\boldsymbol{f} - \boldsymbol{d}). \tag{3.8}$$

Consequently, for the Fourier coefficients $\hat{\boldsymbol{u}}$, we can write

$$\frac{\partial \hat{\boldsymbol{u}}}{\partial t} + \frac{\mathrm{i}}{k^2}\boldsymbol{k} \times \mathcal{F}[\boldsymbol{u} \cdot \nabla \boldsymbol{\omega}] = \hat{\boldsymbol{f}} - \hat{\boldsymbol{d}}, \tag{3.9}$$

where $\mathcal{F}[\bullet]$ denotes the Fourier transform, and $\hat{\boldsymbol{f}}$ and $\hat{\boldsymbol{d}}$ represent the forcing and damping terms applied in Fourier space, respectively. The governing equation in physical space (Eq. (3.7)) includes a pressure term, which allows us to enforce the divergence-free constraint. In Fourier space, this divergence-free condition (Eq. (2.2)) is achieved by projecting the evolution equation (3.9) onto a plane perpendicular to the wave vector.

Our computational code is based on the integration of Eq. (3.9), with further details and implementation to be discussed in Sec. 3.3.

3.2 Inviscid invariants

Inviscid invariants play a significant role in characterizing a system. As introduced in Sec. 2.1.3, in the inviscid, unforced limit, conventional 3D turbulence conserves energy and helicity, while 2D turbulence conserves energy and enstrophy. We have found that in the case of 3D turbulence without vortex stretching, enstrophy and helicity are conserved, whereas kinetic energy is not. This section provides an analytical demonstration of the conservation properties in 3D turbulence without vortex stretching.

3.2.1 Conservation of enstrophy

In this subsection we consider the conservation of enstrophy which is defined as $W = \frac{1}{2}\langle \boldsymbol{\omega} \cdot \boldsymbol{\omega} \rangle$. The vorticity equation of our system is Eq. (3.3). Multiplying by $\boldsymbol{\omega}$ and averaging yields

$$\frac{dW}{dt} = \langle \boldsymbol{\omega} \cdot \big(\nabla \Delta^{-1} \nabla \cdot ((\boldsymbol{u} \cdot \nabla)\boldsymbol{\omega})\big) \rangle. \tag{3.10}$$

Using Eq. (2.7), the RHS can be rewritten as $-\langle(\Delta^{-1}\nabla\cdot((\boldsymbol{u}\cdot\nabla)\boldsymbol{\omega}))\,(\nabla\cdot\boldsymbol{\omega})\rangle$. Incompressibility of vorticity $\nabla\cdot\boldsymbol{\omega}=0$ indicates the RHS of Eq. (3.10) is 0. Then we obtain the conservation of enstrophy for statistically homogeneous, or periodic, flows

$$\frac{dW}{dt}=0. \tag{3.11}$$

3.2.2 Conservation of helicity

The proof of conservation of helicity is somewhat more involved. Helicity is defined as $H=\frac{1}{2}\langle\boldsymbol{\omega}\cdot\boldsymbol{u}\rangle$. The evolution of H can be written using Eq. (2.9) as

$$\frac{dH}{dt}=\left\langle\frac{\partial\boldsymbol{\omega}}{\partial t}\cdot\boldsymbol{u}\right\rangle. \tag{3.12}$$

Multiplying Eq. (3.3) by $\boldsymbol{u}$ and averaging yields

$$\frac{dH}{dt}=-\langle\boldsymbol{u}\cdot(\boldsymbol{u}\cdot\nabla)\boldsymbol{\omega}\rangle+\langle\boldsymbol{u}\cdot\left(\nabla\Delta^{-1}\nabla\cdot((\boldsymbol{u}\cdot\nabla)\boldsymbol{\omega})\right)\rangle. \tag{3.13}$$

Using Eq. (2.7), the second term of RHS can be rewritten as $-\langle(\Delta^{-1}\nabla\cdot((\boldsymbol{u}\cdot\nabla)\boldsymbol{\omega}))\,(\nabla\cdot\boldsymbol{u})\rangle$. Incompressibility of velocity $\nabla\cdot\boldsymbol{u}=0$ indicates this term is 0.

Then we study the first term of RHS of Eq. (3.13). From the vector triple product identity, we can derive the relation Eq. (2.21). So that for the time-evolution of helicity we can write,

$$\frac{dH}{dt}=\langle\boldsymbol{u}\cdot(\nabla\times(\boldsymbol{u}\times\boldsymbol{\omega}))\rangle-\langle\boldsymbol{u}\cdot((\boldsymbol{\omega}\cdot\nabla)\boldsymbol{u})\rangle \tag{3.14}$$

The first term on the right side has the same form with the left-hand-side term of Eq. (2.8). Substituting $\boldsymbol{a}$ with $\boldsymbol{u}$ and $\boldsymbol{b}$ with $\boldsymbol{u}\times\boldsymbol{\omega}$, we can obtain $\langle\boldsymbol{u}\cdot(\nabla\times(\boldsymbol{u}\times\boldsymbol{\omega}))\rangle=\langle\boldsymbol{\omega}\cdot(\boldsymbol{u}\times\boldsymbol{\omega})\rangle=0$. The second term on the right side of Eq. (3.14) can be rewritten as $\langle\boldsymbol{u}\cdot(\boldsymbol{\omega}\cdot\nabla)\boldsymbol{u}\rangle=\langle u_i\omega_j\frac{\partial u_i}{\partial x_j}\rangle$ using the Einstein summation convention. In this identity, u_i, ω_i and x_i are the i-component of velocity, vorticity and position vector respectively. From Eq. (2.7), we have $\langle u_i\omega_j\frac{\partial u_i}{\partial x_j}\rangle=\frac{1}{2}\langle\omega_j\frac{\partial u_iu_i}{\partial x_j}\rangle=-\frac{1}{2}\langle u_iu_i\frac{\partial\omega_j}{\partial x_j}\rangle$. And we can get $\langle\frac{\partial\omega_j}{\partial x_j}\rangle=0$ by the incompressibility of flow, thus $\langle\boldsymbol{u}\cdot((\boldsymbol{\omega}\cdot\nabla)\boldsymbol{u})\rangle=0$. Finally, we obtain

$$\frac{dH}{dt}=0 \tag{3.15}$$

which indicates that helicity is a statistical inviscid invariant of a 3D turbulent system without vortex stretching.

3.2.3 Inviscid invariants in spectrally truncated systems

In numerical simulations, simulating a field with infinite dimensions is not feasible. Instead, we analyze a truncated system, which takes into account only Fourier modes with wave numbers smaller than or equal to a maximum wave number, denoted as $k \leq k_{\max}$. Theoretically, if the maximum wave number is sufficiently large, the truncated system can serve as an approximation of the actual physical system. However, it is not guaranteed that the properties of a truncated turbulent system will correspond precisely to those of actual physical space.

For instance, in 2D turbulence, all Casimir's invariants ω^n, where n represents any positive integer, are inviscid invariants in a physical system. Nevertheless, spectral truncation preserves circulation, energy, and enstrophy [41,81] but fails to maintain higher-order invariants for $n \geq 3$, as supported by the findings in Ref. [82]. In view of this, we will investigate whether enstrophy and helicity remain conserved in a truncated, non-vortex-stretching turbulent system in this subsection. The derivations will be similar to what we presented in Sec. 2.2.3.

In an inviscid, truncated, force-free, and non-vortex-stretching system, the vorticity equation is given as

$$\frac{\partial \boldsymbol{\omega}}{\partial t} + (\boldsymbol{u} \cdot \nabla)\boldsymbol{\omega} = -\nabla \mathcal{P}_w. \tag{3.16}$$

By transforming Eq. (3.16) into Fourier space using Levi-Civita symbols, we obtain

$$\frac{\partial \omega_i(\boldsymbol{k})}{\partial t} = -\mathrm{i}k_j \sum_{\boldsymbol{p}+\boldsymbol{q}=\boldsymbol{k}} \hat{u}_j(\boldsymbol{p})\hat{\omega}_i(\boldsymbol{q}) + \mathcal{F}[-\nabla \mathcal{P}_w] \tag{3.17}$$

where $\boldsymbol{k}$, $\boldsymbol{p}$, $\boldsymbol{q}$ represent wave vectors involved in triad interactions. In Fourier space, the total enstrophy can be calculated as $W = \frac{1}{2}\sum_{\boldsymbol{k}} \hat{\omega}_i(\boldsymbol{k})\hat{\omega}_i^*(\boldsymbol{k})$, as introduced in Sec. 2.2.2. The time derivative of enstrophy can be derived as

$$\frac{\partial W}{\partial t} = \frac{1}{2}\sum_{\boldsymbol{k}} \left(-\mathrm{i}k_j \hat{\omega}_i^*(\boldsymbol{k}) \sum_{\boldsymbol{p}+\boldsymbol{q}=\boldsymbol{k}} \hat{u}_j(\boldsymbol{p})\hat{\omega}_i(\boldsymbol{q}) + \mathrm{i}k_j \hat{\omega}_i(\boldsymbol{k}) \sum_{\boldsymbol{p}+\boldsymbol{q}=\boldsymbol{k}} \hat{u}_j^*(\boldsymbol{p})\hat{\omega}_i^*(\boldsymbol{q}) \right). \tag{3.18}$$

Note that the pressure term does not contribute to enstrophy (nor helicity). In order to achieve a more symmetric equation, we use the relation $\hat{\boldsymbol{u}}(-\boldsymbol{k}) = \hat{\boldsymbol{u}}^*(\boldsymbol{k})$. By doing so, we can obtain the following expression for the time derivative of enstrophy:

$$\frac{\partial W}{\partial t} = \mathrm{Im}[\sum_{\boldsymbol{p}+\boldsymbol{q}+\boldsymbol{k}=\boldsymbol{0}} T(\boldsymbol{k},\boldsymbol{p},\boldsymbol{q})] \tag{3.19}$$

with $T(\boldsymbol{k},\boldsymbol{p},\boldsymbol{q}) = k_j\hat{u}_j(\boldsymbol{q})\hat{\omega}_i(\boldsymbol{q})\hat{\omega}_i(\boldsymbol{k})$ and Im[$\bullet$] the imaginary part of a complex number. For a given set of triad-interaction wave vectors $\{\boldsymbol{k},\boldsymbol{p},\boldsymbol{q}\}$, we can observe that

$$\begin{aligned} T(\boldsymbol{k},\boldsymbol{p},\boldsymbol{q}) + T(\boldsymbol{k},\boldsymbol{q},\boldsymbol{p}) + T(\boldsymbol{p},\boldsymbol{k},\boldsymbol{q}) + T(\boldsymbol{p},\boldsymbol{q},\boldsymbol{k}) + T(\boldsymbol{q},\boldsymbol{k},\boldsymbol{p}) + T(\boldsymbol{q},\boldsymbol{p},\boldsymbol{k}) = \\ k_j\hat{u}_j(\boldsymbol{p})\hat{\omega}_i(\boldsymbol{q})\hat{\omega}_i(\boldsymbol{k}) + k_j\hat{u}_j(\boldsymbol{q})\hat{\omega}_i(\boldsymbol{p})\hat{\omega}_i(\boldsymbol{k}) + p_j\hat{u}_j(\boldsymbol{k})\hat{\omega}_i(\boldsymbol{q})\hat{\omega}_i(\boldsymbol{p}) + \\ p_j\hat{u}_j(\boldsymbol{q})\widehat{\omega}_i(\boldsymbol{k})\hat{\omega}_i(\boldsymbol{p}) + q_j\hat{u}_j(\boldsymbol{k})\hat{\omega}_i(\boldsymbol{p})\hat{\omega}_i(\boldsymbol{q}) + q_j\hat{u}_j(\boldsymbol{p})\hat{\omega}_i(\boldsymbol{k})\hat{\omega}_i(\boldsymbol{q}) \end{aligned} \tag{3.20}$$

This equation can be simplified by applying the relation $\boldsymbol{k}+\boldsymbol{p}+\boldsymbol{q} = \boldsymbol{0}$. For example, we can simplify the term $k_j\hat{u}_j(\boldsymbol{p})\hat{\omega}_i(\boldsymbol{q})\hat{\omega}_i(\boldsymbol{k}) + q_j\hat{u}_j(\boldsymbol{p})\hat{\omega}_i(\boldsymbol{k})\hat{\omega}_i(\boldsymbol{q}) = -p_j\hat{u}_j(\boldsymbol{p})\hat{\omega}_i(\boldsymbol{q})\hat{\omega}_i(\boldsymbol{k})$. We then utilize the incompressibility condition, which gives $p_j\hat{u}_j(\boldsymbol{p}) = 0$, to show that $T(\boldsymbol{k},\boldsymbol{p},\boldsymbol{q}) + T(\boldsymbol{q},\boldsymbol{p},\boldsymbol{k}) = 0$. Similarly, the other terms in the equation can be simplified. Through these simplifications, we ultimately deduce that $T(\boldsymbol{k},\boldsymbol{p},\boldsymbol{q}) + T(\boldsymbol{k},\boldsymbol{q},\boldsymbol{p}) + T(\boldsymbol{p},\boldsymbol{k},\boldsymbol{q}) + T(\boldsymbol{p},\boldsymbol{q},\boldsymbol{k}) + T(\boldsymbol{q},\boldsymbol{k},\boldsymbol{p}) + T(\boldsymbol{q},\boldsymbol{p},\boldsymbol{k}) = 0$, which demonstrates that enstrophy is conserved by each triad of interacting wave vectors, and hence is an inviscid invariant in a truncated system.

Furthermore, using the same method, we can prove the conservation of helicity, which is more complicated and requires software capable of symbolic computation, such as Mathematica. It can be shown that helicity is also conserved triad by triad in a spectrally truncated system.

3.3 Numerical method

This section elucidates the numerical method we have used throughout this thesis. Additionally, it provides specific details about the dissipation and forcing terms in the governing equation, as given in Eq. (3.9).

3.3.1 Numerical setup

We conduct Direct numerical simulations (DNS) for turbulence without vortex-stretching on cubic grids of size N_{grid}^3, where N_{grid} denotes the number of grid points in each direction and is selected as an even integer. Our computational domain consists of a cubic box exhibiting periodicity in three dimensions with a length of side $L = 2\pi$. This periodicity feature allows us to apply the spectral method, and the unit wave vector is $\Delta k = 2\pi/L = 1$. Our computational codes are based on the integration of the velocity equation in Fourier space, as specified in Eq. (3.9). Additionally, a standard pseudo-spectral solver is used to calculate

the nonlinear term in Eq. (3.9), which means the nonlinear term $(\boldsymbol{u}\cdot\nabla)\boldsymbol{\omega}$ is first computed in physical space, and then transformed into Fourier space.

In our codes, we store the Fourier components of velocities for wave vectors whose y- and z- components lie within $-(\frac{N_{\mathrm{grid}}}{2}-1)\Delta k \leq k_y, k_z \leq \frac{N_{\mathrm{grid}}}{2}\Delta k$. However, in the x direction, Fourier components are stored for $0 \leq k_x \leq (N_{\mathrm{grid}}-1)\Delta k$, i.e., only Fourier components for $k_x \geq 0$ need to be stored, which is because the conjugate symmetry of velocity (Eq. (2.26)) guarantees that Fourier components for $k_x < 0$ can be derived from those for $k_x \geq 0$.

It is to be noted that the nonlinear term can induce an aliasing error in a system with finite spectral truncation. To remove this aliasing error, we apply the *2/3 dealiasing rule*, which means setting the Fourier mode with corresponding wave number $|\boldsymbol{k}| > \frac{2}{3}\times\frac{N_{\mathrm{grid}}}{2}\Delta k = \frac{N_{\mathrm{grid}}}{3}\Delta k$ to zero. Therefore, the maximum wave number of the system is $k_{\max} = [\frac{N_{\mathrm{grid}}}{3}]\Delta k$ where $[\bullet]$ is a floor operation.

Regarding time integration, the third-order Adams-Bashforth scheme is applied. The original code (Delache, Cambon & Godeferd [83]) has been formulated in velocity formulation and customized to enable computation of the governing equation of turbulence without vortex stretching Eq. (3.9) for all simulations in this thesis.

3.3.2 Dissipation

In this subsection, we specify the damping term $\hat{\boldsymbol{d}}$ in the governing equation for the dynamics, Eq. (3.9). In our simulations, we employ hyperviscosity and hypofriction to implement dissipation at small and large scales, respectively.

Hyperviscosity

Let us first focus on the damping at the small scales of the system.

The most obvious choice for the small-scale damping of a turbulent system is to use viscous dissipation with the damping term

$$\hat{\boldsymbol{d}} = \nu k^2 \hat{\boldsymbol{u}}. \tag{3.21}$$

Subsequently, the energy dissipation rate can be deduced as

$$\epsilon = \int 2\nu k^2 E(k)\mathrm{d}k. \tag{3.22}$$

The characteristic wave number of dissipation can be interpreted as the inverse of Kolmogorov the length scale η [27]

$$k_d = \frac{1}{\eta} = \left(\frac{\epsilon}{\nu^3}\right)^{1/4}. \tag{3.23}$$

Nevertheless, there exist some cases where our focus is limited to the inertial range without focusing too much on the dissipation range. In such cases, we can attempt to reduce the size of the dissipation range by employing *hyperviscosity* [84,85]. The dissipation term under hyperviscosity dynamics is defined by substituting the Laplacian in Eq. (3.23) with the bth power of the Laplacian, expressed as

$$\hat{\boldsymbol{d}} = \nu k^{2b} \hat{\boldsymbol{u}} \tag{3.24}$$

where the condition $b > 1$ is satisfied. Note that the normal viscous dissipation corresponds to $b = 1$. For classical 3D turbulence, we can increase the extent of the inertial range by an order of magnitude using this approach [86]. Consequently, the energy dissipation rate can be computed as

$$\epsilon = \int 2\nu k^{2b} E(k) \mathrm{d}k. \tag{3.25}$$

Hypofriction

In some cases, an inverse cascade is established, necessitating a damping term at the largest scales of the system to attain a steady state.

In 2D turbulence, linear friction (also referred to as bottom friction or air friction) is commonly applied to remove the energy from large scales [87]. The damping term corresponding to linear friction is represented as

$$\hat{\boldsymbol{d}} = \mu \hat{\boldsymbol{u}} \tag{3.26}$$

with μ the friction coefficient.

Analogue to the application of hyperviscosity, to limit the extent of the range influenced directly by large-scale damping, we use a hypofriction [88, 89]. The damping term corresponding to the hypofriction is defined as

$$\hat{\boldsymbol{d}} = \mu k^{-2a} \hat{\boldsymbol{u}} \tag{3.27}$$

with $a > 0$. Note that large-scale linear damping is obtained for $a = 0$. Accordingly, the dissipation rate of energy can be calculated as

$$\epsilon = \int 2\mu k^{-2a} E(k) \mathrm{d}k. \tag{3.28}$$

3.3.3 Forcing

In this subsection, we specify the forcing term $\hat{\boldsymbol{f}}$ in Eq. (3.9).

In classical 3D turbulence, we can expand the inertial range by employing a force that maintains constant energy within each of the first two shells ($0.5 \leq k < 1.5$ and $1.5 \leq k < 2.5$). The ratio between the two shells corresponds to the $-5/3$ scaling law, i.e., we set $\frac{E(2)}{E(1)} = 2^{-5/3}$. This forcing method is widely used in investigations of 3D turbulence [90, 91]. Building on this concept, for the forcing term $\hat{\boldsymbol{f}}$ in turbulence without vortex stretching, we choose an injection mechanism that keeps the energy constant within a narrow wavenumber range around a certain wavenumber k_f. This type of force is called "constant forcing", and the narrow wavenumber range is termed the "forcing range".

A convenient property of this constant forcing, concerning the present investigation of turbulence without vortex stretching, is that it not only injects energy into the system but also injects the two inviscid invariants: enstrophy and helicity. Without an external force, the energy in every shell would eventually reach zero. Hence maintaining constant energy within a wavenumber range facilitates effective energy input to the system. Moreover, energy input inevitably accompanies enstrophy input due to the relationship between the energy and enstrophy spectrum ($W(k) = k^2 E(k)$), so the constant forcing also injects enstrophy.

However, helicity injection is not as straightforward. In order to explain the helicity injection, we present detailed steps of constant force application as follows:

1. Compute energy within the forcing range at the current time step, denoted as $E(t_n, k_f)$.
2. Conduct integration of Eq. (3.9) without the forcing term.
3. Compute the post-integration energy within the forcing range, denoted as $E'(t_n, k_f)$.
4. Compute the rescaling ratio, $r = E(t_n, k_f)/E'(t_n, k_f)$.
5. Calculate the velocity within the forcing range at the next time step. To ensure $E(t_{n+1}, k_f) = E(t_n, k_f)$, velocities must be rescaled as $u(t_{n+1}, k_f) = \sqrt{r} u'(t_n, k_f)$.

Throughout this process, helicity in the forcing range also remains constant as $H(t_{n+1}, k_f) = rH'(t_n, k_f) = H(t_n, k_f)$ due to the linear relationship between vorticity and velocity. Therefore, the amount of helicity injected by the constant force is $H(t_{n+1}, k_f) - H'(t_n, k_f) = (1 - 1/r)H(t_n, k_f)$ which is similar to the injected energy, $(1 - 1/r)E(t_n, k_f)$. Consequently, energy injection cannot be achieved without simultaneous helicity injection, so the constant forcing application also injects helicity, unless the initial helicity is strictly zero.

Moreover, we note that the injected energy is negative when $r < 1$. In this case, the constant forcing can also be considered as dissipation.

Chapter 4

Absolute equilibrium state

[1] In Chapter 3, we introduced the concept of turbulence without vortex stretching. To analyze this new turbulent system, we first consider a spectrally truncated and inviscid system to investigate the behaviors in the absolute equilibrium state. In this chapter, we will begin by employing the statistical physics method proposed by Kraichnan [40, 41] (refer to Section 2.3.1) to predict the energy, enstrophy, and helicity spectra associated with the absolute equilibrium state. Subsequently, we will perform direct numerical simulations to validate our analytical predictions. The progression toward the equilibrium state will be demonstrated, and the final state will be visualized.

The rest of this chapter is organized as follows. In Sec. 4.1, we will derive the statistical mechanics equilibrium predictions for the energy spectrum. The shape of the resulting equilibrium spectrum suggests that in the absence of vortex stretching, helicity might play an important role in the dynamics of turbulence, unlike the classical 3D case. In Sec. 4.2, we present a numerical assessment of the theoretical results, which include analyses of the conserved quantities, equilibrium spectra and the physical-space characterization of the velocity field. Section 4.3 presents the conclusions of this chapter.

4.1 Analytical considerations

In Section 2.3.1, we showed that statistical physics is an effective tool for analyzing a spectrally truncated, inviscid system. In this section, we will provide a detailed derivation of

[1] The results presented in this chapter have been published in Ref. [92].

energy, enstrophy, and helicity spectra for turbulence without vortex stretching at the absolute equilibrium state. The application of helical decomposition, introduced in Sec. 2.2.5, simplifies the derivations.

4.1.1 Statistical equilibrium distributions

In this subsection, we will derive, using tools from statistical mechanics, the spectral energy distribution corresponding to thermal equilibrium of a finite set of Fourier-modes, as presented in Sec. 2.3.1. We refer to Salmon [93] and Thalabard [94] for detailed derivations using the present approach. We consider that the flow is decomposed on a finite number N of Fourier components $\hat{\boldsymbol{u}}(\boldsymbol{k})$. The vector space $\boldsymbol{k}$ is thus decomposed by its coordinates $\boldsymbol{k}_n$, with $n = 1, ..., N$. Note that in this section, the subscript n does not indicate a vector index, but simply a counter. The value N corresponds to the total number of modes. This means that in a 3D cubic domain with N_k modes in each direction, $N = N_k^3$. Note that the Fourier coefficients of velocity satisfy the conjugate symmetry $\hat{\boldsymbol{u}}(\boldsymbol{k}) = \hat{\boldsymbol{u}}^*(-\boldsymbol{k})$, because the velocity is a real quantity in physical space, thus the total number of independent degrees of freedoms of the system is $N/2$.

We consider incompressible flow, where the divergence in Fourier space implies $\boldsymbol{k} \cdot \hat{\boldsymbol{u}}(\boldsymbol{k}) = 0$, so that only two independent Fourier coefficients are needed to represent the velocity vector $\hat{\boldsymbol{u}}(\boldsymbol{k}_n)$. Because, in addition, the Fourier coefficients are complex, a total of four independent real coefficients describe each mode. These modes are denoted $y_{n_1}, y_{n_2}, y_{n_3}, y_{n_4}$, where n ranges from 1 to N. In total therefore, if we have N wave-vector coordinates representing a 3D velocity field, we have to consider the dynamics of a system of $4N$ coordinates in phase space. A convenient way to choose the independent modes will be described now.

Following Ref. [35], [34] and [40], we represent the velocity field of an incompressible 3D fluid by using a helical-mode decomposition. As introduced in Sec. 2.2.5, every 3D Fourier vector $\hat{\boldsymbol{u}}(\boldsymbol{k})$ can be represented by two orthogonal complex helical waves $\boldsymbol{h}_\pm = \hat{\boldsymbol{\zeta}} \times \hat{\boldsymbol{\kappa}} \pm \mathrm{i}\hat{\boldsymbol{\zeta}}$ with $\hat{\boldsymbol{\kappa}} = \boldsymbol{k}/k$ the unit vector parallel to $\boldsymbol{k}$ and i the imaginary unit. Here the unit vector $\hat{\boldsymbol{\zeta}}$ can be chosen as $\hat{\boldsymbol{\zeta}} = \boldsymbol{z} \times \boldsymbol{k}/|\boldsymbol{z} \times \boldsymbol{k}|$ for an arbitrary vector $\boldsymbol{z}$. It then follows that

$$\hat{\boldsymbol{u}}(\boldsymbol{k}) = \hat{u}_+(\boldsymbol{k})\boldsymbol{h}_+(\boldsymbol{k}) + \hat{u}_-(\boldsymbol{k})\boldsymbol{h}_-(\boldsymbol{k})\,. \tag{4.1}$$

Note that $\hat{u}_+(\boldsymbol{k})$ and $\hat{u}_-(\boldsymbol{k})$ are complex numbers.

As stated above, all coordinates $\boldsymbol{k}$ of the considered part of Fourier space are individually labeled $\boldsymbol{k}_n$, with n ranging from 1 to N. Because at each coordinate $\boldsymbol{k}_n$ we have four individual real coefficients $y_{n_1}, y_{n_2}, y_{n_3}, y_{n_4}$, we can thus define using the following representation:

$$\begin{aligned} y_{n_1} &= \mathrm{Re}[\hat{u}_+(\boldsymbol{k}_n)], \quad y_{n_2} = \mathrm{Im}[\hat{u}_+(\boldsymbol{k}_n)], \\ y_{n_3} &= \mathrm{Re}[\hat{u}_-(\boldsymbol{k}_n)], \quad y_{n_4} = \mathrm{Im}[\hat{u}_-(\boldsymbol{k}_n)], \end{aligned} \tag{4.2}$$

where Re[•] and Im[•] represent the real and imaginary part of the quantity in brackets. The main motivation to use the helical mode decomposition in the present investigation is that we have a simple relation between the generalized coordinates and the modal energy, helicity and enstrophy,

$$\begin{aligned} \frac{1}{2}\hat{\boldsymbol{u}}(\mathbf{k}) \cdot \hat{\boldsymbol{u}}^*(\mathbf{k}) &= \hat{u}_+\hat{u}_+^* + \hat{u}_-\hat{u}_-^* \\ &= y_{n_1}^2 + y_{n_2}^2 + y_{n_3}^2 + y_{n_4}^2 = E_n, \end{aligned} \tag{4.3}$$

$$\begin{aligned} \frac{1}{2}\hat{\boldsymbol{u}}(\mathbf{k}) \cdot \hat{\boldsymbol{\omega}}^*(\mathbf{k}) &= k\left(\hat{u}_+\hat{u}_+^* - \hat{u}_-\hat{u}_-^*\right) \\ &= |\boldsymbol{k}_n|\left(y_{n_1}^2 + y_{n_2}^2 - y_{n_3}^2 - y_{n_4}^2\right) = H_n, \end{aligned} \tag{4.4}$$

$$\begin{aligned} \frac{1}{2}\hat{\boldsymbol{\omega}}(\mathbf{k}) \cdot \hat{\boldsymbol{\omega}}^*(\mathbf{k}) &= k^2(\hat{u}_+\hat{u}_+^* + \hat{u}_-\hat{u}_-^*) \\ &= |\boldsymbol{k}_n|^2(y_{n_1}^2 + y_{n_2}^2 + y_{n_3}^2 + y_{n_4}^2) = W_n. \end{aligned} \tag{4.5}$$

In the following, we will use that all four coefficients y_{n_i} correspond to the same position in Fourier space so that we can write $|\boldsymbol{k}_n| = k$. Now that we have defined the invariants as a function of the generalized coordinates y_{n_i} in phase space, we can proceed with the derivation of the equilibrium distribution.

The fundamental principle of equilibrium statistical mechanics states that in systems satisfying a Liouville equation (non-divergent evolution of the generalized coordinates), the probability density $P(\mathbf{y})$ eventually becomes uniform over all accessible parts of phase space (Salmon [93]). We will compute the average spectral energy distribution associated with this thermal equilibrium state. An essential ingredient to compute the average corresponding to this distribution is the probability density. Similar to the derivation presented in Sec. 2.3, the partial density (or partition function) for mode n, $P_n\left(y_{n_1}, ..., y_{n_4}\right)$, is considered to satisfy a Boltzmann-Gibbs equilibrium distribution,

$$P_n\left(y_{n_1}, ..., y_{n_4}\right) = C_n \exp\left[-S_n\right], \tag{4.6}$$

where S_n is a function of the constants of motion and C_n is a constant. For instance, if enstrophy and helicity are conserved, as in our case, the quantity S_n writes

$$S_n = \alpha W_n + \beta H_n, \tag{4.7}$$

where α and β are Lagrange multipliers representing some kind of inverse statistical temperature or chemical potential. The function P_n gives thus the probability to find values y_{n_i} for mode n. It is at this point that the approach of different physical systems is distinct. For 2D turbulence, W_n and the energy E_n would appear, whereas in classical 3D turbulence, E_n and H_n would appear in expression (4.7).

We have thus, substituting definitions (4.4) and (4.5) in (4.6),

$$\begin{aligned} P_n\left(y_{n_1},...,y_{n_4}\right) &= C_n \exp\left[(-k^2\alpha - k\beta)(y_{n_1}^2 + y_{n_2}^2)\right. \\ &+ \left.(-k^2\alpha + k\beta)(y_{n_3}^2 + y_{n_4}^2)\right]. \end{aligned} \tag{4.8}$$

We define Z_n the integral of P_n,

$$Z_n = \iiiint P_n \mathrm{d}y_{n_1}\mathrm{d}y_{n_2}\mathrm{d}y_{n_3}\mathrm{d}y_{n_4}. \tag{4.9}$$

Expression (4.9) has a form of Gaussian integral, and can be further computed as following:

$$\begin{aligned} Z_n &= C_n \left(\int \exp\left[(-k^2\alpha - k\beta)y_{n_1}^2\right]\mathrm{d}y_{n_1}\right)\left(\int \exp\left[(-k^2\alpha - k\beta)y_{n_2}^2\right]\mathrm{d}y_{n_2}\right) \\ &\quad \left(\int \exp\left[(-k^2\alpha + k\beta)y_{n_3}^2\right]\mathrm{d}y_{n_3}\right)\left(\int \exp\left[(-k^2\alpha + k\beta)y_{n_4}^2\right]\mathrm{d}y_{n_4}\right) \qquad (4.10) \\ &= C_n \frac{\pi^2}{k^4\alpha^2 - k^2\beta^2}. \qquad (4.11) \end{aligned}$$

The average enstrophy per mode can be calculated using the partition function P_n, similarly to the approach used to obtain expression (2.75). The formula is given by

$$\begin{aligned} \langle W_n \rangle &= \sum_{i=1..4} \langle k^2 y_{n_i} y_{n_i} \rangle \qquad (4.12) \\ &= \sum_{i=1..4} \frac{1}{Z_n} \iiiint \left[k^2 P_n y_{n_i} y_{n_i}\right] \mathrm{d}y_{n_1}\mathrm{d}y_{n_2}\mathrm{d}y_{n_3}\mathrm{d}y_{n_4}. \qquad (4.13) \end{aligned}$$

Similarly, the average helicity per mode is given by

$$\langle H_n \rangle = \sum_{i=1,2} \langle k y_{n_i} y_{n_i} \rangle - \sum_{i=3,4} \langle k y_{n_i} y_{n_i} \rangle \tag{4.14}$$

$$= \sum_{i=1,2} \frac{1}{Z_n} \iiiint [k P_n y_{n_i} y_{n_i}] \, \mathrm{d}y_{n_1} \mathrm{d}y_{n_2} \mathrm{d}y_{n_3} \mathrm{d}y_{n_4} - \sum_{i=3,4} \frac{1}{Z_n} \iiiint [k P_n y_{n_i} y_{n_i}] \, \mathrm{d}y_{n_1} \mathrm{d}y_{n_2} \mathrm{d}y_{n_3} \mathrm{d}y_{n_4}. \tag{4.15}$$

From Eq. (4.6) and Eq. (4.9) it is observed that we can compute the average directly using

$$-\frac{1}{Z_n} \frac{\partial Z_n}{\partial \alpha} = \langle W_n \rangle, \tag{4.16}$$

and similarly

$$-\frac{1}{Z_n} \frac{\partial Z_n}{\partial \beta} = \langle H_n \rangle. \tag{4.17}$$

From the integral (4.11), we determine the enstrophy and helicity,

$$\langle W_n \rangle = \frac{2\alpha k^2}{\alpha^2 k^2 - \beta^2}, \quad \langle H_n \rangle = \frac{2\beta}{\alpha^2 k^2 - \beta^2}. \tag{4.18}$$

The enstrophy spectrum and helicity spectrum are therefore, owing to isotropy,

$$W(k) = \frac{8\pi\alpha k^4}{\alpha^2 k^2 - \beta^2}, \quad H(k) = \frac{8\pi\beta k^2}{\alpha^2 k^2 - \beta^2}. \tag{4.19}$$

so that the kinetic energy spectrum writes

$$E(k) = \frac{8\pi\alpha k^2}{\alpha^2 k^2 - \beta^2}. \tag{4.20}$$

These last expressions are the principal theoretical result of this chapter. An important feature of this expression, in contrast to expression (2.80) derived for classical turbulence, is that in the present case, helicity does mainly affect the large scales. Expressions (4.19) and (4.20) will be verified using simulations in Sec. 4.2.

4.1.2 Integral relations between the enstrophy, helicity and energy for the equilibrium distributions

Because the enstrophy and helicity are conserved quantities of the system, the statistical characterization of our system in statistical equilibrium is completely determined by the

values of the enstrophy and helicity,

$$W = \int_{k_{\min}}^{k_{\max}} k^2 E(k) \mathrm{d}k, \qquad H = \int_{k_{\min}}^{k_{\max}} H(k) \mathrm{d}k \tag{4.21}$$

as soon as we know $k_{\min}$ and $k_{\max}$ and the initial conditions. Indeed, the unknown coefficients α and β in the equilibrium spectra are fully determined by the other parameters. This allows us to predict the expected long time value of the kinetic energy

$$E = \int_{k_{\min}}^{k_{\max}} E(k) \mathrm{d}k, \tag{4.22}$$

as a function of the enstrophy and helicity. Let us illustrate this for the simplest, mirror-symmetric case. For that case we have $\beta = 0$, which leads to

$$W = \int_{k_{\min}}^{k_{\max}} 8\pi \frac{k^2}{\alpha} = \frac{8\pi}{3} \frac{k_{\max}^3 - k_{\min}^3}{\alpha} \approx \frac{8\pi}{3} \frac{k_{\max}^3}{\alpha}, \tag{4.23}$$

which allows us to express α as a function of W and $k_{\max}$, where we used that $k_{\min} \ll k_{\max}$. Substituting this in the kinetic energy spectrum and integrating yields

$$E \approx 3 \frac{W}{k_{\max}^2}. \tag{4.24}$$

so that we have a prediction for the final value of the kinetic energy as a function of the initial condition for W. When both helicity and enstrophy are non-zero, the computation becomes more tedious, but can still be performed analytically. We introduce the ratio $\gamma = \beta/\alpha$ so that the helicity spectrum writes

$$H(k) = \frac{8\pi\gamma}{\alpha} \frac{k^2}{k^2 - \gamma^2}. \tag{4.25}$$

For this expression to make sense, the minimum wavenumber should verify $k_{\min} > |\gamma|$, because the enstrophy spectrum must be positive at each wavenumber. Under this constraint, we can integrate the helicity spectrum to obtain the expression [2]

$$H = \frac{8\pi\gamma}{\alpha} \left(k_{\max} - k_{\min} + \frac{\gamma}{2} \ln \left(\frac{(k_{\max} - \gamma)(k_{\min} + \gamma)}{(k_{\max} + \gamma)(k_{\min} - \gamma)} \right) \right), \tag{4.26}$$

which relates the helicity to $k_{\max}$, $k_{\min}$, α and β. For the helical cases, the relation between energy and helicity is simply $E = H/\gamma$.

[2] An error exists within Eq. (3.34) of Ref. [92]. Nevertheless, this error does not influence the results.

4.2 Numerical simulations

In this section, we will assess numerically the conservation of enstrophy and helicity. Subsequently we will check our predictions from statistical mechanics and show visualizations of the equilibrium state.

We integrate Eq. (3.9) without forcing and damping mechanism, i.e., $\hat{\boldsymbol{f}} = 0$ and $\hat{\boldsymbol{d}} = 0$. And our computational domain consists of a periodic box in three dimensions with a length of side $L = 2\pi$ and a grid of size 128^3. Higher resolutions do not seem necessary to assess the analytical results in the present case. Aliasing errors are removed using the 2/3 rule, as introduced in Sec. 3.3. Thus the maximum wave number is $k_{\max} = [\frac{128}{3}] \times \frac{2\pi}{L} = 43$ and the minimum wave number is $k_{\min} = \frac{2\pi}{L} = 1$.

4.2.1 Initial conditions

The initial energy spectrum is defined as

$$E(k) = C_E \, (k/k_0)^4 \, e^{-2(k/k_0)^2} \tag{4.27}$$

with $k_0 = 2.52$ and C_E a constant. The initial complex arguments of velocity in Fourier space are chosen randomly. This method generates initial fields with non-zero helicity. We want to test our predictions for both mirror-symmetric flows and flows with mean helicity. To generate a helicity-free flow it is in principle possible to manipulate the phases of the Fourier modes, but we have used a more intuitive manner by combining two velocity fields.

We generate two velocity fields $\boldsymbol{u}_a$ and $\boldsymbol{u}_b$ with identical energy spectra but different random phases. Then a helicity-free velocity field can be created by a linear combination of these two fields as $\boldsymbol{u}_c = \boldsymbol{u}_a + \lambda \boldsymbol{u}_b$. The constant λ will be determined now. We first introduce the notation

$$h_{ab} \equiv \frac{1}{2} \langle \boldsymbol{u}_a \cdot \boldsymbol{\omega}_b \rangle. \tag{4.28}$$

The mean helicity of field $\boldsymbol{u}_c$ is

$$\begin{aligned} H_c \equiv h_{cc} &= \frac{1}{2} \langle \boldsymbol{u}_c \cdot \boldsymbol{\omega}_c \rangle = \frac{1}{2} \langle (\boldsymbol{u}_a + \lambda \boldsymbol{u}_b) \cdot (\boldsymbol{\omega}_a + \lambda \boldsymbol{\omega}_b) \rangle \\ &= \frac{1}{2} (h_{aa} + \lambda (h_{ab} + h_{ba}) + \lambda^2 h_{bb}). \end{aligned} \tag{4.29}$$

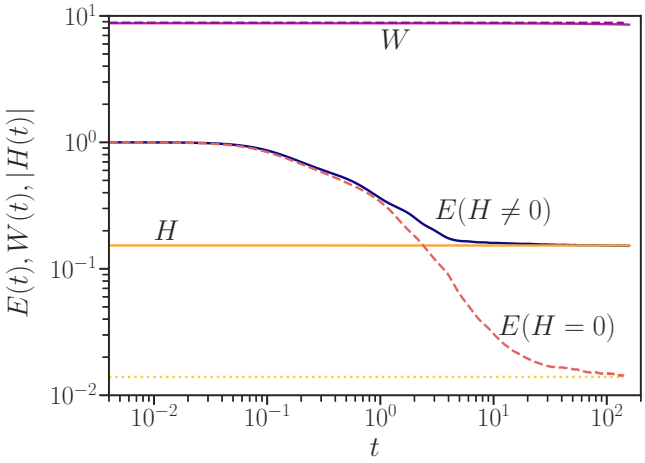

Figure 4.1: Time evolution of energy, enstrophy and helicity for the inviscid, force-free, 3D, no vortex-stretching turbulence: solid lines, helical case; dashed lines, mirror-symmetric case; dotted line, the analytical prediction of the kinetic energy for the mirror-symmetric case.

Because h_{aa}, h_{bb}, h_{ab}, h_{ba} can all be computed directly, the condition $H_c = 0$ yields a quadratic equation for λ (i.e. Eq. (4.29)=0), which can be solved exactly to determine λ. This procedure allows us to generate a zero-helicity initial condition with prescribed kinetic energy spectrum. Owing to rounding errors, the helicity of the resulting initial condition is of the order of 10^{-4}, which is sufficiently close to zero for our purposes.

4.2.2 Conservation of enstrophy and helicity during relaxation

In Fig. 4.1, we show the time evolution of enstrophy, helicity and kinetic energy. Note that the initial energy E_0 is unity. Time is normalized by a characteristic time scale $\tau = 1/\sqrt{E_0 k_{\min}^2}$. For the case of mirror-symmetric truncated Euler turbulence without vortex stretching, a clear conservation of enstrophy is observed, whereas the kinetic energy decays. Helicity remains negligible throughout the simulation. The prediction of the kinetic energy, discussed in Sec. 4.1.2, is represented by a dotted line. It is observed that the expected steady state is reached for the kinetic energy. This steady state is the predicted equilibrium state, where the Fourier modes all contain, on average, the same amount of enstrophy.

In Fig. 4.1, the same results are also plotted for the helical case. It is observed, as shown

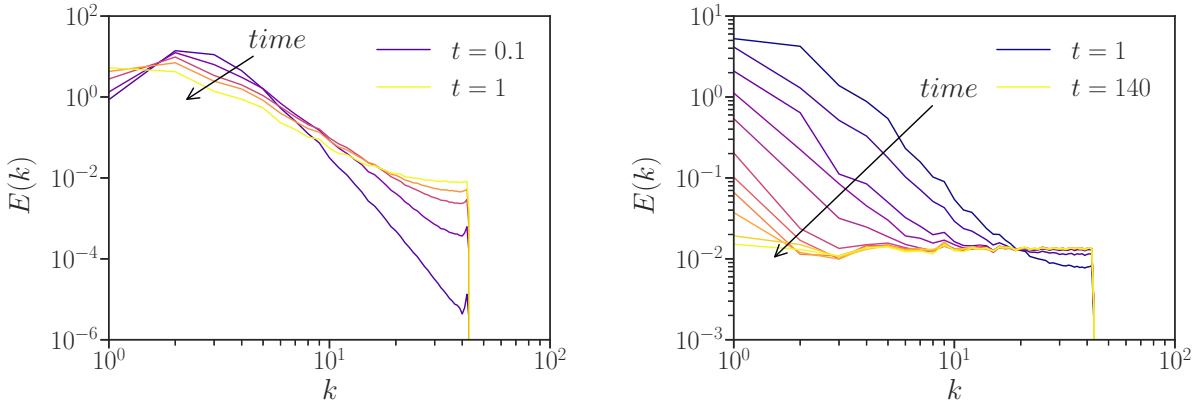

(a) (b)

Figure 4.2: Inviscid relaxation for helicity-free turbulence: (a) short time evolution, showing the kinetic energy spectra at t = 0.1, 0.2,0.4, 0.6, 1; (b) long time evolution, showing the spectra at t = 1, 2, 4, 6, 10, 20, 40, 60, 100, 120, 140.

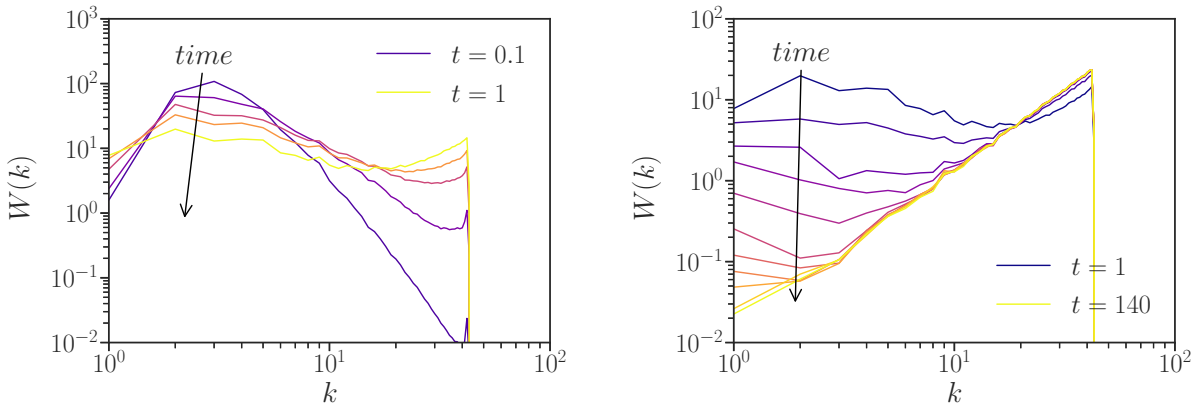

(a) (b)

Figure 4.3: Time evolution of enstrophy spectra helicity-free turbulence: (a) short time evolution; (b) long time evolution. The time-instants are the same as indicated in Fig. 4.2.

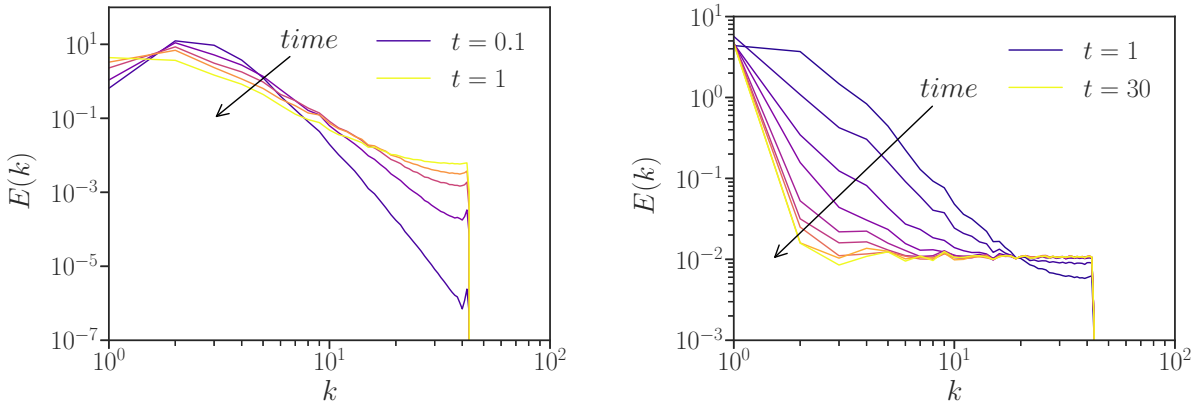

(a) (b)

Figure 4.4: Inviscid relaxation for helical turbulence: (a) Short time evolution, showing the kinetic energy spectra at t = 0.1, 0.2, 0.4, 0.6, 1; (b) long time evolution, showing the spectra at t = 1, 2, 4, 6, 8, 10, 14, 16, 18, 30.

in our proof (Sec. 3.2.2), that helicity is conserved by the system. As mentioned in Sec. 4.1.2, the prediction of the final kinetic energy in the helical case is $E = H/\gamma$. After calculation, we have $\gamma = -0.9989 \approx -1$ in our simulation. This corresponds to the observation that the kinetic energy tends to the absolute value of the helicity. This tendency is not a coincidence, but reflects the condensation of energy into a helical flow structure at scales with wavenumber $k = 1$, as will be shown next. It is also shown that the presence of helicity allows the flow to retain more kinetic energy in the system than the mirror-symmetric case does. Indeed, without helicity, the energy drops to less than 2% of its initial value, while in the helical case, this value is approximately 15%.

To further investigate the dynamics of the truncated system, we show in Fig. 4.2(a,b) the evolution of the kinetic energy spectra towards the equilibrium state. In Fig. 4.3(a,b), it is observed that enstrophy accumulates rapidly in the largest spatial frequencies, in a similar manner as energy accumulates in classical truncated Euler dynamics [95, 96]. This evolution was correctly predicted and explained in [97].

The dynamics of the helical case (Fig. 4.4(a,b)) is quite similar, except for the persistent energy at the smallest wavenumbers. This is anticipated by the statistical mechanics

predictions in Sec. 4.1 and we will focus on them now.

4.2.3 Comparison with predicted shapes

In figure 4.5, we compare the spectra associated with the relaxed state, obtained from the numerical simulations, to the predictions ((4.19) and (4.20)) for the spectra. An excellent agreement is observed. Figure 4.5(a) shows the mirror-symmetric case, where a flat energy spectrum, associated with equidistributed enstrophy is obtained. In this simulation, the predicted formula of the energy spectrum is $E(k) = 0.0131$. We do not show the enstrophy spectrum, which is simply obtained by the energy spectrum multiplied by k^2.

The most flagrant difference between the mirror-symmetric and helical cases is the accumulation of helicity near the infrared cut-off. In figure 4.5(b), we observe this for the energy spectrum, and the same feature is observed for the enstrophy and helicity spectra in figure 4.5(c) and figure 4.5(d), respectively. The amount of energy in this large-scale feature is quite important. Indeed, the $k = 1$ mode contains 87% of the total energy. We will now focus on this energetic, helical mode.

4.2.4 Visualization of the final state

Instantaneous visualizations (at $t = 140$) of the three velocity components and energy and helicity for the final state of the helical case are presented in figures 4.6 and 4.7, respectively. This visualization reveals that our 3D, inviscid, no vortex-stretching system relaxes to a large-scale structure. This could be anticipated from the energy spectrum and is further illustrated in the visualizations because almost all energy and all helicity are contained in the $k = 1$ mode. We observe that the i-component of velocity is nearly independent of the i-direction, where i indicates x, y, or z. Consequently, a plausible 3D structure for this final state is the Arnold-Beltrami-Childress, or ABC, flow. A physical explanation for this, in the light of the statistical mechanics description used here, is that adding the additional constraint of helicity conservation will change the energy and therefore the enstrophy distribution. This will necessarily lead to a decrease of the entropy of the system, because the highest entropy corresponds to enstrophy equipartition. The minimum change in entropy corresponds to a modification of the largest scales of the system. Maximizing the helicity in the largest scales of the system is therefore the most probable reaction of the system. Maximum helicity

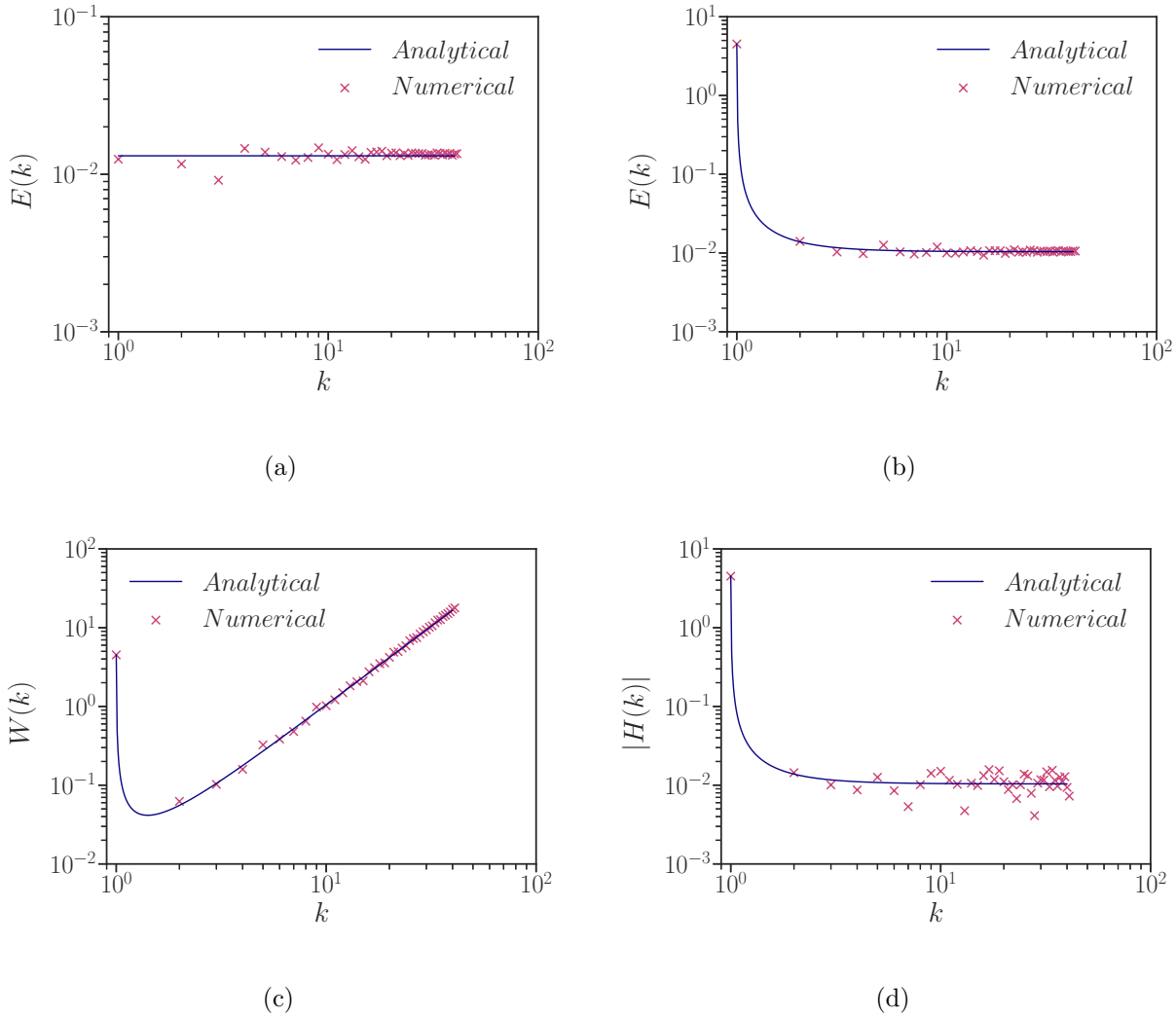

Figure 4.5: Analytical spectra associated with the absolute equilibrium state and numerical spectra. (a) Energy spectrum of the helicity-free case at $t = 140$ with the predicted formula $E(k) = 0.0131$. (b-d) Helical case at $t = 30$. The predicted values of Lagrange multipliers are $\alpha = 2416.6$ and $\beta = -2414.0$. (b) Energy spectrum. (c) Enstrophy spectrum. (d) Absolute value of helicity spectrum.

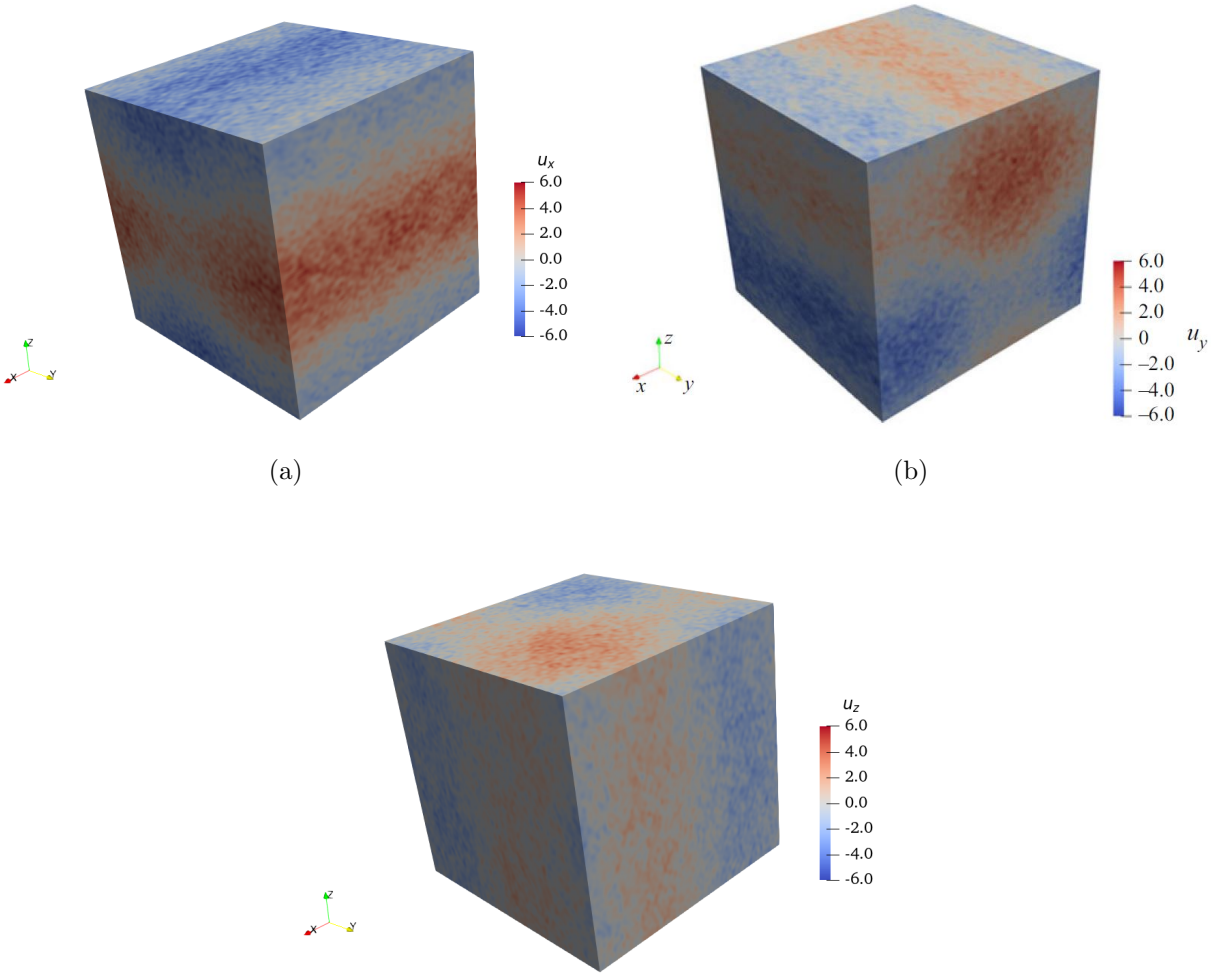

Figure 4.6: Visualizations of the truncated, inviscid, helical system without vortex stretching, obtained from pseudo-spectral computations. (a) x-component of velocity (u_x). (b) y-component of velocity (u_y). (c) z-component of velocity (u_z).

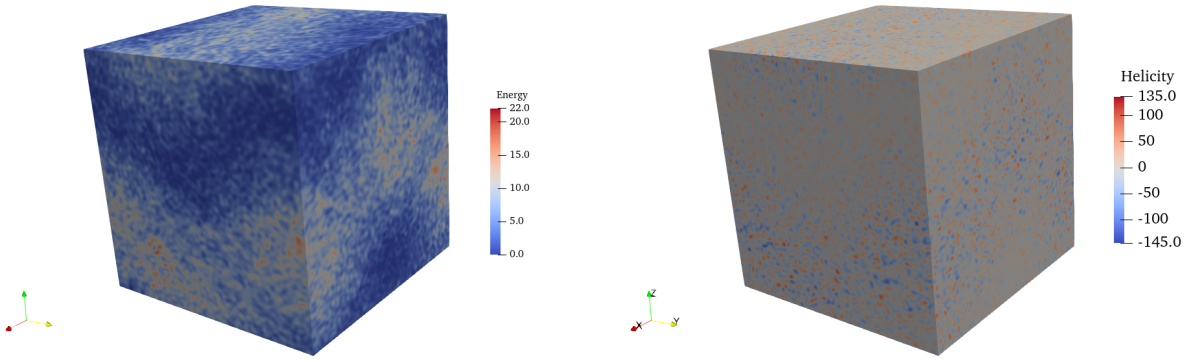

(a) (b)

Figure 4.7: Visualizations of energy and helicity in the truncated, inviscid, helical system without vortex stretching. (a) Energy. (b) Helicity.

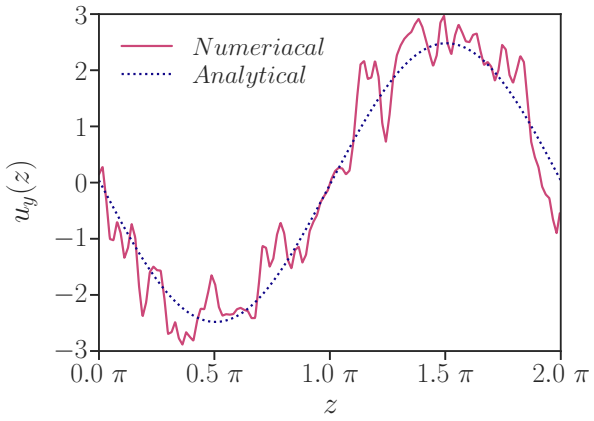

Figure 4.8: Visualization of flow and verification of ABC flow proprieties. Analytical and numerical results of $u_y(z)$ along the line ($x = 0.66L$, $y = 0.5L$).

corresponds to alignment of velocity and vorticity, and thus to an ABC flow. In the following, we verify that the $k = 1$ contribution of the equilibrium state corresponds to such a flow.

The definition of an ABC flow with typical size L is

$$\left.\begin{aligned} u_x =& A\sin\tilde{z} + C\cos\tilde{y}, \\ u_y =& B\sin\tilde{x} + A\cos\tilde{z}, \\ u_z =& C\sin\tilde{y} + B\cos\tilde{x}, \end{aligned}\right\} \tag{4.30}$$

where $\tilde{x}_i = \pm 2\pi x_i/L + \phi_i$. The $\pm$ sign determines the sign of helicity. Simple algebra shows that the parameters A, B, C satisfy the relations

$$\left.\begin{aligned} A^2 =& \left\langle u_x^2 \right\rangle + \left\langle u_y^2 \right\rangle - \left\langle u_z^2 \right\rangle, \\ B^2 =& \left\langle u_y^2 \right\rangle + \left\langle u_z^2 \right\rangle - \left\langle u_x^2 \right\rangle, \\ C^2 =& \left\langle u_z^2 \right\rangle + \left\langle u_x^2 \right\rangle - \left\langle u_y^2 \right\rangle. \end{aligned}\right\} \tag{4.31}$$

We measure at a moment of equilibrium ($t = 140$) $\langle u_x^2 \rangle = 3.7963$, $\left\langle u_y^2 \right\rangle = 4.2210$ and $\langle u_z^2 \rangle = 1.8600$. These figures yield $|A| = 2.4814$, $|B| = 1.5115$ and $|C| = 1.1980$. Averaging the three relations (4.30) for fixed positions x, y, z allows also to determine the phases ϕ_i. Doing so for our simulation, we find $\widetilde{x} = -2\pi x/L - 0.66\pi, \widetilde{y} = -2\pi y/L - 0.25\pi, \widetilde{z} = -2\pi z/L - 0.495\pi$ with $A > 0$, $B > 0$, $C > 0$. Note that values of the parameters A, B, C and the phases ϕ_i change slowly in time.

In figure 4.8, we compare the resulting ABC flow prediction to the results of the simulation for an arbitrary cut through the domain along the z-direction, plotting the y-velocity at $t = 140$. The large-scale flow is indeed consistent with an ABC flow pattern. Superposed upon this large-scale pattern, we observe random fluctuations with a larger spatial frequency, consistent with the spectra we showed in the previous section. All other velocity components in all other directions confirm this behaviour of an ABC structure accompanied by large-frequency noise (not shown).

Furthermore, figure 4.9 presents the visualization of u_y for the helicity-free case at the final state. We observe the absence of large-scale structures, consistent with the energy spectrum predictions, as no large-scale mode contains significantly more energy than the others.

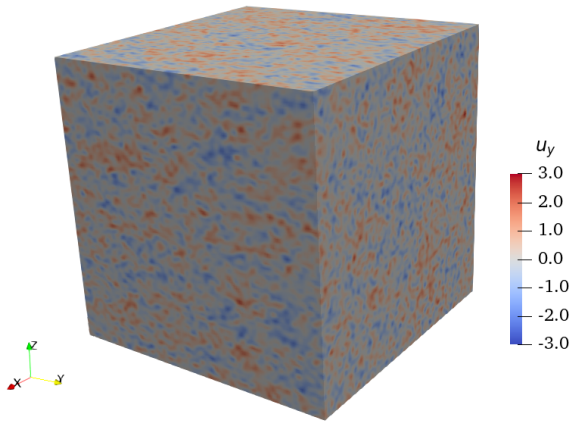

(a)

Figure 4.9: Visualizations of the truncated, inviscid, helicity-free system without vortex stretching. Velocity in the y-direction (u_y).

4.3 Conclusion

The main insight obtained in the present chapter can be summarized by the spectra in figure 4.5. These figures illustrate the statistical equilibrium states of a truncated set of Fourier modes, governed by the Euler equations without vortex stretching. The kinetic energy spectrum is flat for large wavenumbers, as was predicted by Bos [97]. However, the largest scales allowed by the system are strongly affected if the initial conditions contain helicity.

In the absence of helicity, the final state corresponds to a thermal equilibrium of Fourier modes over which enstrophy is evenly distributed, on average. As soon as helicity is present, the helicity allows a condensation of energy in the largest scales of the system. The flow structure associated with this is an Arnold-Beltrami-Childress flow and the energy of this structure is directly determined by the amount of helicity in the system. It is shown in the simulations carried out here that the initial amount of normalized helicity does not need to be very large to have a large influence on the final state. Indeed, because the helicity is conserved, the decrease of the kinetic energy (and constant enstrophy) leads to an increase of its normalized value at the end.

The tendency of the largest scales of the inviscid system to absorb the helicity does have implications for the cascade directions in a forced-dissipative system. Indeed, in turbulence without vortex stretching, enstrophy is preferentially transfered to the large wavenumbers [97]. To approach the equilibrium state, helicity will presumably show a tendency to be transferred to small wavenumbers. The verification of such a novel dual cascade scenario will be presented in Chapter 5.

Chapter 5

Cascades of inviscid invariants

[1] As explained in Sec. 2.2, the dynamics of 2D and classical 3D turbulent flows are very different. In classical 3D turbulence, energy is transferred mainly from the largest towards the smallest scales, with a spectrum proportional to $k^{-5/3}$ in the inertial subrange [10] (k being the wavenumber), and helicity is transferred in the same direction and exhibits a helicity spectrum proportional to $k^{-5/3}$ in the inertial range [33, 49]. In 2D turbulence, energy and enstrophy exhibit a dual and counter-directional cascade, i.e., energy flows towards large scales, and enstrophy flows towards smaller ones. The inertial ranges corresponding to those inverse and forward cascades scale as $k^{-5/3}$ and k^{-3}, respectively [41, 99]. As highlighted in Chapter 2, a crucial distinction between 2D and 3D flows lies in the vortex-stretching mechanism. The primary question we aim to investigate in this chapter is the nature of cascade behaviors when vortex stretching is removed from 3D turbulence.

In Chapter 3 and 4, we showed that helicity and enstrophy are conserved quantities for 3D turbulence without vortex stretching. And we also assessed the dynamics of inviscid turbulence without vortex stretching by statistical mechanics. These results suggest a dual-cascade mechanism and give a prediction of the cascade directions of these two inviscid invariants in a turbulent system without vortex stretching: enstrophy and helicity.

In this chapter, we will investigate the possibility of this dual cascade by assessing the spectral dynamics and its associated fluxes in 3D turbulence without vortex stretching using DNSs. Indeed, in a previous investigation, the forward enstrophy cascade was observed in closure theory [97]. The features of the investigation in this chapter are thus (i) validation

[1] The results presented in this chapter have been published in Ref. [98].

by DNSs of the enstrophy cascade observed in closure theory, (ii) assessment and refinement of the scaling of the energy spectrum in the enstrophy cascade inertial range, (iii) the verification of a dual-cascade mechanism in the presence of helicity, and (iv) the proposition and assessment of scaling arguments for the inertial range of the inverse helicity cascade. Furthermore, we will also examine turbulence where the vortex-stretching term is filtered to retain only local or nonlocal vorticity contributions to the strain-rate tensor. This effort aims to understand the transition from turbulence without vortex stretching toward classical 3D turbulence.

The rest of this chapter is organized as follows. In Sec. 5.1, we will predict the cascade directions and scaling of energy and helicity spectra in turbulence without vortex stretching. In Sec. 5.2, we will present the numerical setup. Then, in Sec. 5.3, we report on the assessment of the theoretical results. Subsequently, in Sec. 5.4, we will study filtered turbulence that retains only local or nonlocal vorticity contributions to the strain-rate tensor. Finally, Sec. 5.5 will conclude the investigation in this chapter.

5.1 Analytical considerations

In this section, we first predict a dual cascade mechanism and cascade directions of the two inviscid invariants in a turbulent system without vortex-stretching: enstrophy and helicity. Then, using dimensional analysis, we propose predictions for energy and helicity spectra in the inertial ranges for a steady system.

5.1.1 Results from statistical mechanics

In Chapter 4, we considered the statistical mechanics of the incompressible Euler equations without vortex-stretching. It was shown that this system conserves enstrophy W and helicity H. In contrast, kinetic energy E is not conserved. When projecting the dynamics of Euler equations without vortex-stretching on a truncated set of Fourier-modes in three dimensions, the equilibrium energy, enstrophy and helicity distributions can be determined, following the methods of Lee [39] and Kraichnan [41] (see Chapter 2). The so-obtained analytical predictions are Eq. (4.19) and (4.20). The equilibrium energy distribution Eq. (4.20) is shown in Fig. 5.1 for cases with and without helicity. This equilibrium energy distribution of the inviscid system allows to formulate predictions of the cascade directions in the nonequilibrium

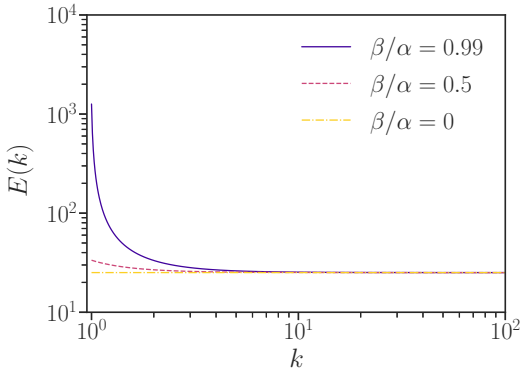

Figure 5.1: Absolute equilibrium energy spectra as predicted by statistical mechanics in Chapter 4. The ratio β/α is associated with the amount of helicity in the system. In the absence of helicity ($\beta = 0$), the energy distribution is flat, corresponding to enstrophy equipartition. The presence of helicity, an invariant of the system, leads to a peaked energy distribution at the large scales.

(turbulent) case. The underlying idea is that a damped-driven system will evolve to approach the statistically most probable state, i.e., the equilibrium state.

The important feature of these equilibrium distributions with respect to the present chapter is that the presence of helicity leads to a modification of the energy distribution at the largest scales allowed by the system. Indeed, comparing the energy spectra in Fig. 5.1 with and without helicity, we observe the presence of a peak at $k = 1$, the smallest wave number. This shows that helicity, and the associated energy has a tendency to concentrate in these scales. If helicity is injected in small scales, then we expect that nonlinear interactions will lead to a flux of helicity towards the large scales. The opposite is expected for enstrophy. Indeed, the equilibrium enstrophy spectrum is shown to be given by $W(k) \sim k^2$ for large k (and also for small k in the absence of helicity). If a dissipation mechanism is present at large wave numbers and enstrophy is initially concentrated at small wave numbers, the nonlinear interactions are expected to have a tendency to redistribute the enstrophy towards large k in an attempt to restore equilibrium.

As explained in Sec. 2.3.1, these reasonings follow closely the ideas by Kraichnan on 2D turbulence [41], which suggested the existence of a dual cascade, with energy and enstrophy

being transferred in opposite directions, and those for helicity transfer in classical 3D turbulence [40], suggesting a unique, forward cascade. In the present case we expect a similar picture as in the 2D case, with enstrophy and helicity being transferred in opposite directions in scale space, and this will be checked numerically in Sec. 5.3.

5.1.2 Inertial range scaling

For turbulent systems with excitations on a wide range of scales, power-spectra exhibit commonly self-similar ranges, where the considered quantity (e.g. the energy density) varies as a power law of the wave number. The most famous example is the inertial range of the kinetic energy spectrum in 3D turbulence, which scales as $E(k) \sim \epsilon^{2/3} k^{-5/3}$ (see Sec. 2.2.2). This expression can be obtained by dimensional analysis, once we assume that the energy dissipation rate ϵ and the wave number k are the quantities determining the dynamics in the inertial range. As a matter of fact, ϵ appears in this expression since it is equal, at high Reynolds numbers and in a steady state, to the flux of energy through scale space from the injection scale to the dissipation range. In the present system, if the dual-cascade scenario is confirmed, the quantities determining the scaling of the energy, helicity, and enstrophy spectra will be the fluxes of enstrophy and helicity.

Let us consider the velocity equation without vortex stretching Eq. (3.7), where we add an external force $\boldsymbol{f}$, acting at a given intermediate length scale k_f, and damping mechanisms $\boldsymbol{d}$, which act dominantly at large and small length scales, characterized by k_μ and k_ν, respectively. The left-hand side of Eq. (3.7) represents the nonlinear advection of vorticity. This term conserves the enstrophy and helicity of the system. Energy is not conserved and can be produced or destroyed by the interaction, somewhat like enstrophy which can be generated in classic 3D turbulence. Therefore, if k_μ and k_ν are far enough removed from the forcing scale k_f, enstrophy and helicity should either pile up around k_f or be transferred to smaller or larger scales. A sketch of energy spectrum presenting the dual cascade is shown in Fig. 5.2.

Following the reasoning in Section 5.1.1, we suppose that in a homogeneous turbulent flow governed by Eq. (3.7) at a sufficiently high Reynolds number, the statistics of the energy density in the inertial ranges have universal forms. For the forward enstrophy cascade and the inverse helicity cascade ranges, these universal forms are expected to be uniquely determined by the flux of enstrophy $\Pi_W(k)$ and helicity $\Pi_H(k)$, respectively. These fluxes

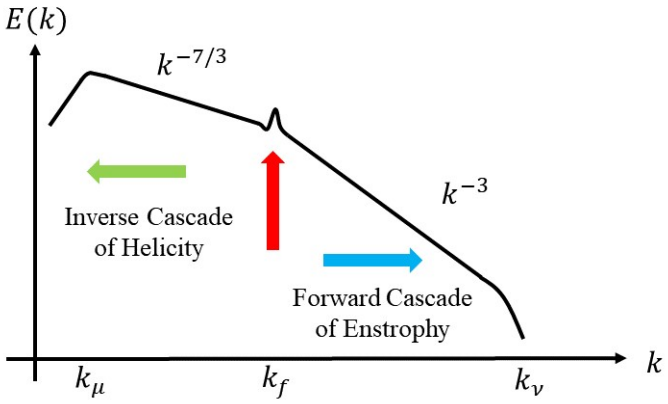

Figure 5.2: Log–log sketch of the energy spectrum in 3D turbulence without vortex stretching.

are defined as

$$\Pi_W(k) = -\int_{\sum_k} \mathrm{Re}\left[\hat{\boldsymbol{N}}(\boldsymbol{k})\cdot\hat{\boldsymbol{\omega}}^*(\boldsymbol{k})\right] d\boldsymbol{k}, \tag{5.1}$$

$$\Pi_H(k) = -\int_{\sum_k} \mathrm{Re}\left[\hat{\boldsymbol{N}}(\boldsymbol{k})\cdot\hat{\boldsymbol{u}}^*(\boldsymbol{k})\right] d\boldsymbol{k}, \tag{5.2}$$

where $\sum_k$ is the spherical domain in Fourier space consisting of all wave vectors with $||\boldsymbol{k}|| \leq k$. And the vorticity advection nonlinearity is indicated by

$$\hat{\boldsymbol{N}}(\boldsymbol{k}) = \mathcal{F}[-(\boldsymbol{u}\cdot\nabla)\boldsymbol{\omega}]. \tag{5.3}$$

By dimensional analysis, this hypothesis leads to the predictions for the inverse cascade range $k_\mu \ll k \ll k_f$,

$$E(k) \sim \Pi_H(k)^{2/3}k^{-7/3}, \tag{5.4}$$

$$H(k) \sim \Pi_H(k)^{2/3}k^{-4/3}, \tag{5.5}$$

and analogously for the forward cascade range $k_f \ll k \ll k_\nu$,

$$E(k) \sim \Pi_W(k)^{2/3}k^{-3}, \tag{5.6}$$

$$H(k) \sim \Pi_W(k)^{2/3}k^{-2}. \tag{5.7}$$

Expression (5.6) can be refined introducing logarithmic corrections, introduced by Kraichnan for inertial range scaling in 2D turbulence [100]. We recall the arguments of Kraichnan here.

It is expected that the flux of enstrophy in the forward cascade range is constant for large wave numbers. Physically, local transfer can be represented by an amount of enstrophy around a wave number k, which is transferred to smaller scales on a timescale $\tau(k)$,

$$\Pi_W(k) \sim \frac{k^3 E(k)}{\tau(k)}. \tag{5.8}$$

The typical timescale in the inertial range is associated with straining of the structures at scale k by structures at lower wave numbers. Such a straining time is of the order

$$\tau(k) \sim \left(\int_{k_f}^{k} p^2 E(p) dp \right)^{-1/2}. \tag{5.9}$$

Inserting a power law proportional to p^{-3} for the energy spectrum in expression (5.9) introduces directly a logarithmic dependence of $\tau(k)$ on the wave number. This leads therefore to a dependence of Eq. (5.8) on the wave number. Multiplying Eq. (5.6) by $[\ln(k/k_f)]^\gamma$ and substituting it into expressions (5.8) and (5.9), we find that for $\gamma = -1/3$, the flux becomes independent of the wave number. All these arguments, originally proposed for 2D turbulence, can be transposed directly to the current system, so that we expect that Eq. (5.6) can be refined to

$$E(k) \quad \sim \quad \Pi_W(k)^{2/3} k^{-3} [\ln(k/k_f)]^{-1/3}. \tag{5.10}$$

We expect the helicity spectrum in the enstrophy cascade range also to be affected by this correction.

All these scaling laws will be assessed using DNS in Section 5.3. Note that we will not consider the helicity-free case in the present chapter. Indeed, for the mirror-symmetric case $H(k)$ is trivially zero. Furthermore, in the absence of the inverse helicity cascade, the scales $k_\mu \ll k \ll k_f$ will display an equipartition of enstrophy, associated with an energy spectrum $E(k) \sim k^0$. This equilibrium scaling was assessed in Ref. [97] using closure and in Chapter 4 using DNS for the truncated inviscid system.

5.2 Numerical setup

In Sec. 5.3, the results of numerical simulations are presented in order to assess the scaling properties of turbulence without vortex stretching. In the present section we detail the numerical setup we have used.

5.2.1 Forcing and damping of the system

The governing equation for the dynamics, Eq. (3.9), needs the specification of the forcing and damping terms. For the forcing term $\hat{\boldsymbol{f}}$ we choose an injection mechanism which keeps the energy constant in a narrow wavenumber range around wavenumber k_f, as presented in Sec. 3.3.3. The damping mechanism $\hat{\boldsymbol{d}}$ is somewhat more involved since we expect the establishment of a dual cascade. Since we are concentrating on inertial range scaling without focusing too much on the dissipation range, we will attempt to reduce the size of the latter by using hyperviscosity. Similarly, when an inverse cascade is established, a damping term is required at the largest scales of the system, to be able to attain a steady state. Again, to limit the extent of the range influenced directly by this damping, we use a hypofriction [88, 89]. Hyperviscosity and hypofriction are introduced in Sec. 3.3.2.

The equation that will be solved in Fourier space is,

$$\frac{\partial \hat{\boldsymbol{u}}}{\partial t} + \frac{\mathrm{i}}{k^2}\boldsymbol{k} \times \mathcal{F}[\boldsymbol{u} \cdot \nabla \boldsymbol{\omega}] = \hat{\boldsymbol{f}} - \nu k^{2b}\hat{\boldsymbol{u}} - \mu k^{-2a}\hat{\boldsymbol{u}}, \tag{5.11}$$

with $\nabla \cdot \boldsymbol{u} = 0$. The left-hand side of this equation is the Fourier transform of the Euler equations without vortex stretching, and we discussed the equilibrium statistical mechanics of this system in Chapter 4. The terms on the right-hand side of this system allow us to consider the nonequilibrium features, by introducing forcing, the first term on the right-hand side, and damping at small and large scales, associated with the last two terms, respectively. In order to restrict the direct influence of the damping terms to a smaller wavenumber range, we use the values $a = 1$ and $b = 4$, unless stated differently. The parameters ν and μ represent the hyperviscosity and hypofriction rate, respectively.

Using Eq. (5.11), we can define the dissipation of enstrophy as

$$\begin{aligned} \epsilon_W &= \epsilon_W^\nu + \epsilon_W^\mu & (5.12)\\ &= \int 2\left(\nu k^{2b} + \mu k^{-2a}\right) k^2 E(k) dk. & (5.13) \end{aligned}$$

We distinguish two contributions: ϵ_W^ν, associated with the hyperviscous damping, and ϵ_W^μ, associated with the large-scale friction. Similarly, we define the contributions to the dissipation rate of helicity

$$\begin{aligned} \epsilon_H &= \epsilon_H^\nu + \epsilon_H^\mu & (5.14)\\ &= \int 2\left(\nu k^{2b} + \mu k^{-2a}\right) H(k) dk, & (5.15) \end{aligned}$$

and energy

$$\epsilon_E = \epsilon_E^\nu + \epsilon_E^\mu \tag{5.16}$$

$$= \int 2\left(\nu k^{2b} + \mu k^{-2a}\right) E(k) dk. \tag{5.17}$$

In the case of asymptotically large scale separation, $k_\mu \ll k_f \ll k_\nu$, we expect that the forward helicity flux and inverse enstrophy flux are negligible. In this case we will therefore have, for $k_f \ll k \ll k_\nu$ in a steady state,

$$\Pi_W(k) \approx \epsilon_W^\nu \tag{5.18}$$

and for $k_\mu \ll k \ll k_f$,

$$\Pi_H(k) \approx -\epsilon_H^\mu. \tag{5.19}$$

In the present simulations we will verify to what extent these asymptotic relations are satisfied.

5.2.2 Characteristic length scales and measures of scale separation

The predictions in Section 5.1.2 are supposed to be valid in inertial ranges, i.e., ranges of scales which are well separated from those scales where source and sink terms act. In order to observe clear scaling ranges, scale separation is thus required between the forcing scale k_f and the damping scales k_μ, k_ν, as shown in Fig. 5.2. In studies of three-dimensional turbulence, an inertial range $k_f \ll k \ll k_\nu$ of about one decade in wave number can be observed in state-of-the-art numerical simulations. Dual cascades need scale separation for two simultaneous ranges of wave numbers $k_\mu \ll k \ll k_f$ and $k_f \ll k \ll k_\nu$, and the physical constraints to observe clear dual-cascade behavior with well-developed scaling ranges for both cascades, simultaneously, require very large simulations. For instance, in 2D turbulence, resolutions of 16384^2 grid points were needed to observe a hint of a dual cascade [53]. Whereas, in 3D turbulence, simulations on grids of 10^{12} grid points are nowadays possible [101], such simulations are extremely demanding with respect to numerical resources. It is therefore more convenient to investigate the two cascade ranges separately in individual simulations, by placing the forcing scale either close to k_μ or close to k_ν. This will be carried out in the following, and it will be shown that this approach allows us to accurately probe the inertial ranges of the system.

In the present simulations, the definition of a Reynolds number directly based on the values of ν and the large-scale velocity and integral length scale is not very informative, since we use hyperviscosity and hypofriction. In general the information associated with the Reynolds number which is most important when scaling is investigated is the scale separation between the large and small scales of the flow. We will therefore, instead of the classical Reynolds number, introduce a measure for the scale separation in the different flows.

For the forward cascade of enstrophy, the wave number representing the dissipative scales in a hyperviscous turbulence is given by [102] $k_\nu = (\epsilon_W^\nu/\nu^3)^{1/(6b)}$. Therefore the scale separation in the forward cascade range is represented by the ratio of this wave number and k_f, the wave number characterizing the forcing scale,

$$R_W = \frac{k_\nu}{k_f} = \frac{1}{k_f}\left(\frac{\epsilon_W^\nu}{\nu^3}\right)^{1/(6b)}. \tag{5.20}$$

We will use this kind of Reynolds number to characterize the scale separation in the forward cascade simulations.

Similarly, we can define a friction wave number $k_\mu = (\mu^3/\epsilon_H^\mu)^{1/(6a+1)}$. For the inverse cascade, we will choose the forcing scale to be as close as possible to the dissipation range and the scale k_μ where the friction acts to be as close as possible to the domain size. The scale separation is then characterized by the ratio of the forcing wave number k_f and the wave number k_μ. For this case we define, therefore,

$$R_H = \frac{k_f}{k_\mu} = k_f\left(\frac{\epsilon_H^\mu}{\mu^3}\right)^{1/(6a+1)}, \tag{5.21}$$

which characterizes the extent of the scaling range in the inverse cascade.

The quantities R_W and R_H are thus not strictly Reynolds numbers, but dimensionless quantities which measure the scale separation in the forward cascade and inverse cascade range, respectively. We mention that in 3D Navier-Stokes turbulence the Taylor-scale Reynolds number R_λ measures the scale separation in a similar way. In the presence of normal viscous dissipation, the ratio of the large (integral) scale $\mathcal{L}$ to the smallest (Kolmogorov) scale η is in that case given by $\mathcal{L}/\eta \sim R_\lambda^{3/2}$

5.2.3 Resolutions

DNSs are executed on grids of sizes 128^3, 256^3, and 512^3 to consider different values of R_W and R_H and thereby assess the robustness of the observed scaling ranges.

Simulation cases	v	β	k_v	R_W	μ	α	Forcing
128^3	1×10^{-9}		19	12.67			$E(1) = 10^3$
256^3	$2^{-8} \times 10^{-9}$	4	38	25.33	0	0	$E(2) = 125$
512^3	$2^{-16} \times 10^{-9}$		75	50			$k_f = 1.5$

Table 5.1: Numerical parameters for forward enstrophy cascade simulations.

Simulation cases	v	β	μ	α	k_μ	R_H	$k_f^{(1)}; k_f^{(2)}$
128^3	256×10^{-13}				1.127	13.75	$15; 16$
256^3	10^{-13}	4	0.45	1	0.854	35.71	$30; 31$
512^3	$\frac{1}{256} \times 10^{-13}$				0.648	93.36	$60; 61$

Table 5.2: Numerical parameters for inverse helicity cascade simulations. The energy in the forced-wavenumber shells is kept at a constant value $E\left(k_f^{(1)}\right) = E\left(k_f^{(2)}\right) = 10^{-3}$. The forcing wave number is defined as $k_f = \left(k_f^{(1)} + k_f^{(2)}\right)/2$

The values of the numerical parameters used for the different simulations are summarized in Tables 5.1 and 5.2 for the forward and inverse cascade simulations, respectively.

5.3 Numerical results

In this section we present the results of the numerical integration of Eq. (5.11). The choice of the forced wave number range and the values of μ and ν allows us to study inertial ranges for either the forward enstrophy cascade or the inverse cascade range associated with helicity transfer.

5.3.1 Forward enstrophy cascade

We start by forcing the largest scales of the system: The energy in the largest scales is kept constant in time. In the wave number range $1 \leq k \leq 1.5$ the energy is given a value $E(1) = 10^3$ and for $1.5 < k \leq 2.5$ the energy level is kept at a value $E(2) = 125$. In the simulations the flow attains a statistically steady state where the enstrophy injected in the forcing range is in equilibrium with the enstrophy dissipated by the hyperviscous damping term. Since no scales larger than the forcing scale are available in our domain, no inverse

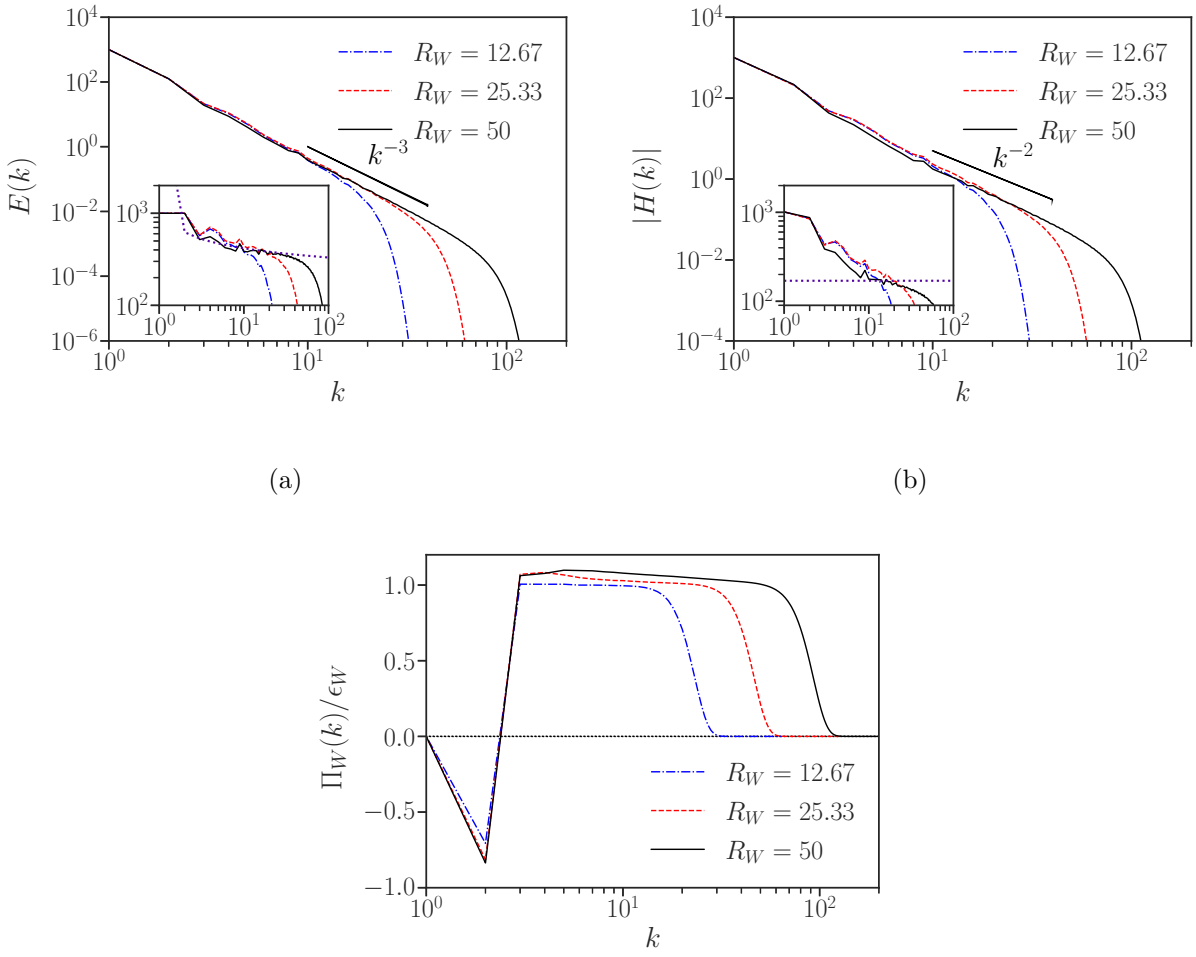

Figure 5.3: Spectra of energy, helicity, and enstrophy flux for the forward enstrophy cascade at different values of the scale-separation number R_W. (a) Energy spectra. The inset shows compensated spectra $k^3E(k)$, and the dotted line in the inset indicates the logarithmic correction [see Eq. (5.10)]. (b) Helicity spectra. Inset: compensated spectra $|k^2H(k)|$. (c) Flux of enstrophy, normalized by the hyperviscous dissipation of enstrophy ϵ_W.

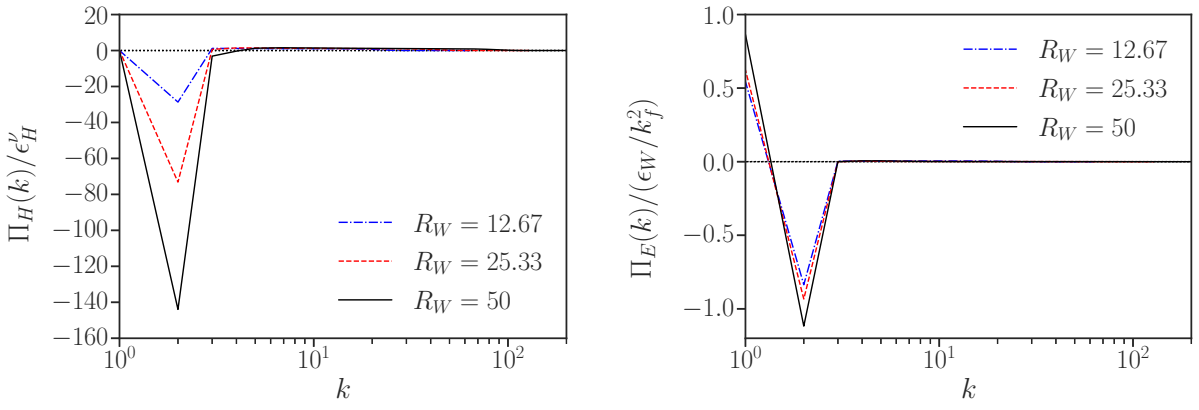

(a) (b)

Figure 5.4: Spectra of helicity and energy flux for the forward enstrophy cascade case at different values of the scale-separation number R_W. (a) Helicity flux spectra, normalized by the hyperviscous dissipation of helicity ϵ_H^ν. (b) Energy flux spectra, normalized by ϵ_W/k_f^2.

cascade can be established, and no large-scale damping is needed to allow for a steady state. The value of μ is therefore chosen zero in these simulations.

In Fig. 5.3(a) and (b) we show energy and helicity spectra, respectively. The insets show their compensated spectra. For the energy spectrum, we can observe that an inertial range is present, with a wavenumber dependence close to k^{-3}, as was also observed in the two-point closure investigation [97]. Similarly, for the helicity spectrum, the exponent is close to k^{-2}. In the inset of Fig. 5.3(a) we show the energy spectra premultiplied by k^3. The inset illustrates that for the largest k, before the dissipation rate is reached, the spectra are approximately flat. The plateau is, however, absent for smaller k. We show in the same inset how a logarithmic correction [cf. Eq.(5.10)] allows us to improve the agreement with the predictions for these scales.

In order to assess that these scaling ranges correspond to constant-flux solutions, we compute the enstrophy flux, defined in Eqs. (5.1). In Fig. 5.3(c), it is observed that a substantial range of wave numbers is observed where the flux is almost constant and approximately equal to ϵ_W^ν. Since the first two modes of the system are forced, there is no space for an inverse cascade to form. Moreover, Fig. 5.4(a) displays the normalized helicity flux spectra by ϵ_H^ν,

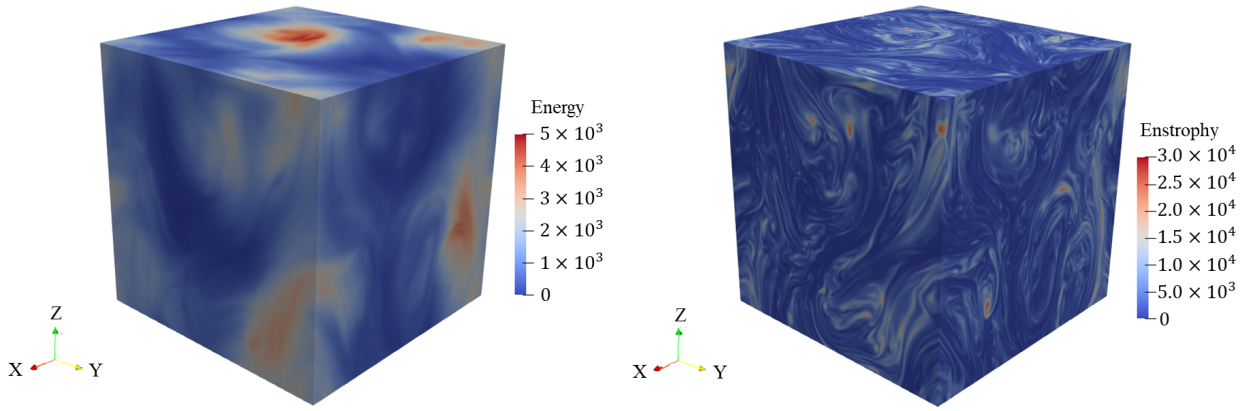

(a) (b)

Figure 5.5: Visualizations of the no-vortex-stretching system forced at large scales for the 512^3 case. ($R_W = 50$) (a) Energy. (b) Enstrophy.

indicating that helicity barely cascades forward, even in the absence of an inverse cascade space. Fig. 5.4(b) presents the energy flux spectra normalized by by ϵ_W/k_f^2. We observe $\Pi_E(k = 0) \neq 0$ because energy conservation does not hold in turbulence without vortex stretching. Similar to helicity, energy scarcely cascades forward.

In Fig. 5.5, enstrophy and energy are visualized for the largest simulation at the largest resolution. The energy plot shows large-scale structures at the forcing scale. The enstrophy shows more fine-grained filamentary structures.

5.3.2 Inverse helicity cascade

After the confirmation of the predictions for the forward cascade of enstrophy in the last section, we now turn to the assessment of the inverse cascade, associated with helicity conservation. We consider the same numerical scheme but change the forcing range to higher wave numbers. We carry out simulations at resolutions of $128^3, 256^3$, and 512^3 associated with three values of the scale-separation parameter R_H. The corresponding forcing scales are now $k_f = 15.5, 30.5$, and 60.5, respectively, for the three considered resolutions.

For all simulations, hyperviscosity and hypofriction are used to render the system station-

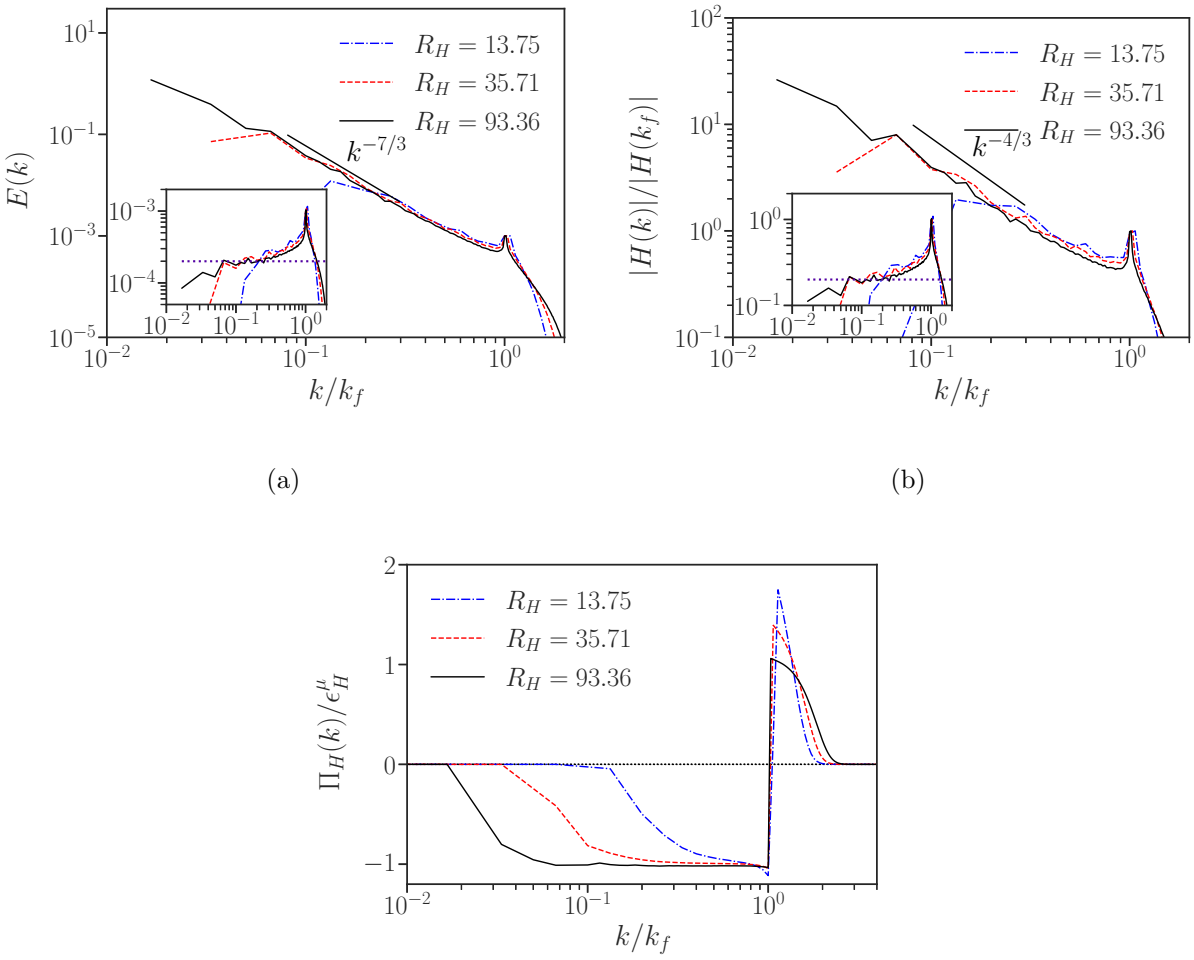

Figure 5.6: Spectra of energy, helicity, and helicity flux for the inverse helicity cascade regime at different values of the scale-separation number R_H. (a) Energy spectra, (b) helicity spectra, and (c) helicity flux spectra. The insets in (a) and (b) show compensated spectra $(k/k_f)^{7/3} E(k)$ and $(k/k_f)^{4/3} |H(k)|/|H(k_f)|$, respectively.

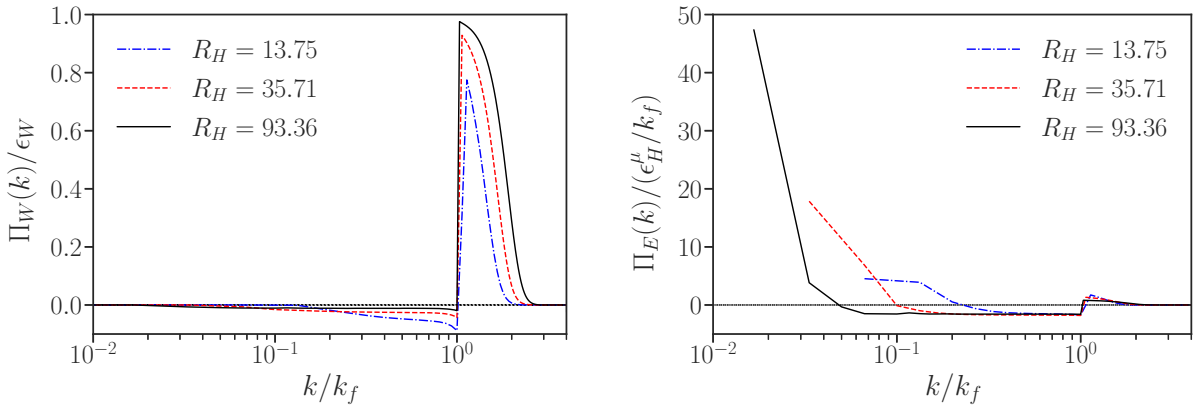

(a) (b)

Figure 5.7: Spectra of enstrophy and energy flux for the inverse helicity cascade regime at different values of the scale-separation number R_H. (a) Enstrophy flux spectra normalized by the dissipation rate of enstrophy ϵ_W, (b) Energy flux spectra, normalized by ϵ_H^μ/k_f.

ary. The numerical parameters are given in Table 5.2. Energy and helicity spectra during the steady state are shown in Figs. 5.6(a) and (b), respectively. We can observe that in the inertial range, the spectral exponent approaches the predictions of Sec. 5.1.2, in particular, for the largest resolution considered here.

The physical picture is further confirmed in Fig. 5.6(c), which shows the helicity fluxes normalized by the hypofriction dissipation rate. It is observed that the flux attains the value of the large-scale dissipation ϵ_H^μ for $k < k_f$. For the largest resolution, a constant flux is observed for more than one decade in wave numbers. Additionally, Fig. 5.7(a) presents the enstrophy flux spectra normalized by the total dissipation rate of enstrophy ϵ_W. We can observe that most enstrophy cascades forward. Fig. 5.7(b) shows the energy flux spectra normalized by ϵ_H^μ/k_f. We observe that the shapes of energy flux spectra are similar to those of helicity flux spectra in the inertial cascade ranges. The forward cascades at wave numbers smaller than inertial ranges result from the condensation of energy at the smallest wave number. In this context, energy can be regarded as being "transported" towards larger scales by helicity.

The spatial kinetic energy distribution and helicity distributions are visualized in Fig. 5.8.

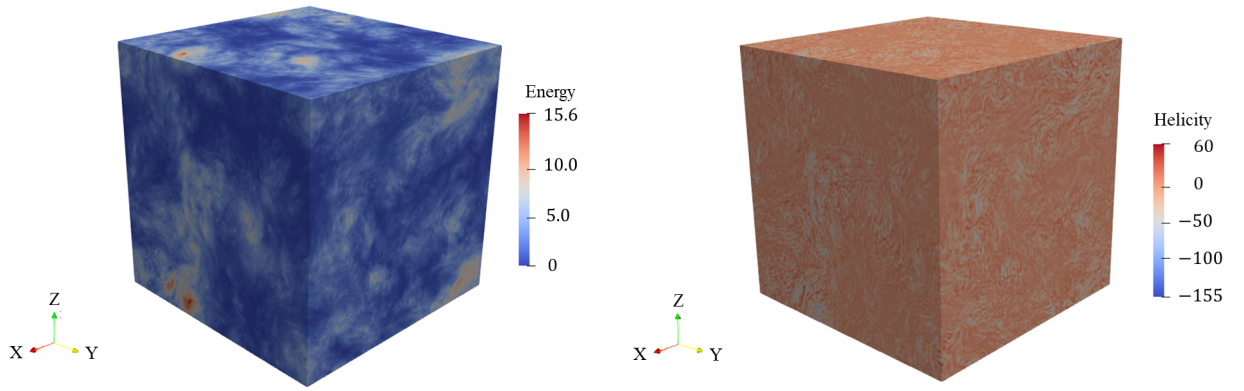

(a) (b)

Figure 5.8: Visualizations of the no-vortex-stretching system forced at small scales for $R_W = 93$. (a) Kinetic energy. (b) Helicity.

We observe that the mean value of the helicity is not zero, but no outstanding large-scale helical features are observed. Clearly, the large-scale friction does prevent the system from generating energetic, helical structures at the box scale.

5.4 Local and non-local contributions to vortex stretching

We observed that the energy scaling in the forward cascade range of turbulence without vortex stretching is k^{-3}, which differs from that of classical 3D turbulence. We are interested in understanding what happens if we remove only a portion of vortex stretching and how turbulence without vortex stretching evolves toward classical 3D turbulence. To this end, we consider turbulence in which the vortex-stretching term is filtered to retain only local or nonlocal vorticity contributions to the strain-rate tensor. Our primary goal is to investigate whether a critical radius of the strain rate tensor exists in this system, around which the turbulence changes its properties. A secondary motivation is to investigate the contributions of local and nonlocal strain on the turbulence dynamics, as proposed in Ref. [19,20]. Indeed, in Ref. [19], the vorticity equation was reformulated in order to separate the vortex-stretching

term into a contribution where the stretching is induced by strain associated with local vorticity and strain resulting from vorticity at a certain distance. To get further insights into these different contributions, we will follow our strategy of comparing a system of turbulence with and without these contributions.

5.4.1 Filtering the vortex stretching

The velocity-gradient tensor can be written as the sum of a symmetric tensor $\mathsf{S}_{ij} = (\partial_j u_i + \partial_i u_j)/2$ and an anti-symmetry tensor $\Omega_{ij} = (\partial_j u_i - \partial_i u_j)/2$. Then the vortex-stretching term in the vorticity equation (Eq. (2.4)) can be written as $(\boldsymbol{\omega} \cdot \nabla)\boldsymbol{u} = \boldsymbol{\omega} \cdot (\mathbf{S} + \boldsymbol{\Omega})$. The anti-symmetry part of the vortex-stretching term follows the relation $\omega_j \Omega_{ij} = -\frac{1}{2}\epsilon_{ijk}\omega_j\omega_k = 0$. It indicates that the dynamics of the vorticity governed by the curl of the Navier-Stokes equation can be expressed by the product of vorticity and the strain-rate tensor, as shown below:

$$\frac{\partial \boldsymbol{\omega}}{\partial t} + \boldsymbol{u} \cdot \nabla \boldsymbol{\omega} = \boldsymbol{\omega} \cdot \mathbf{S} + \nu \Delta \boldsymbol{\omega}, \tag{5.22}$$

with $\nabla \cdot \boldsymbol{u} = 0$, $\boldsymbol{\omega} = \nabla \times \boldsymbol{u}$, $\boldsymbol{u}$ the velocity, ν the kinematic viscosity. The filter we will apply to the Navier-Stokes equations contains a control parameter, the filter width R. Varying this parameter will allow us to evolve the system from the well-known three-dimensional limit to the no-vortex-stretching case. Such a parametric study follows the approaches of Frisch and others [54, 103–107] and allows us to identify critical values or dimensions which are situated in between well-defined limit-cases.

Vortex stretching represents the interaction between vorticity and strain-rate tensor. Recent investigations have attempted to better understand the dynamics of vortex stretching by decomposing the strain-rate tensor into local and non-local parts and assessing their contributions to the turbulent dynamics. Following the method described in this and our previous works (Ref. [97] and Chapter 4), we will focus on the same question not by *a posteriori* considering these contributions in a Navier-Stokes velocity field, but by removing local or non-local parts directly from the governing equations. It means that we will not decompose normal 3D turbulence into local and non-local parts in post-processing but investigate systems between turbulence with and without vortex stretching. Thereto we will consider the following equation,

$$\frac{\partial \boldsymbol{\omega}}{\partial t} + \boldsymbol{u} \cdot \nabla \boldsymbol{\omega} = \boldsymbol{D}(\boldsymbol{\omega}) + \boldsymbol{\omega} \cdot \mathbf{S}^F(R) + \boldsymbol{f}, \tag{5.23}$$

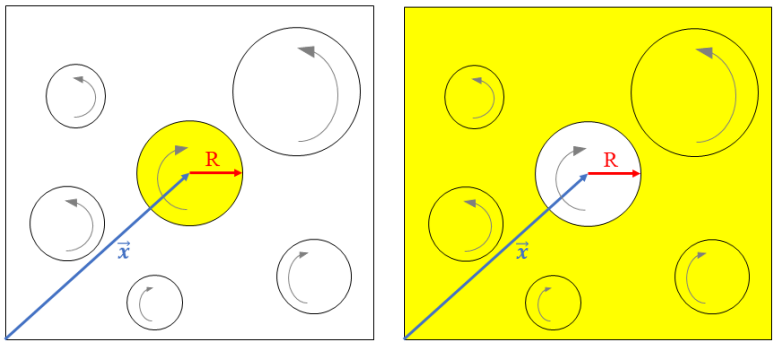

(a) (b)

Figure 5.9: Sketch of the local/non-local contributions of strain to vortex stretching. Only strain rate associated to vorticity in the yellow areas makes contribution to the vortex stretching in point $\boldsymbol{x}$. (a) Local strain cases. (b) Non-local strain cases.

with $\mathbf{S}^F(R)$ the filtered strain-rate tensor.

According to Ref. [19, 20], the strain-rate tensor can be decomposed into local and non-local contributions obtained through Biot-Savart integration of vorticity in a sphere of radius R. Using the same approach, we apply two types of filters to the strain-rate tensor on the vortex-stretching term, most easily defined in Fourier space,

$$\hat{\mathsf{S}}^F_{ij}(\mathbf{k}, R) = \begin{cases} (1 - f(kR))\,\hat{\mathsf{S}}_{ij}(\mathbf{k}) & \text{(local strain)} \\ f(kR)\hat{\mathsf{S}}_{ij}(\mathbf{k}) & \text{(non-local strain)} \end{cases} \tag{5.24}$$

with $f(kR)$ a non-local filter and $1 - f(kR)$ a local filter,

$$f(kR) = \frac{3[\sin(kR) - kR\cos(kR)]}{(kR)^3}$$

and $\hat{\mathsf{S}}_{ij}(\mathbf{k})$ the Fourier transform of the strain rate tensor [20,108]. And we solve two separate systems by retaining local and non-local components of strain, respectively. To physically understand these systems, it is insightful to stress that $f(kR)$ corresponds to a low pass filter, i.e., structures far from the point of vorticity will remain after filtering. The yellow parts in Fig. 5.9 represent the effective strain rate area contributing to the vortex stretching in point $\boldsymbol{x}$. Two limits of the filter $f(kR)$ are $\lim_{R\to 0} f(kR) = 1$ and $\lim_{R\to\infty} f(kR) = 0$. Thus if we use this filter, the system returns to normal 3D turbulence when the radius R

approaches 0 and turbulence without vortex-stretching when R approaches infinity. That is why we call $f(kR)$ a non-local filter. In a system applying the non-local filter, varying R from 0 to 1 allows us to smoothly adapt the dynamics from classical Navier-Stokes to no-vortex stretching turbulence. And obviously, we can obtain the same process by varying R from 1 to 0 in a system applying the local filter $(1 - f(kR))$. The resulting dynamics will be discussed below.

5.4.2 Numerical setup and results

In this part of the investigation, our aim is to understand how turbulence behaves when the vortex stretching is neither completely removed nor completely unmodified. Thereto we simulate turbulence governed by Eq.(5.23) with different radii of filter R and then compare properties of these turbulent systems. All simulations are executed using a grid of 128^3. This modest resolution was chosen in order to carry out a systematic investigation for a large number of filter sizes. The same forcing method as in Sec. 5.3.1 is applied, and the energy spectra of the first two modes are fixed as $E(1) = E(2) = 1$ in each simulation. The conventional viscosity term $\nu\nabla^2\boldsymbol{u}$ is used as the damping mechanism. Thus, the equation of the Fourier-coefficients $\hat{\boldsymbol{u}}$ of turbulence with filtered vortex-stretching is

$$\frac{\partial\hat{\boldsymbol{u}}}{\partial t} = -\nu k^2\hat{\boldsymbol{u}} - \frac{\mathrm{i}}{k^2}\boldsymbol{k}\times\mathcal{F}[(\boldsymbol{u}\cdot\nabla)\boldsymbol{\omega}] + \frac{\mathrm{i}}{k^2}\boldsymbol{k}\times\mathcal{F}[\boldsymbol{\omega}\cdot\boldsymbol{S}^F] + \hat{\boldsymbol{f}} \tag{5.25}$$

with $\nu = \frac{1}{55}$ in all filtered cases. We calculate the following cases: the normal 3D case, no vortex-stretching case, local and non-local strain cases with $R/\eta_0 = 2, 5, 20, 27, 35, 45, 55, 75$ where η_0 is defined as $\eta_0 = 1.8/k_{max} \approx 0.0422$, where k_{max} is fixed by the normal 3D case such that $\eta k_{max} \approx 1.8$ to ensure a good resolution where η is Kolmogorov length scale.

For a filtered vortex-stretching system, there is no inviscid invariant. Fig. 5.10 represents energy, enstrophy, and the absolute value of helicity for different values of the radius R/η_0 in local and non-local strain cases. We expect that in the limit $R \gg \eta_0$ and $R \ll \eta_0$, the local case behaves as the non-local case for $R \ll \eta_0$ and $R \gg \eta_0$, respectively. The $R \gg \eta_0$ limit for the local case and the $R \ll \eta_0$ limit for the non-local case correspond to the standard turbulence limit. In contrast, the the $R \ll \eta_0$ limit for the local case and the $R \gg \eta_0$ limit for the non-local case correspond to the turbulence without vortex stretching limit. In standard turbulence limit, the enstrophy is dramatically amplified in the cascade through vortex stretching [97]. Indeed it is observed that in this limit, the enstrophy is

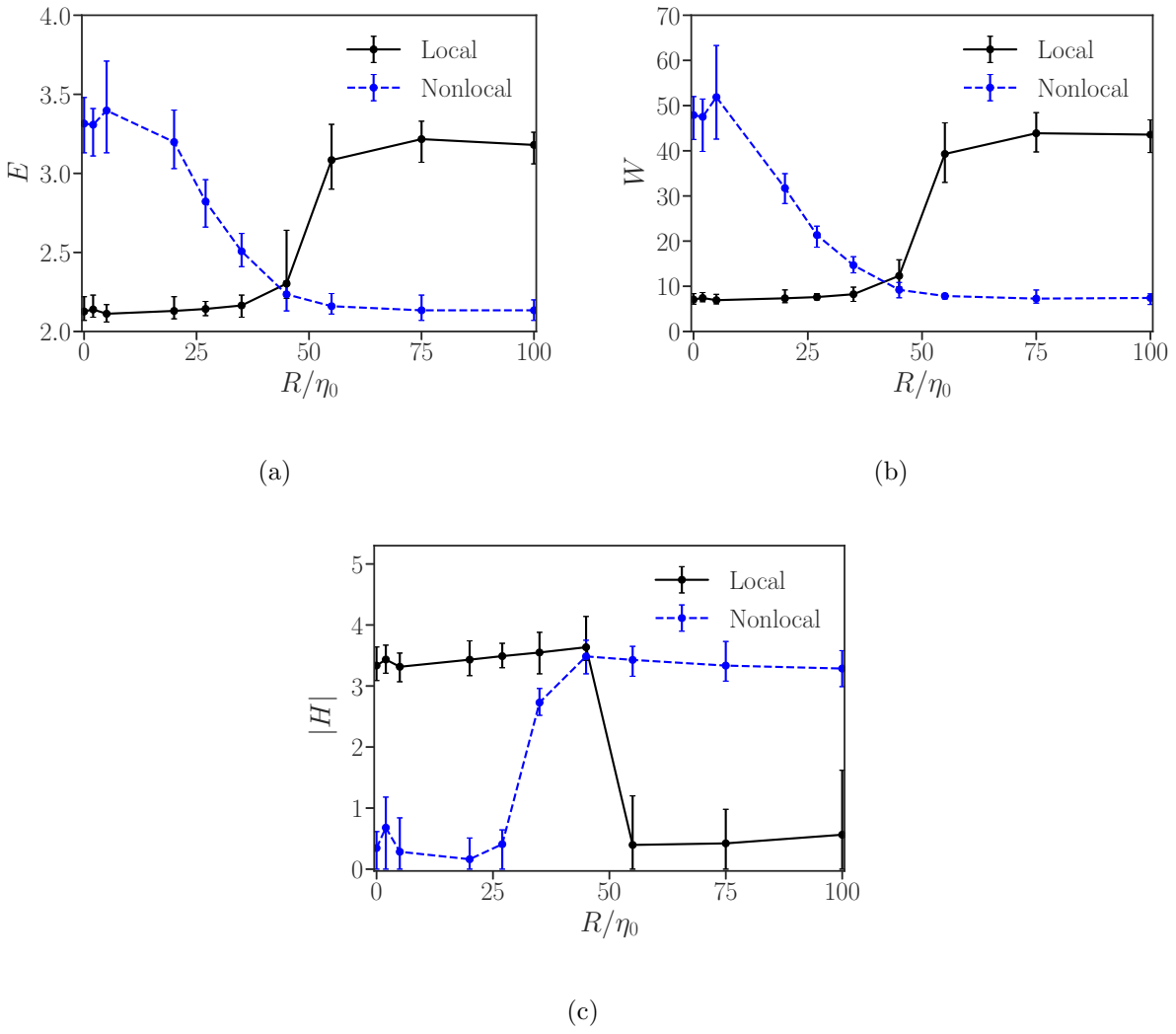

Figure 5.10: Influence of the radius of the local and nonlocal filters on integral quantities. (a) Energy. (b) Enstrophy. (c) Absolute value of helicity.

amplified by approximately an order of magnitude. We anticipate that this effect would be stronger at larger Reynolds numbers. The helicity, on the other hand, is much smaller in this limit, which is not because it ceases to be a conserved quantity. Indeed, helicity is conserved by both turbulence without and with vortex stretching. The actual reason is that the cascade direction of this quantity changes so that it has a tendency to accumulate at large scales. In classical 3D turbulence case, the forward helicity cascade allows a rapid drain of helicity towards the dissipation scale, a feature that stretching-less turbulence does not possess. Thereby turbulence without vortex-stretching has a stronger tendency to become helical, particularly in the absence of large-scale friction.

We can observe that integral quantities change rapidly around $R/\eta_0 = 50$ in the local filter cases. We can thus define a critical radius $R_c \approx 50\eta_0 = 2.11$. Strain outside the spherical region of radius R_c has little contribution to the vorticity associated with vortex-stretching. However, the critical radius is not so obvious in the non-local strain cases where the evolution of the quantities is more gradual. The critical radius seems to be associated with the change in cascade direction for the helicity and with the change in invariants for the enstrophy and energy. Such a change in cascade-direction was also observed in a pioneering study of non-integer dimensions [103] where the cross-over from two to three dimensional turbulence was investigated using two-point closure analysis.

5.5 Conclusion

We have in this chapter illustrated the cascades of enstrophy and helicity, as well as their associated spectral scalings in isotropic three-dimensional turbulence without vortex stretching. Confirming the predictions from statistical mechanics [92], we showed that enstrophy cascades from large scales towards small scales, where it is dissipated, while helicity is transferred from small scales towards large scales.

In the inertial range of the forward cascade, energy and helicity spectra follow $E(k) \propto k^{-3}$ and $|H(k)| \propto k^{-2}$ for $k \gg k_f$, associated with a conserved enstrophy flux towards large k. Closer to the forcing scale, logarithmic corrections allow us to describe the deviation of the spectral energy distribution from the dimensional prediction.

For the inverse cascade, we have $E(k) \propto k^{-7/3}$ and $|H(k)| \propto k^{-4/3}$ for wave numbers in the range between the friction wavenumber and the forcing wave number. It is shown that

these wave number ranges are associated with a constant (conserved) flux of helicity towards small k.

Our investigation of the influence of the filtering of the strain-rate tensor highlights how the properties of the flow change between the two limiting cases: normal turbulence and turbulence without vortex stretching. It is observed that, in particular, the steady-state value of the global helicity changes in a dramatic manner for a critical value of the filter width. This indicates that the change in cascade direction might be an important concept underlying critical transitions in turbulent flows. We can mention a recent investigation, which illustrates a similar phenomenon in the presence of strong rotation [109].

An interesting perspective of the present investigation would be the assessment of the chirality of the flow structures. Indeed, it is observed that in our simulations, the relation between helicity and energy spectra is nearly $|H(k)| = kE(k)$. Formulations of energy and helicity using the helical decomposition [40] allow us to show that $|H(k)| = kE(k)$ corresponds to homochiral modes. By imposing helicity forcing, where only positive or negative chiral modes are mainly input, in classical 3D turbulence, we can generate an inverse energy cascade characterized by an energy spectrum proportional to $k^{-5/3}$ [110]. Moreover, in flows where only a certain class of chiral modes is retained, a dual cascade is observed: a direct helicity cascade with an energy spectrum proportional to $k^{-7/3}$ and an inverse energy cascade with an energy spectrum proportional to $k^{-5/3}$ [111]. The interesting feature is that in that particular case, the helicity is transferred to small scales as opposed to the inverse helicity cascade in the present system.

Another feature of this system which deserves further research is the long-time evolution of the system in the absence of large-scale damping. Indeed, in the absence of friction or other forms of large-scale damping, helicity will pile up, as energy does for two-dimensional turbulence. Furthermore, since the system resembles two-dimensional turbulence in certain aspects, the characterization of flow structures using statistical mechanics [62, 63] is an interesting direction for investigation. This is what we will investigate in Chapter 6.

Chapter 6

Condensation and freely decaying states

As explained in Chapter 2, in 2D turbulence at high Reynolds numbers, nonlinear interactions yield a transfer of energy towards large scales. If energy is continuously injected, and in the absence of a large-scale dissipation mechanism, energy eventually accumulates in low wave numbers, leading to a condensate [41]. This condensation phenomenon has been observed numerically, and in 2D periodic square domains, the physical manifestation of this condensation is the generation of a large-scale counter-rotating vortex pair [112,113]. Such large-scale coherent structures are also observed in quasi-two-dimensional turbulence [114] and are at the heart of a number of geophysical processes [54, 115, 116]. The turbulence without vortex stretching is a system between 2D and 3D. Therefore, we are interested in investigating whether large-scale condensation will occur in turbulence without vortex stretching.

In Chapter 5, we demonstrated that the forced, no vortex-stretching turbulent system exhibits an inverse helicity cascade and a forward enstrophy cascade, with energy also cascading inversely, transported by helicity. To investigate the inertial ranges, we introduced large-scale friction in Chapter 5 to dissipate energy from the largest scales. A natural question arises: What happens when energy is not removed from large scales?

In this chapter, we will establish that condensation occurs at the scale of the box for our system if no large-scale friction is present. Subsequently, we will examine the system as it freely decays from this condensed state. We will attempt to predict the properties of large-scale structures in both forced-dissipative and freely decaying turbulence by employing

point-vortex statistical mechanics.

This chapter is structured as follows. In Section 6.1, we employ a generalized point-vortex model to predict a sinh relation in 3D turbulence without vortex-stretching. Subsequently, in Section 6.2, we present the numerical simulations and the evaluation of our theoretical results. Lastly, Section 6.3 presents the conclusions of this chapter.

6.1 Analytical considerations

In this section, we assess the dynamics of the condensation state, where we predict the existence of a hyperbolic sine relationship between velocity and vorticity. Furthermore, we introduce a definition for negative temperature associated with helicity.

6.1.1 Sinh relation

As introduced in Sec. 2.3.2, when 2D turbulence attains a condensation state, a sinh relation between vorticity and stream function emerges (Eq. (2.81)). We investigate whether there is a similar functional relation in our turbulent system without vortex stretching. We generalize the point-vortex model to a 3D system. Thereto we propose that a 3D vorticity field can be considered as a combination of $6M$ point vortices, the axes of which are each parallel to one of the three coordinate axes. We suppose that in each direction there are M point-vortices of positive vorticity $+1$, and M ones of negative vorticity -1. Without loss of generality, we use non-dimensional vorticities $+1$ and -1 here. Similar to Ref. [64], we imagine the total volume $V = L^3$ subdivided into small cells of volume $\Delta \ll V$. The cells are large enough, however, to contain many particles. We call $M^+_{i,x}$, $M^+_{i,y}$, $M^+_{i,z}$ and $M^-_{i,x}$, $M^-_{i,y}$, $M^-_{i,z}$ the number of positive and negative point-vortices in each direction inside cell i. Then the vorticity field can be written as

$$\begin{cases} \omega_x(\boldsymbol{r}) = \sum_i (M^+_{i,x} - M^-_{i,x}) \delta\left(\boldsymbol{r} - \boldsymbol{r}_i\right), \\ \omega_y(\boldsymbol{r}) = \sum_i (M^+_{i,y} - M^-_{i,y}) \delta\left(\boldsymbol{r} - \boldsymbol{r}_i\right), \\ \omega_z(\boldsymbol{r}) = \sum_i (M^+_{i,z} - M^-_{i,z}) \delta\left(\boldsymbol{r} - \boldsymbol{r}_i\right), \end{cases} \tag{6.1}$$

where $\boldsymbol{r}_i$ indicates the position of cell i. The associated velocity field can be obtained using Biot-Savart's law

$$\boldsymbol{u}(\boldsymbol{x}) = \frac{1}{4\pi} \int_{\mathbb{R}^3} \frac{\boldsymbol{\omega}(\boldsymbol{y}) \times (\boldsymbol{x} - \boldsymbol{y})}{|\boldsymbol{x} - \boldsymbol{y}|^3} d\boldsymbol{y}. \tag{6.2}$$

Substituting Eq. (6.1) into Eq. (6.2), yields expressions for the velocity components in each direction

$$\begin{cases} u_x(\boldsymbol{r}) = \frac{1}{4\pi}\sum_i \frac{(M^+_{i,y}-M^-_{i,y})(r_z-r_{i,z})-(M^+_{i,z}-M^-_{i,z})(r_y-r_{i,y})}{|\boldsymbol{r}-\boldsymbol{r}_i|^3}, \\ u_y(\boldsymbol{r}) = \frac{1}{4\pi}\sum_i \frac{(M^+_{i,z}-M^-_{i,z})(r_x-r_{i,x})-(M^+_{i,x}-M^-_{i,x})(r_z-r_{i,z})}{|\boldsymbol{r}-\boldsymbol{r}_i|^3}, \\ u_z(\boldsymbol{r}) = \frac{1}{4\pi}\sum_i \frac{(M^+_{i,x}-M^-_{i,x})(r_y-r_{i,y})-(M^+_{i,y}-M^-_{i,y})(r_x-r_{i,x})}{|\boldsymbol{r}-\boldsymbol{r}_i|^3} \end{cases} \tag{6.3}$$

with $r_{i,x}, r_{i,y}, r_{i,z}$ the x-, y- and z-component of $\boldsymbol{r}_i$, and z-component of $\boldsymbol{r}_i$ and r_x, r_y, r_z the x-, y-, and z-component of $\boldsymbol{r}$.

This point-vortex model allows us to define an entropy using Boltzmann's formula. The entropy of this 3D point-vortex system can be written as

$$S = \ln \mathscr{W} \tag{6.4}$$

with

$$\mathscr{W} = \frac{(6M)!}{\prod_i \left\{M^+_{i,x}!M^-_{i,x}!M^+_{i,y}!M^-_{i,y}!M^+_{i,z}!M^-_{i,z}!\right\}}. \tag{6.5}$$

The quantity $\mathscr{W}$ indicates the number of microstates associated with the macrostate where there are $M^+_{i,x}$, $M^+_{i,y}$, $M^+_{i,z}$ positive and $M^-_{i,x}$, $M^-_{i,y}$, $M^-_{i,z}$ negative point-vortices inside cell i. We assume $M^+_{i,x}$, $M^+_{i,y}$, $M^+_{i,z}$, $M^-_{i,x}$, $M^-_{i,y}$, $M^-_{i,z}$ to be large enough for Stirling's formula to be valid. We then obtain

$$\begin{aligned} S \approx 6M\ln(6M) - 6M + \textstyle\sum_i (&-M^+_{i,x}\ln M^+_{i,x} + M^+_{i,x} - M^-_{i,x}\ln M^-_{i,x} + M^-_{i,x} - M^+_{i,y}\ln M^+_{i,y} + M^+_{i,y} \\ &-M^-_{i,y}\ln M^-_{i,y} + M^-_{i,y} - M^+_{i,z}\ln M^+_{i,z} + M^+_{i,z} - M^-_{i,z}\ln M^-_{i,z} + M^-_{i,z}) \end{aligned} \tag{6.6}$$

Similar to a 2D system, we assume the final state of 3D turbulence without vortex stretching to be close to the maximum entropy state. We will therefore attempt to determine this state by maximizing the entropy under the constraints imposed by the dynamical equation. Indeed, enstrophy and helicity are inviscid invariants in 3D turbulence without vortex stretching. To proceed, we need therefore to consider formulas of these two invariants expressed as a function of the variables governing the 3D point-vortex system. The total helicity of the system is given by

$$\begin{aligned} H = \tfrac{1}{2}\textstyle\int \boldsymbol{u}\cdot\boldsymbol{\omega} d\boldsymbol{r} = \frac{1}{8\pi}\sum_{i,j}\frac{1}{|\boldsymbol{r}_j-\boldsymbol{r}_i|^3} \\ \big((M^+_{j,x}-M^-_{j,x})\left((M^+_{i,y}-M^-_{i,y})(r_{j,z}-r_{i,z}) - (M^+_{i,z}-M^-_{i,z})(r_{j,y}-r_{i,y})\right) + \\ (M^+_{j,y}-M^-_{j,y})\left((M^+_{i,z}-M^-_{i,z})(r_{j,x}-r_{i,x}) - (M^+_{i,x}-M^-_{i,x})(r_{j,z}-r_{i,z})\right) + \\ (M^+_{j,z}-M^-_{j,z})\left((M^+_{i,x}-M^-_{i,x})(r_{j,y}-r_{i,y}) - (M^+_{i,y}-M^-_{i,y})(r_{j,x}-r_{i,x})\right)\big). \end{aligned} \tag{6.7}$$

And enstrophy of this 3D point-vortex system can be written as

$$W = \sum_i (1)^2 M_{i,x}^+ + \sum_i (-1)^2 M_{i,x}^- + \sum_i (1)^2 M_{i,y}^+ + \sum_i (-1)^2 M_{i,y}^- + \sum_i (1)^2 M_{i,z}^+ + \sum_i (-1)^2 M_{i,z}^-. \tag{6.8}$$

The maximum entropy state is now obtained by solving the variational problem,

$$\delta S - \beta \delta H - \alpha \delta W = 0 \tag{6.9}$$

with β, α Lagrange multipliers. Similar to what was assumed for 2D systems, we suppose the numbers of positive or negative point-vortices to be independent of each other. Thus, the partial derivative of helicity with respect to $M_{j,x}^+$ is

$$\frac{\partial H}{\partial M_{j,x}^+} = \frac{1}{8\pi} \sum_i \frac{(M_{i,y}^+ - M_{i,y}^-)(r_{j,z} - r_{i,z}) - (M_{i,z}^+ - M_{i,z}^-)(r_{j,y} - r_{i,y})}{|\boldsymbol{r}_j - \boldsymbol{r}_i|^3} = \frac{u_x(\boldsymbol{r}_j)}{2}. \tag{6.10}$$

Other derivatives have similar forms. Then, substituting Eq. (6.6), (6.7) and (6.8) into Eq. (6.9) and deriving the integrand with respect to $M_{i,x}^+$ and $M_{i,x}^-$ yields the expressions

$$\begin{cases} \ln M_{i,x}^+ + \alpha + \frac{\beta}{2} u_x(\boldsymbol{r}_i) = 0, \\ \ln M_{i,x}^- + \alpha - \frac{\beta}{2} u_x(\boldsymbol{r}_i) = 0. \end{cases} \tag{6.11}$$

Results in the other two directions are similar. Hence, the numbers of point-vortices in the cell i with vorticity vectors along the x-direction are

$$\begin{aligned} M_{i,x}^+ &= \exp(-(\alpha + \frac{\beta}{2} u_x(\boldsymbol{r}_i))), \\ M_{i,x}^- &= \exp(-(\alpha - \frac{\beta}{2} u_x(\boldsymbol{r}_i))), \end{aligned} \tag{6.12}$$

at the maximum entropy state. Using Eq. (6.1), we find

$$\begin{aligned} \omega_x =& \exp(-\alpha)(\exp(-\frac{\beta}{2} u_x) - \exp(\frac{\beta}{2} u_x)) \\ =& 2\exp(-\alpha)\sinh(-(\frac{\beta}{2} u_x)). \end{aligned} \tag{6.13}$$

After applying similar derivations in the other two directions, the vorticity components in the y- and z-directions are

$$\begin{aligned} \omega_y &= 2\exp(-\alpha)\sinh(-(\tfrac{\beta}{2} u_y)), \\ \omega_z &= 2\exp(-\alpha)\sinh(-(\tfrac{\beta}{2} u_z)). \end{aligned} \tag{6.14}$$

This sinh relation between vorticity and velocity, Eqs. (6.13) and (6.14) is the principal theoretical result of the present investigation.

6.1.2 Negative temperature

As mentioned in Sec.2.3, in 2D turbulence, a negative temperature suggests the possibility of an inverse energy cascade. Moreover, in 3D turbulence without vortex stretching, we observe an inverse cascade of helicity (refer to Chapter 5). This prompts us to explore if an analogous negative temperature concept can be associated with helicity in 3D turbulence without vortex stretching.

Unlike energy which is always positive, helicity can be either positive or negative. This property of helicity indicates that we cannot define negative temperature only based on the negative sign of the variable β. Consequently, we need to develop a novel and suitable definition of negative temperature associated with helicity. In 2D turbulence, the intrinsic interpretation of negative temperature is that entropy decreases as energy increases, signifying that the system grows more organized when energy is input. In 3D turbulence without vortex stretching, β should be negative for positive helicity and positive for negative helicity, ensuring that entropy decreases as the absolute value of helicity increases. Such an understanding paves the way for a suitable definition of negative temperature in our system: helicity and β have opposite signs.

Using the point-vortex model in the condensation state, we can derive a sinh relation between velocity and vorticity (refer to Eq. (6.13) and (6.14)). An exact formula for β seems difficult to derive from the equation for β. However, a plausible approximation can be made for the low-energy case, i.e., when $|\frac{\beta}{2}u_i|^2 \ll 1$. In this case, we have $\omega_i \approx -\exp(-\alpha)\beta u_i$. Hence $u_i\omega_i = -\exp(-\alpha)\beta u_i u_i$, and thus we obtain $\beta = -\frac{H}{\exp(-\alpha)E}$. Given that $\exp(-\alpha)$ and E are always positive, this formulation of β implies that β and H have opposite signs, suggesting a negative temperature associated with helicity.

6.2 Numerical simulations

We first show the energy condensation process in a forced system in Sec. 6.2.2. Subsequently, in Sec. 6.2.3, we eliminate the force and allow the system to decay freely from the condensation state. In both cases, we verify our predictions from the point-vortex model by illustrating the emergence of a hyperbolic sine relation between velocity and vorticity.

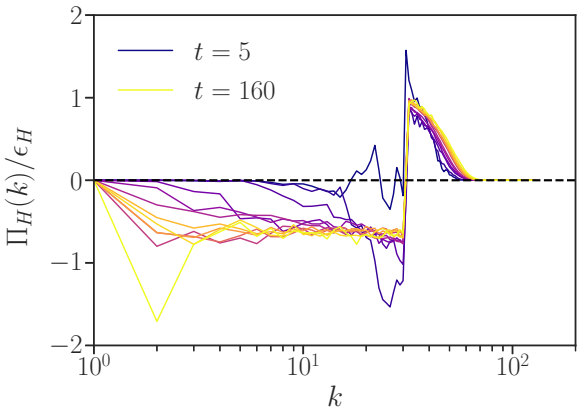

Figure 6.1: Flux of helicity normalized by the dissipation rate of helicity during the force-dissipative phase at $t = 5$, 10, 20, 30, 40, 50, 60, 70, 80, 100, 130, 160. The coloring of the curves evolves in time from dark to light.

6.2.1 Setup

In order to validate the analytical predictions presented in Sec. 6.1, we conduct Direct numerical simulations. Our computational domain consists of a periodic box in three dimensions with a length of side $L = 2\pi$ and a grid of size 256^3.

We consider two cases. For the first one, we integrate Eq. (3.9). For the second one, we eliminate the force and allow the system to decay freely. Since we are concentrating on the condensation state without focusing too much on the dissipation range, we reduce the size of the latter by using hyperviscosity $\hat{\boldsymbol{d}} = \nu k^{2b} \hat{\boldsymbol{u}}$ and we use therefore the value $b = 4$. The parameter ν represents the hyperviscosity rate which is set to 10^{-13} in our simulations. We choose an injection mechanism that keeps the energy constant in a narrow wavenumber range $29.5 \leq k < 31.5$ around the forcing wavenumber $k_f = 30.5$ at a level $E(k) = 10^{-3}$.

The initial energy spectrum is chosen as $E(k) = 5 \times 10^{-7}$. The initial value of the energy is small enough to allow a clear observation of the energy condensation process. Complex phases of $\hat{\boldsymbol{u}}$ are set randomly at the initial moment.

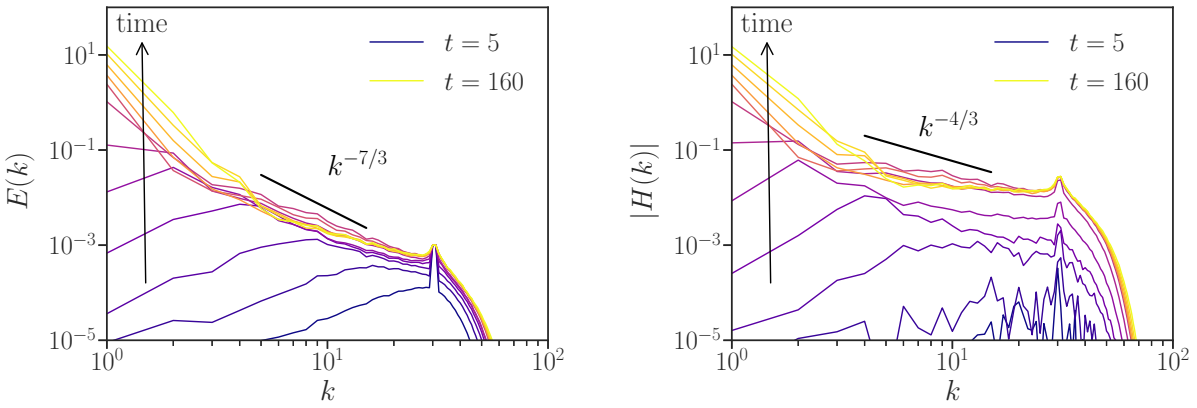

(a) (b)

Figure 6.2: Time evolution of wavenumber spectra of the kinetic energy (a) and helicity (b) during the force-dissipative phase. The time-instants are the same as indicated in Fig. 6.1.

6.2.2 Forced turbulence

We start by forcing the system from a random initial condition, dissipating mainly the small scales. In Fig. 6.1, we show the time evolution of the helicity flux normalized by its dissipation rate ϵ_H, defined as $\epsilon_H = \int 2\nu k^{2b} H(k) dk$, during the condensate phase from $t = 5$ to $t = 160$. In turbulence governed by Eq. (3.9), the flux of helicity is defined as $\Pi_H(k) = -\int_{\Sigma_k} \mathrm{Re}\left[\hat{\boldsymbol{N}}(\boldsymbol{k}) \cdot \hat{\boldsymbol{u}}^*(\boldsymbol{k})\right] d\boldsymbol{k}$ with $\hat{\boldsymbol{N}}(\boldsymbol{k}) = \mathcal{F}[-(\boldsymbol{u} \cdot \nabla)\boldsymbol{\omega}]$ the non-linear term in the vorticity equation. Σ_k is the spherical domain in Fourier space consisting of all wave vectors with $\|\boldsymbol{k}\| \leqslant k$. The normalized flux is negative at scales smaller than the forcing wavenumber $k_f = 30.5$, implying the helicity cascades from small towards large scales during this phase.

In Fig. 6.2 (a) and (b), we show the time evolution of energy and helicity spectra, respectively. A peak in the energy and helicity spectra appears at large scales after $t = 60$. Indeed, since helicity is conserved by the nonlinearity and there is only very weak damping present at scales $k < k_f$, the physical process leading to the build-up at the large scales of the system is associated with the helicity which is transferred to large scales. After arriving at the largest scales of the system, no dissipation mechanism is able to absorb the helicity injected by the forcing. The helicity and its associated energy piles then up, leading to large spectral peaks at the small wavenumbers. The spectra of kinetic energy and

helicity for intermediate wavenumbers during the inverse cascade of helicity are theoretically proportional to $k^{-7/3}$ and $k^{-4/3}$, respectively, which are the expected scalings in the inverse cascade range of turbulence without vortex stretching, as shown in Chapter 5. However, due to the limitation of computing resources, the inertial range is not sufficiently large to clearly display these theoretical scalings.

In Fig. 6.3, we show the time evolution of kinetic energy, helicity, and enstrophy in the three directions, respectively. After $t \approx 60$, kinetic energy, helicity, and enstrophy in the y direction become larger than in the other two directions. At this time the condensation process starts. The associated condensate-like structure is visualized in Fig. 6.4. This structure is constituted of highly anisotropic columnar structures in the y direction. A parallel can here be drawn with 2D turbulence where the condensate-like structure is a pair of counter-rotating vortices.

After reaching this condensate state, we assess the relation between velocities and vorticities as predicted by the point-vortex model in Sec. 6.1. Fig. 6.5 shows the scatter plot of u_y against ω_y for the condensation state at $t = 160$. A tendency of a sinh-relation can be found, but a considerable noise hinders us from identifying a clear functional relationship. In order to reduce the noise, instead of investigating the relation between velocity and vorticity components directly, we focus on their averaged values

$$\begin{aligned} \langle u_y \rangle_y (x,z) &= \frac{1}{M_y} \sum_y u_y(x,y,z), \\ \langle \omega_y \rangle_y (x,z) &= \frac{1}{M_y} \sum_y \omega_y(x,y,z), \end{aligned} \tag{6.15}$$

where u_y and ω_y indicate velocity and vorticity in the y-direction, $\langle \cdot \rangle_y$ indicates a space average in the y-direction and M_y is the number of grid points in the y-direction ($M_y = 256$ in our simulations). Similar definitions can be defined in the other directions. As sinh is not a linear function, theoretically, we can not derive $\langle \omega_y \rangle_y = 2\exp(-\alpha)\sinh(-\frac{\beta}{2}\langle u_y \rangle_y)$ from Eq. (6.13) and (6.14). But if u_y is nearly constant along the y-direction, we can get an approximation $\left\langle \sinh(-\frac{\beta}{2}u_y) \right\rangle_y \approx \sinh(-\frac{\beta}{2}\langle u_y \rangle_y)$. An instantaneous visualization of three velocity components for the condensation state at $t = 160$ is shown in Fig. 6.6. We observe that u_x, u_y and u_z depend only weakly on the x, y and z directions respectively. Thus, the averaged values are appropriate for investigating the hyperbolic sine relation. Furthermore, the structure of u_y is similar to a dipole, while structures of u_x and u_z are

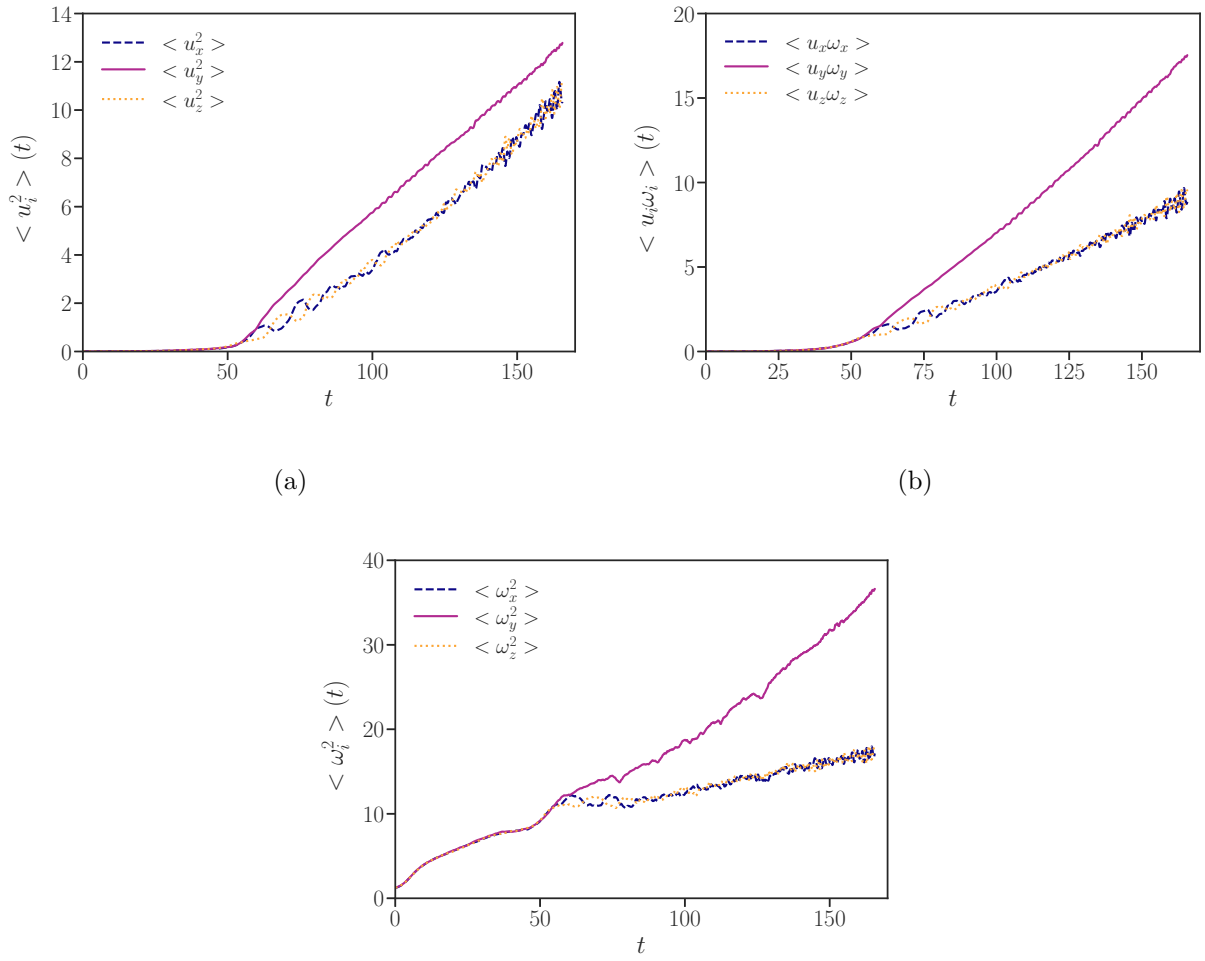

Figure 6.3: Time evolution of integral quantities contained in three directions during the force-dissipative phase. $\langle \bullet \rangle$ indicates the volume average. (a) Energy. (b) Helicity. (c) Enstrophy.

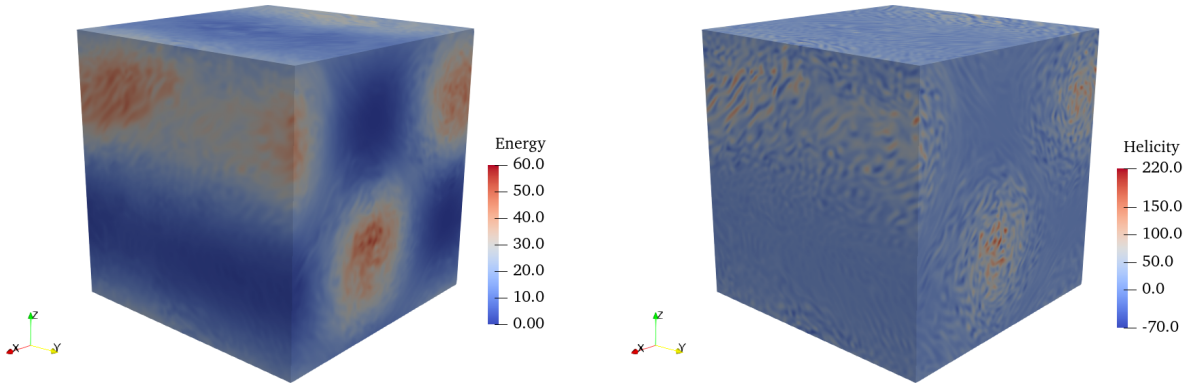

(a) (b)

Figure 6.4: Visualizations of condensate-like structure at $t = 160$. (a) Energy. (b) Helicity.

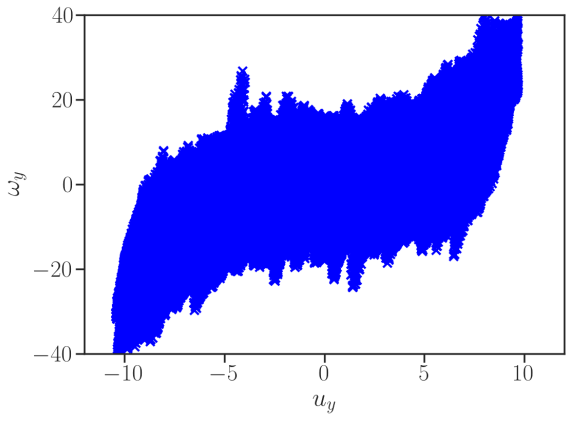

Figure 6.5: Scatter plot of y-components velocities and vorticities at the condensation state at $t = 160$.

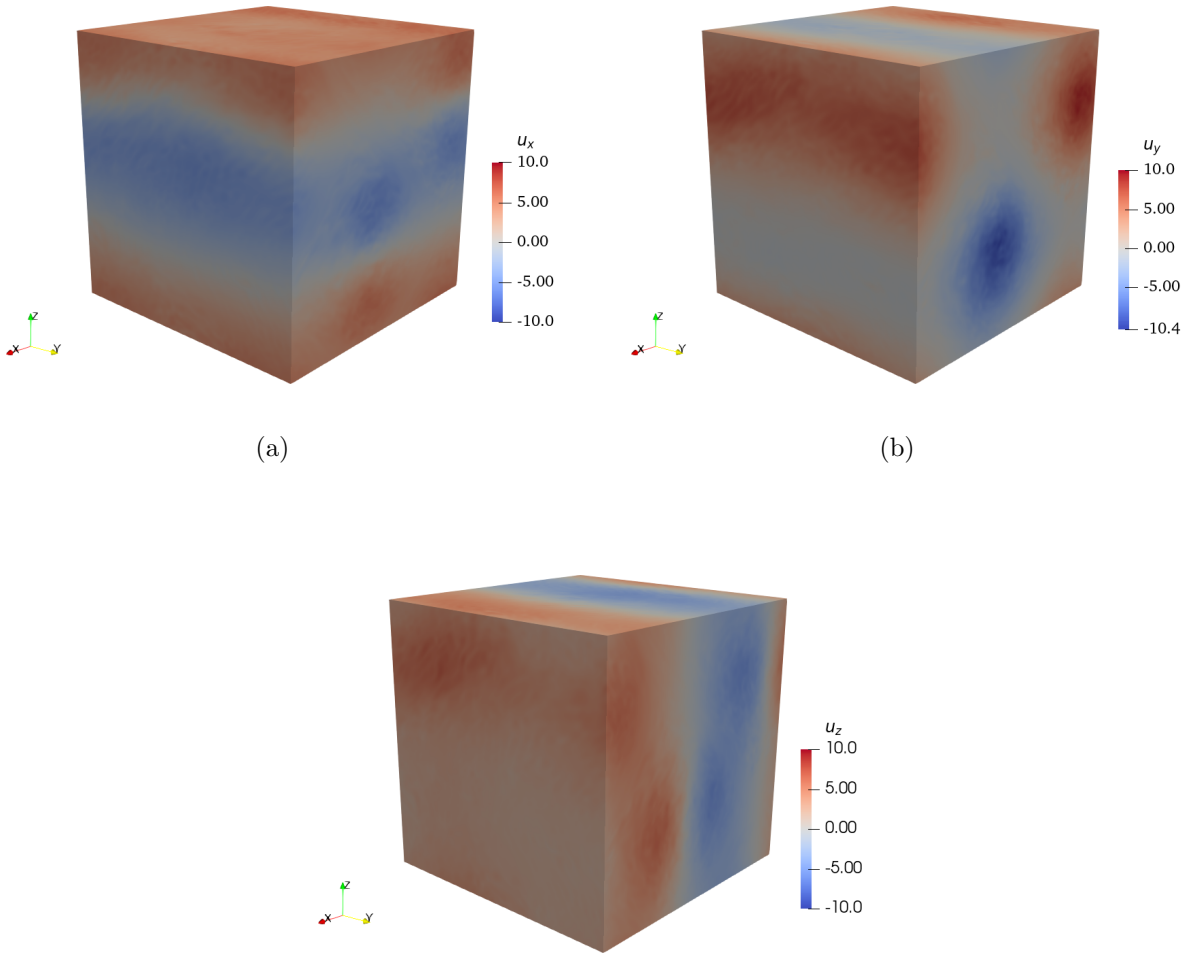

Figure 6.6: Velocity components in three directions at the condensation state at $t = 160$. (a) u_x. (b) u_y. (c) u_z.

closer to a unidirectional flow in 2D turbulence. Note that dipoles and unidirectional flows are two condensation states of 2D turbulence caused by bifurcations of stochastic Navier-Stokes equation [116].

The values of the two Lagrange multipliers α and β can be determined *a priori*. Firstly, we introduce the averaged quantities associated with helicity and enstrophy, as

$$\begin{aligned} H_{ave} =& \frac{1}{2}\sum_{y,z}\langle u_x\rangle_x(y,z)\langle w_x\rangle_x(y,z)+\frac{1}{2}\sum_{x,z}\langle u_y\rangle_y(x,z)\langle w_y\rangle_y(x,z)+ \\ & \frac{1}{2}\sum_{x,y}\langle u_z\rangle_z(x,y)\langle w_z\rangle_z(x,y), \\ W_{ave} =& \frac{1}{2}\sum_{y,z}\langle w_x\rangle_x^2(y,z)+\frac{1}{2}\sum_{x,z}\langle w_y\rangle_y^2(x,z)+\frac{1}{2}\sum_{x,y}\langle w_z\rangle_z^2(x,y), \end{aligned} \tag{6.16}$$

respectively. We substitute the relation $\langle\omega_m\rangle_m = 2\exp(-\alpha)\sinh(-(\frac{\beta}{2}\langle u_m\rangle_m))$ into Eq. (6.16) where m indicates x, y and z, so that H_{ave} and W_{ave} can be written as functions of averaged velocities $\langle u_m\rangle_m$. At each moment, exact values of $\langle u_m\rangle_m$, H_{ave}, and W_{ave} can be obtained from the simulation data. Then the two unknowns α and β can be calculated from these two equations of H_{ave} and W_{ave}. At $t = 160$, the analytically predicted curve is $\langle\omega_m\rangle_m = 1.5207\sinh(0.3779\langle u_m\rangle_m)$ in our simulation. In this case, β has a value of -0.7558, which is negative, while helicity is positive. The opposite signs of β and helicity indicate the presence of a negative temperature within this condensation state.

In Fig. 6.7, we show scatter plots of averaged components of velocities and vorticities in three directions for the condensation state at $t = 160$. A hyperbolic sine relation is observed between y-components $\langle u_y\rangle_y$ and $\langle\omega_y\rangle_y$. The yellow lines in Fig. 6.7 indicate the analytically predicted curve, which overlaps the data points in the direction where most energy is contained. This collapse verifies our analytical prediction of the sinh relation in the y-direction. However, for other directions, we observe a linear instead of a sinh relation between velocities and vorticities, as shown in Fig. 6.7(a) and (c). It can be easily demonstrated that $\lim_{x\to 0}\sinh(cx) = cx$ with c a constant number, which indicates that the form of $\sinh(cx)$ resembles a straight line when x varies in a small range around 0. We insist that these functional relations are not direct fits of the sinh relation to the data but obtained evaluating the averaged quantities $\langle u_m\rangle_m$, H_{ave} and W_{ave} only.

Moreover, we note that y direction is not necessarily the direction which contains most energy. Further details can be found in Sec. 6.2.4.

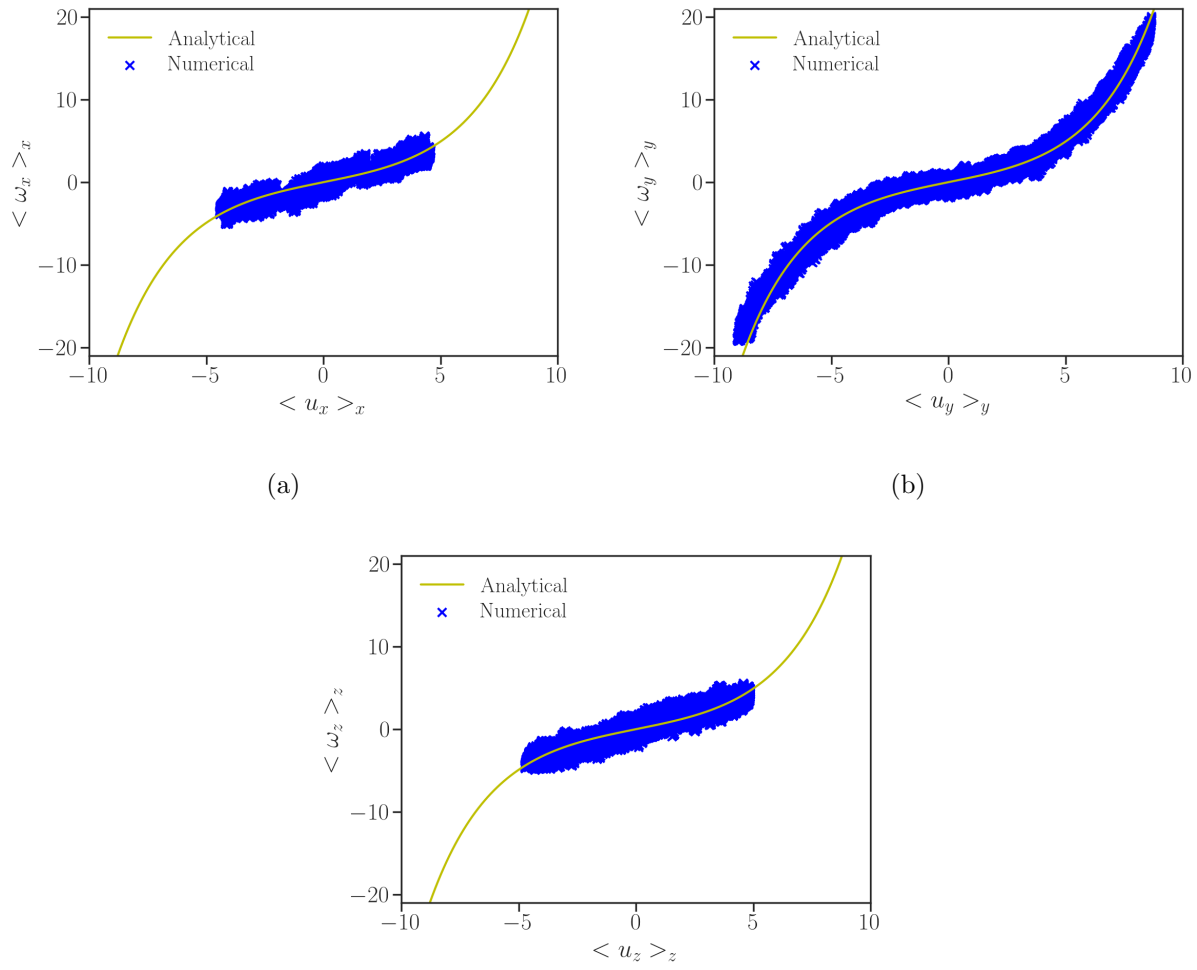

Figure 6.7: Scatter plots of averaged components of velocities and vorticities in three directions at the condensation state at $t = 160$. The yellow lines present the analytically predicted curve $\langle \omega_m \rangle_m = 1.5207 \sinh(0.3779 \langle u_m \rangle_m)$. (a) X-components. (b) Y-components. (c) Z-components.

6.2.3 Freely decaying turbulence

At the condensation state at $t = 160$, the external force is removed from the system, and we indicate in this section the moment when the removal of force commences as time $t = 0$.

In Fig. 6.8, we show the time evolution of kinetic energy, helicity, and enstrophy in the three directions, respectively. During the free-decay phase, most of kinetic energy, helicity, and enstrophy remain concentrated in the y direction. As shown in Fig. 6.8(a), energy displays an increasing trend during the dissipation phase, especially in the y direction, which is not violating any conservation laws because energy is not conserved in turbulence without vortex stretching (see Chapter 4). From Fig. 6.8(b), we can see that the value of helicity exhibits very little change over time since most of the helicity cascades towards small wavenumbers and is hardly dissipated by the hyperviscosity. Fig. 6.8(c) shows the decrease of enstrophy.

In Fig. 6.9(a) and (b), we show the time evolution of energy and helicity spectra, respectively. We observe that the energy and helicity at small scales decay during the dissipation. The insets in Fig. 6.9 provide a detailed view around the first modes, revealing that energy and helicity at large scales increase for a duration $t \leq 16$ after the external force is removed. The large-scale structures persist for a period after eliminating the force, as shown in Fig. 6.10.

In Fig. 6.11(a), we show scatter plots of y-components of velocities and vorticities, along with the analytically predicted black curves. Here, no-averaged values u_p, H, and W are used to calculate Lagrange multipliers α and β at each moment. In this case, β and helicity have opposite signs, suggesting a negative temperature. During the dissipation phase, noise at small scales decreases, and we observe a clear hyperbolic sine relation between u_y and ω_y. Our analytical prediction of the sinh relation in the y direction is confirmed by the overlapping of the predicted curve and data points. For other directions, similar to the forced phase, we observe a linear instead of a sinh relation between velocities and vorticities, as shown in Fig. 6.11(b).

6.2.4 Supplemental simulations

To assess the robustness of the results presented above, we also executed eight supplemental DNS-runs using the same initial energy spectrum but different initial complex phases of $\hat{\boldsymbol{u}}$.

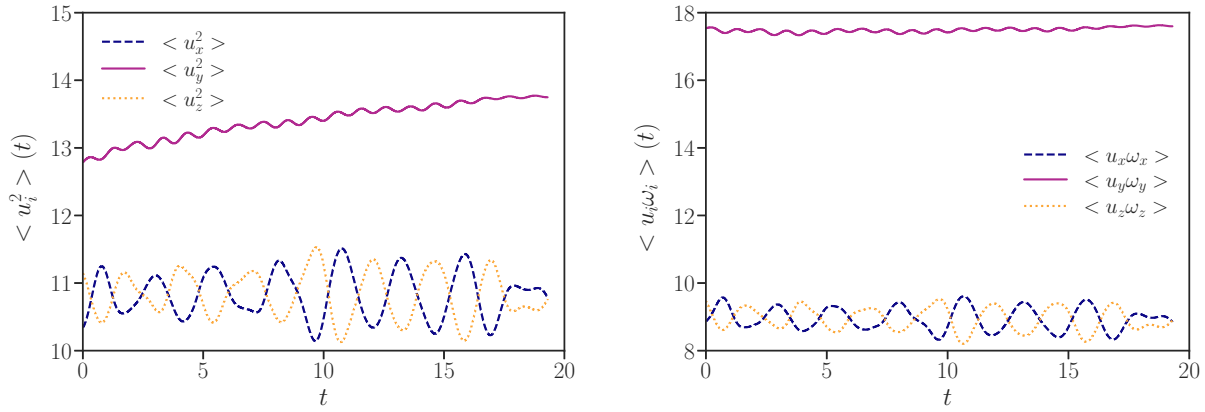

Figure 6.8: Time evolution of integral quantities contained in three directions during the freely decaying phase. (a) Energy. (b) Helicity. (c) Enstrophy.

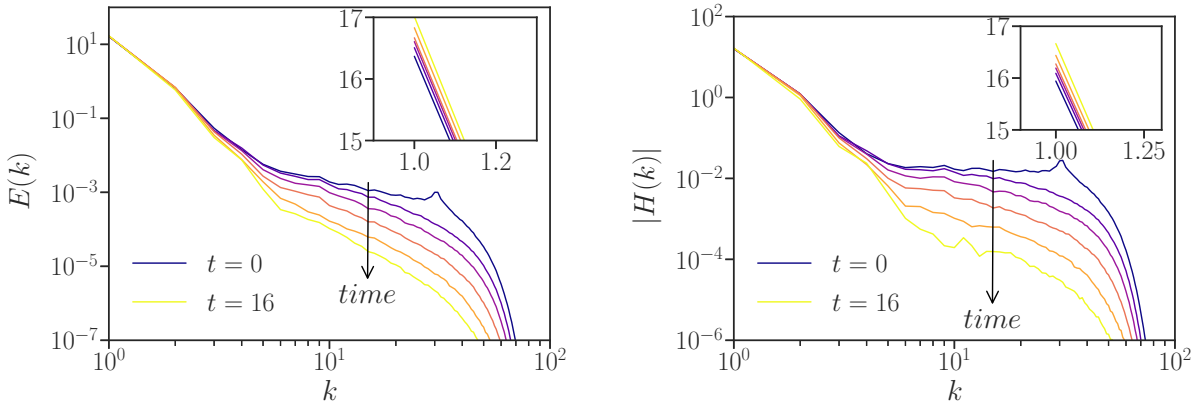

(a) (b)

Figure 6.9: Time evolution of wavenumber spectra of kinetic energy (a) and helicity (b) during the freely decaying phase at $t = 0$, 1, 2, 4, 8, 16. The insets in (a) and (b) provide a detailed view around the first modes.

We find that the y direction is not necessarily the direction which contains most energy. Indeed there is no reason that the y-direction should be different. Furthermore, in one of the eight simulations, energy in two of the three directions is comparable and larger than that in the third direction. In this cases the sinh relation is found in the two directions containing larger energy, presented in Fig. 6.12(b-d).

Fig. 6.13 shows the visualization of energy and iso-enstrophy surface at a condensation state ($t = 126$). The spatial structure is a 3D structure that looks like two columns along the x direction and two along the z direction.

In all our nine simulations we have thus observed this type of symmetry breaking where two components of the kinetic energy take the same value, the other being either larger or smaller. No observations are reported where all three components tend to the same value. We have no rigorous explanation for this symmetry breaking.

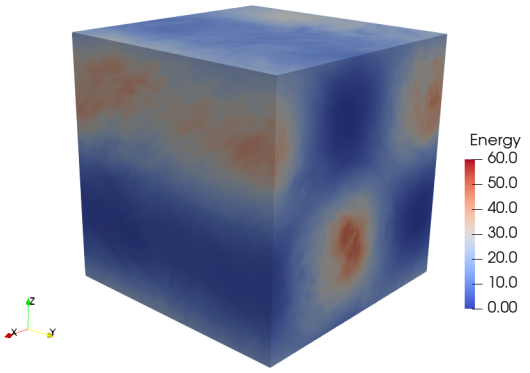

(a)

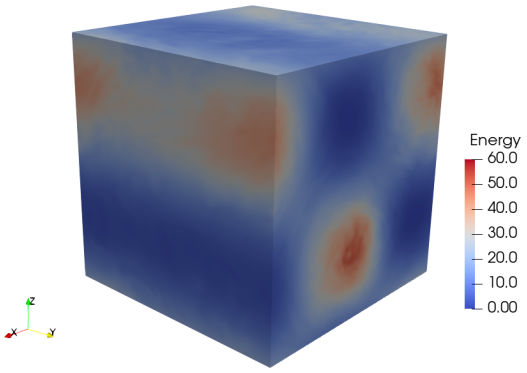

(b)

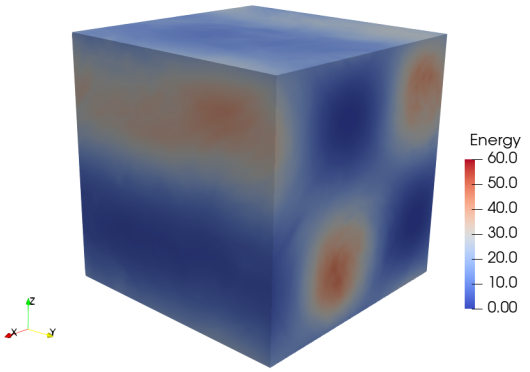

(c)

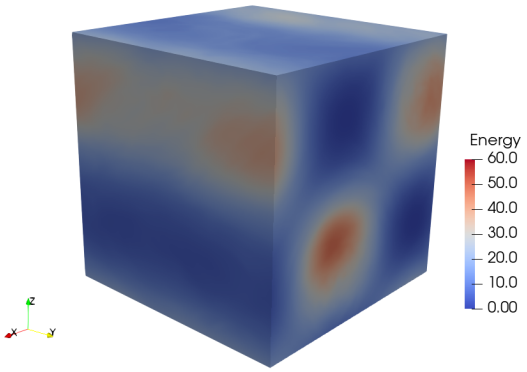

(d)

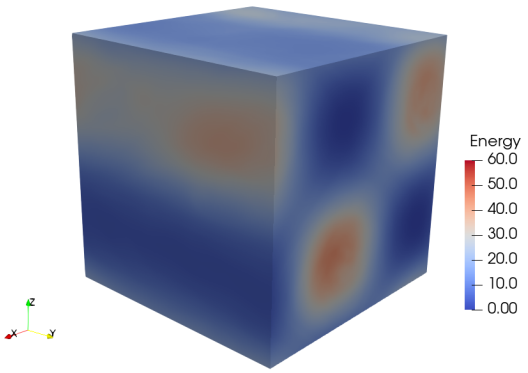

(e)

Figure 6.10: Visualization of energy during the freely decaying phase. (a) $t = 1$. (b) $t = 2$. (c) $t = 4$. (d) $t = 8$ (e) $t = 16$.

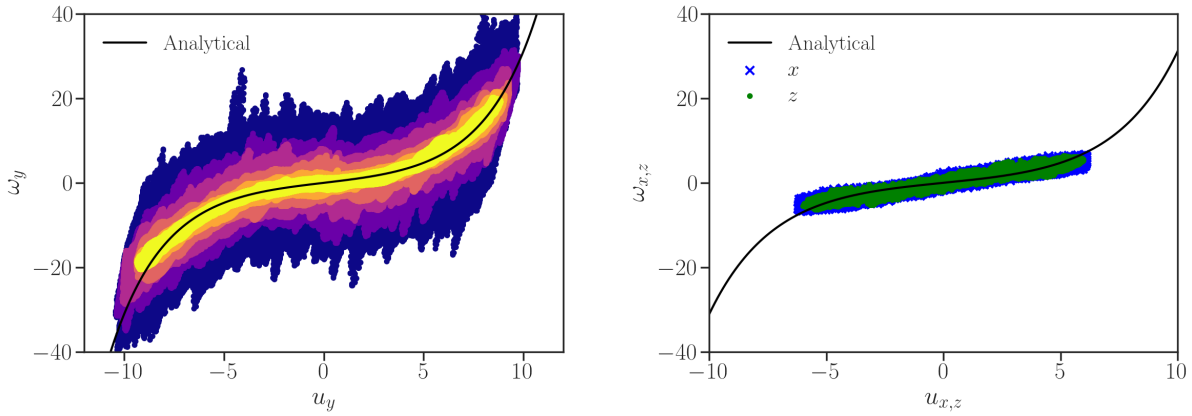

(a) (b)

Figure 6.11: Scatter plots of the components of velocities and vorticities during the freely decaying phase. (a) u_y versus ω_y at time instants $t = 0, 1, 2, 4, 8, 16$ from dark to light. (b) x- and z-components of velocities and vorticities at $t = 16$. Black lines in (a) and (b) are the analytically predicted curves at $t = 16$, given by $\omega_y = 1.511 \sinh(0.3718 u_y)$.

6.3 Conclusion

In this chapter, we have illustrated a large-scale condensation of energy in 3D turbulence without vortex stretching. As we presented in Chapter 5, helicity cascades from small to large scales. During the cascade, energy is carried by helicity towards the smallest wave numbers. In the absence of friction at large scales, energy accumulates and forms a large-scale structure. And this large-scale structure persists for a period after eliminating the force.

This condensate of 3D turbulence without vortex stretching behaves like that of 2D turbulence. We showed analytically a generalized 3D point-vortex model to predict a hyperbolic sine relation between vorticity and velocity in the direction which contains most energy. In a forced system, after condensation occurs, the predicted hyperbolic sine relation can be found between averaged vorticity and velocity, which suggests that the statistical mechanics approach can be applied to averaged systems, as also observed in experiments [80]. During the freely decaying phase, the relation between vorticity and velocity very clearly relaxes to the predicted hyperbolic sine function, similar to the sinh relation between vorticity and stream

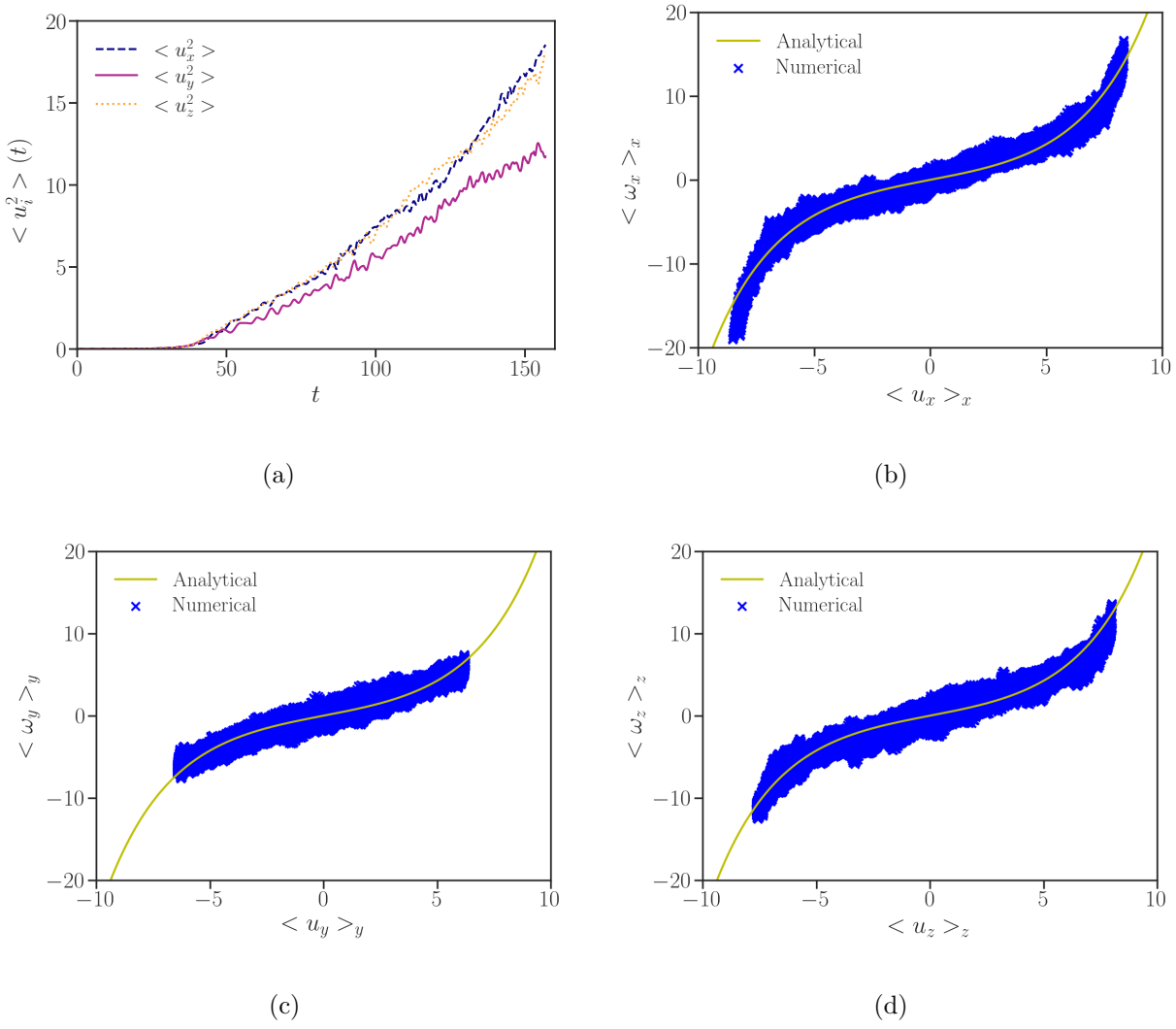

Figure 6.12: Simulation results of the case where energy in two of the three directions is larger than that in the third direction. (a) Mean square values of velocity components in three directions. (b-d) Scatter plots of averaged components of velocities and vorticities in three directions at $t = 126$. (b) Relation between $\langle u_x \rangle_x$ and $\langle \omega_x \rangle_x$. (c) Relation between $\langle u_y \rangle_y$ and $\langle \omega_y \rangle_y$. (d) Relation between $\langle u_z \rangle_z$ and $\langle \omega_z \rangle_z$. Yellow lines in (b), (c) and (d) are the analytically predicted curves $\langle \omega_m \rangle_m = 1.5391 \sinh(0.3479 \langle u_m \rangle_m)$.

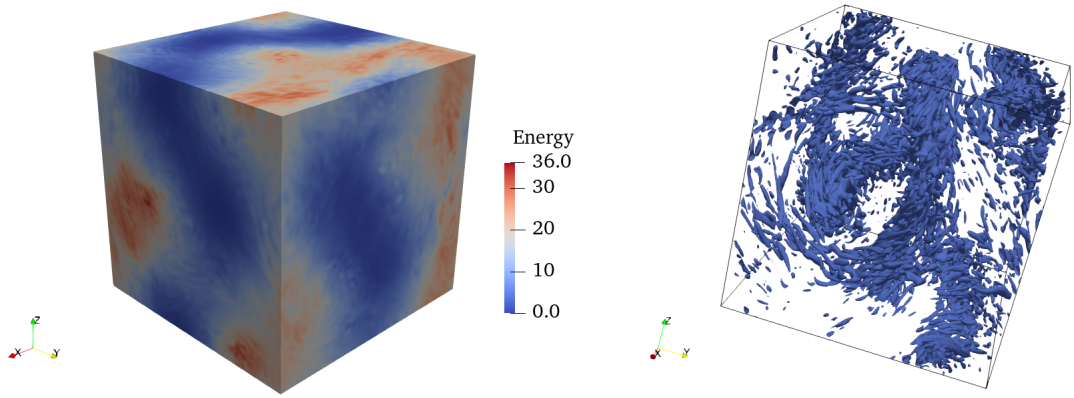

(a) (b)

Figure 6.13: Visualization of flows in the case where energy in two of the three directions is larger than that in the third direction at $t = 126$. (a) Energy. (b) Iso-enstrophy surface (where $\frac{1}{2}\omega_i\omega_i = 110$).

function in freely decaying 2D turbulence.

Chapter 7

Equilibrium statistical mechanics in 2D3C turbulence

In Sec. 2.3.1, we reviewed the derivation of equilibrium energy spectra in truncated 2D and 3D turbulence using statistical mechanics theories. In Sec. 4.1, we applied this theory to determine equilibrium energy spectra for 3D turbulence without vortex stretching. Furthermore, this statistical mechanics method can also be employed in other turbulent systems. In this chapter, we will provide the analytical derivation of equilibrium spectra for two-dimensional three-component (2D3C) turbulence, and compare these analytical predictions with the results obtained from direct numerical simulations. Note that we again consider incompressible, homogeneous, and isotropic (in the 2D plane) turbulence.

The organization of this chapter is as follows. In Section 7.1, we introduce fundamental concepts of 2D3C turbulence. Then, Section 7.2 provides the analytical derivations of the spectra of inviscid invariants. Subsequently, in Section 7.3, we present the numerical simulations and the evaluation of the analytical predictions. Lastly, Section 7.4 presents the conclusions of this chapter.

7.1 2D3C turbulence

2D3C flow is a type of 3D flow where one of the three velocity components is passively advected by the 2D flow formed in the other two directions. 2D3C flow is an idealized representation of turbulence with rapid rotation [117, 118], or magnetohydrodynamic (MHD) tur-

bulence with strong magnetic field [119–121]. Similar to turbulence without vortex stretching, 2D3C turbulence lies between 2D and 3D turbulence, and has been the subject of numerous research efforts [122–124]. In this chapter, we focus on the absolute equilibrium state of 2D3C flow in a spectrally (Galerkin) truncated system.

Without loss of generality, we choose the 2D plane to be the (x, y)-plane. In a 2D3C flow, the velocity can be decomposed into a 2D part $\boldsymbol{u}^{\mathrm{2D}} = \begin{pmatrix} u_x(x,y,t) \\ u_y(x,y,t) \\ 0 \end{pmatrix}$, and a component perpendicular to this 2D plane $\boldsymbol{u_z} = \begin{pmatrix} 0 \\ 0 \\ u_z(x,y,t) \end{pmatrix}$. The total velocity field is given by $\boldsymbol{u} = \boldsymbol{u}^{\mathrm{2D}} + \boldsymbol{u_z}$. The governing equations of velocity in a 2D3C flow are

$$\frac{\partial \boldsymbol{u}^{\mathrm{2D}}}{\partial t} = -(\boldsymbol{u}^{\mathrm{2D}} \cdot \nabla)\boldsymbol{u}^{\mathrm{2D}} - \nabla p + \nu \Delta \boldsymbol{u}^{\mathrm{2D}}, \tag{7.1}$$

$$\frac{\partial u_z}{\partial t} = -(\boldsymbol{u}^{\mathrm{2D}} \cdot \nabla) u_z + \nu \Delta u_z. \tag{7.2}$$

In these equations, Eq. (7.1) represents the Navier-Stokes equation of the 2D flow, and Eq. (7.2) illustrates that the z-component u_z is passively advected by the 2D flow. Next, we investigate the equations of vorticity. The vorticity associated with $\boldsymbol{u}^{\mathrm{2D}}$ can be calculated as

$$\nabla \times \boldsymbol{u}^{\mathrm{2D}} = \begin{pmatrix} 0 \\ 0 \\ \omega_z \end{pmatrix}. \tag{7.3}$$

with $\omega_z = \frac{\partial u_y}{\partial x} - \frac{\partial u_x}{\partial y}$. The vorticity associated with $\boldsymbol{u}^{\mathrm{2D}}$ is in the z direction. By taking the curl of Eq. (7.1), we can derive the governing equation of ω_z:

$$\frac{\partial \omega_z}{\partial t} = -(\boldsymbol{u}^{\mathrm{2D}} \cdot \nabla)\omega_z + \nu \Delta \omega_z. \tag{7.4}$$

Eq. (7.4) implies that ω_z is also advected by the 2D flow but backreacts on the flow through Eq. (7.3). The vorticity associated with $\boldsymbol{u}_z$ is

$$\boldsymbol{\omega}^{\mathrm{2D}} = \nabla \times \boldsymbol{u}_z = \begin{pmatrix} \frac{\partial u_z}{\partial y} \\ -\frac{\partial u_z}{\partial x} \\ 0 \end{pmatrix} = \begin{pmatrix} \omega_x \\ \omega_y \\ 0 \end{pmatrix}. \tag{7.5}$$

We can obtain the equation for $\boldsymbol{\omega}^{2\mathrm{D}}$ by taking the curl of Eq. (7.1):

$$\frac{\partial \boldsymbol{\omega}^{2\mathrm{D}}}{\partial t} = -(\boldsymbol{u}^{2\mathrm{D}} \cdot \nabla)\boldsymbol{\omega}^{2\mathrm{D}} + (\boldsymbol{\omega}^{2\mathrm{D}} \cdot \nabla)\boldsymbol{u}^{2\mathrm{D}} + \nu \Delta \boldsymbol{\omega}^{2\mathrm{D}}. \tag{7.6}$$

The second term on the RHS of Eq. (7.6) signifies the vortex stretching term, and it is not equal to zero trivially. However, it should be noted that the vortex stretching of the 2D part is zero, as can be seen from Eq. (7.4).

7.2 Analytical predictions

In this section, we will analytically derive the equilibrium spectra for inviscid invariants in 2D3C turbulence using the same method introduced in Sec. 2.3.1.

7.2.1 Formulas of modal inviscid invariants

As mentioned in Sec. 2.3.1 and 4.1, we should first investigate what the inviscid invariants in 2D3C turbulence are and examine the modal forms of these inviscid invariants.

From Eq. (7.1) and (7.4), we can infer that the 2D flow is independent of the z-component. Thus, as for 2D turbulence, the energy and enstrophy of the 2D part in 2D3C flow are inviscid invariants. The 2D energy and 2D enstrophy are defined as

$$E^{2\mathrm{D}} = \frac{\langle |\boldsymbol{u}^{2\mathrm{D}}|^2 \rangle}{2}, \tag{7.7}$$

and

$$W = \langle {\omega_z}^2 \rangle, \tag{7.8}$$

respectively. In addition, 2D3C flow belongs to the category of 3D systems. Thus it possesses inviscid invariants of 3D turbulence: total energy and helicity. As the 2D energy remains conserved in an inviscid system, the energy associated with the passive z-component, defined as

$$E^z = \frac{\langle u_z^2 \rangle}{2} \tag{7.9}$$

is also an inviscid invariant. Lastly, we consider the helicity. The helicity in the z direction can be defined as

$$H^z = \langle u_z \omega_z \rangle, \tag{7.10}$$

and the helicity in the 2D plane is defined as

$$H^{2\mathrm{D}} = \langle \boldsymbol{u}^{2\mathrm{D}} \cdot \boldsymbol{\omega}^{2\mathrm{D}} \rangle. \tag{7.11}$$

In homogeneous turbulence, we can employ the identity (2.7) to derive the relation:

$$H^z = \langle u_z \frac{\partial u_y}{\partial x} \rangle - \langle u_z \frac{\partial u_x}{\partial y} \rangle = -\langle u_y \frac{\partial u_z}{\partial x} \rangle + \langle u_x \frac{\partial u_z}{\partial y} \rangle = H^{2\mathrm{D}} \tag{7.12}$$

Considering that the total helicity $H = H^z + H^{2\mathrm{D}}$ is conserved, relation (7.12) indicates that H^z and $H^{2\mathrm{D}}$ are two inviscid invariants, but they are not independent.

Consequently, the modal entropy (S_n) can be expressed by the four independent inviscid invariants as

$$S_n = \alpha E_n^{2D} + \beta W_n + \gamma E_n^z + \delta H_n^z \tag{7.13}$$

where the subscript n represents the modal component of the corresponding inviscid invariants and $\alpha, \beta, \gamma, \delta$, and η are Lagrange parameters.

As discussed in Sec. 2.2.5, the velocity field of an incompressible 3D fluid can be decomposed using helical modes [35]. For incompressible 2D3C turbulence, we can specialize the two helical wave vectors $\boldsymbol{h}_\pm$ in Eq. (2.59) as $\boldsymbol{h}_{s_k} = \begin{pmatrix} \mathrm{i}s_k k_y/k \\ -\mathrm{i}s_k k_x/k \\ 1 \end{pmatrix}$ with s_k indicating symbols + or − [122]. Then the velocity in Fourier space can be expressed as

$$\hat{\boldsymbol{u}}(\boldsymbol{k}) = \hat{\boldsymbol{u}}^+(\boldsymbol{k}) + \hat{\boldsymbol{u}}^-(\boldsymbol{k}) = \hat{u}_z^+ \begin{pmatrix} \mathrm{i}k_y/k \\ -\mathrm{i}k_x/k \\ 1 \end{pmatrix} + \hat{u}_z^- \begin{pmatrix} -\mathrm{i}k_y/k \\ \mathrm{i}k_x/k \\ 1 \end{pmatrix} \tag{7.14}$$

where k_x, k_y represent the x, y components of the wave vector $\boldsymbol{k}$, respectively, and $\hat{u}_z^{s_k}$ denotes the z component of $\hat{\boldsymbol{u}}^{s_k}$. To simplify the notation, we will omit the $\boldsymbol{k}$ in $\hat{u}_z^{s_k}(\boldsymbol{k})$. By taking the curl of velocity, we can obtain the vorticity

$$\hat{\boldsymbol{\omega}}(\boldsymbol{k}) = k\hat{\boldsymbol{u}}^+(\boldsymbol{k}) - k\hat{\boldsymbol{u}}^-(\boldsymbol{k}) = k \left(\hat{u}_z^+ \begin{pmatrix} \mathrm{i}k_y/k \\ -\mathrm{i}k_x/k \\ 1 \end{pmatrix} - \hat{u}_z^- \begin{pmatrix} -\mathrm{i}k_y/k \\ \mathrm{i}k_x/k \\ 1 \end{pmatrix} \right). \tag{7.15}$$

Fourier components of the four independent inviscid invariants of 2D3C turbulence, E^{2D}, W, E^z, and H^z can then be expressed by $\hat{u}_z^+$ and $\hat{u}_z^-$ as

$$\begin{aligned}
E^z(\boldsymbol{k}) =& \frac{1}{2}(\hat{\boldsymbol{u}}(\mathbf{k})\cdot\boldsymbol{e_z})(\hat{\boldsymbol{u}}^*(\mathbf{k})\cdot\boldsymbol{e}_z) = \frac{1}{2}(\hat{u}_z^+ + \hat{u}_z^-)(\hat{u}_z^{+*} + \hat{u}_z^{-*}),\\
E^{\mathrm{2D}}(\boldsymbol{k}) =& \frac{1}{2}\left((\hat{u}_x^+ + \hat{u}_x^-)(\hat{u}_x^{+*} + \hat{u}_x^{-*}) + (\hat{u}_y^+ + \hat{u}_y^-)(\hat{u}_y^+ * + \hat{u}_y^{-*})\right)\\
=& \frac{1}{2}\left((\mathrm{i}k_y/k)(\hat{u}_z^+ - \hat{u}_z^-)(-\mathrm{i}k_y/k)(\hat{u}_z^{+*} - \hat{u}_z^{-*}) + (-\mathrm{i}k_x/k)(\hat{u}_z^+ - \hat{u}_z^-)(\mathrm{i}k_x/k)(\hat{u}_z^{+*} - \hat{u}_z^{-*})\right)\\
=& \frac{1}{2}(\hat{u}_z^+ - \hat{u}_z^-)(\hat{u}_z^{+*} - \hat{u}_z^{-*}),\\
W(\boldsymbol{k}) =& \frac{1}{2}(\hat{\boldsymbol{\omega}}(\mathbf{k})\cdot\boldsymbol{e_z})(\hat{\boldsymbol{\omega}}^*(\mathbf{k})\cdot\boldsymbol{e}_z) = \frac{1}{2}k(\hat{u}_z^+ - \hat{u}_z^-)k(\hat{u}_z^{+*} - \hat{u}_z^{-*}) = k^2E^{2D}(\boldsymbol{k}),\\
H^z(\boldsymbol{k}) =& \frac{1}{2}(\hat{\boldsymbol{u}}(\mathbf{k})\cdot\boldsymbol{e_z})(\hat{\boldsymbol{\omega}}^*(\mathbf{k})\cdot\boldsymbol{e}_z) = \frac{k}{2}(\hat{u}_z^+ + \hat{u}_z^-)(\hat{u}_z^{+*} - \hat{u}_z^{-*}).
\end{aligned} \tag{7.16}$$

Here, $\boldsymbol{e}_z$ indicates the unit vector in the z direction. Note that $\hat{u}_z^+$ and $\hat{u}_z^-$ are complex numbers. Thus, each Fourier mode $\hat{\boldsymbol{u}}(\boldsymbol{k})$ corresponds to four real-space components. Let's represent these four real components by $y_{n_1}, y_{n_2}, y_{n_3}, y_{n_4}$ with $\hat{u}_z^+ = y_{n_1} + \mathrm{i}y_{n_2}$, $\hat{u}_z^- = y_{n_3} + \mathrm{i}y_{n_4}$. Finally, the modal components of the four inviscid invariants are

$$\begin{aligned}
E_n^z =& \frac{1}{2}\left(y_{n_1}^2 + y_{n_2}^2 + y_{n_3}^2 + y_{n_4}^2 + 2y_{n_1}y_{n_3} + 2y_{n_2}y_{n_4}\right),\\
E_n^{\mathrm{2D}} =& \frac{1}{2}\left(y_{n_1}^2 + y_{n_2}^2 + y_{n_3}^2 + y_{n_4}^2 - 2y_{n_1}y_{n_3} - 2y_{n_2}y_{n_4}\right),\\
W_n =& \frac{k^2}{2}\left(y_{n_1}^2 + y_{n_2}^2 + y_{n_3}^2 + y_{n_4}^2 - 2y_{n_1}y_{n_3} - 2y_{n_2}y_{n_4}\right),\\
H_n^z =& \frac{k}{2}\left(y_{n_1}^2 + y_{n_2}^2 - y_{n_3}^2 - y_{n_4}^2 + 2\mathrm{i}y_{n_1}y_{n_4} - 2\mathrm{i}y_{n_2}y_{n_3}\right).
\end{aligned} \tag{7.17}$$

7.2.2 Equilibrium spectra

According to the fundamental principle of equilibrium statistical mechanics, it is understood that systems that fulfill the divergence-free condition in phase space will eventually have a uniform probability density across all accessible portions of the phase space. As a consequence, the partition function for mode n aligns with a Boltzmann-Gibbs equilibrium distribution, as expressed in:

$$P_n(y_{n_1}, ..., y_{n_4}) = C_n \exp[-S_n] \tag{7.18}$$

with C_n a constant. We can insert the expressions from Eq. (7.13) and Eq. (7.17) into Eq. (7.18), and then proceed to integrate P_n:

$$Z_n = \iiint \int_{-\infty}^{\infty} P_n \mathrm{d}y_{1n}\ \mathrm{d}y_{2n}\ \mathrm{d}y_{3n}\ \mathrm{d}y_{4n}. \tag{7.19}$$

We can compute this integral analytically to get the following:

$$Z_n = C_n \frac{\pi^2}{\alpha\gamma + (\beta\gamma - \delta^2)k^2}. \tag{7.20}$$

Following the methodology applied in Sec. 2.3.1, we can deduce the formulas of modal inviscid invariants from expression (7.20) as follows:

$$\begin{aligned}
\left\langle E_n^{\mathrm{2D}} \right\rangle &= -\frac{d\ln[Z_n]}{d\alpha} = \frac{\gamma}{\alpha\gamma + (\beta\gamma - \delta^2)k^2}, \\
\left\langle E_n^{z} \right\rangle &= -\frac{d\ln[Z_n]}{d\gamma} = \frac{\alpha + \beta k^2}{\alpha\gamma + (\beta\gamma - \delta^2)k^2}, \\
\left\langle H_n^{z} \right\rangle &= -\frac{d\ln[Z_n]}{d\delta} = -\frac{2\delta k^2}{\alpha\gamma + (\beta\gamma - \delta^2)k^2}.
\end{aligned} \tag{7.21}$$

We can observe that the formula for $\left\langle E_n^{\mathrm{2D}} \right\rangle$ is, not surprisingly, similar to that of modal energy found in classical 2D turbulence. The only difference is the substitution of $(\beta\gamma - \delta^2)$ with β. Furthermore, $\langle E_n^z \rangle$ acts as an equipartition in helicity-free cases, where δ equals to zero. It is also noteworthy that this formula of $\langle E_n^z \rangle$ is identical to the distribution of passive scalar typically observed in classical 2D turbulence.

The 2D spectra are obtained by multiplying Eq. (7.21) by $2\pi k$ as

$$E^{\mathrm{2D}}(k) = \frac{2\pi k}{\alpha + \beta' k^2}, \tag{7.22}$$

$$E^{z}(k) = \frac{\alpha + \beta k^2}{\gamma} \frac{2\pi k}{\alpha + \beta' k^2}, \tag{7.23}$$

$$W(k) = \frac{2\pi k^3}{\alpha + \beta' k^2}, \tag{7.24}$$

$$H^{z}(k) = -\frac{2\delta}{\gamma} \frac{2\pi k^3}{\alpha + \beta' k^2}. \tag{7.25}$$

with

$$\beta' = \beta - \delta^2/\gamma. \tag{7.26}$$

We can observe that Eq. (7.22) has the same formula as Eq. (2.72) with β' in Eq. (7.22) playing the role of β in Eq. (2.72).

7.2.3 Integral relations between inviscid invariants for the equilibrium distributions

Because the 2D energy and 2D enstrophy are conserved quantities of the 2D part of our system, the statistical characterization of this 2D part in the equilibrium state is completely determined by the values of the 2D energy and 2D enstrophy,

$$E^{2D} = \int_{k_{\min}}^{k_{\max}} E^{2D}(k)\mathrm{d}k, \quad W = \int_{k_{\min}}^{k_{\max}} W(k)\mathrm{d}k \tag{7.27}$$

as soon as we know $k_{\min}$ and $k_{\max}$ and the initial conditions. By substituting Eq. (7.22) and (7.24) into Eq. (7.27), it can be deduced that the values of α and β' can be determined only by E^{2D} and W, implying that the third component has no influence on the shape of $E^{2D}(k)$ and $W(k)$. It indicates that the dynamics of the third component have no influence on the dynamics of the 2D part.

By deriving from Equation (7.24) and (7.25), we can establish a relation between the spectra of 2D enstrophy and helicity in the z direction (and also in the 2D plane) as

$$H^z(k) = -\frac{2\delta}{\gamma}W(k). \tag{7.28}$$

The relation (7.28) is linear, attributed to the fact that both u_z and ω_z are passively advected by the 2D flow. Subsequently, we can also derive the linear relationship between W and H^z (or H^{2D}) as

$$H^z = -\frac{2\delta}{\gamma}W. \tag{7.29}$$

The integration of Equations (7.22), (7.23), and (7.24) offers us a relation between the energy in the z direction, 2D energy, and 2D enstrophy as

$$E^z = \frac{\alpha}{\gamma}E^{2D} + \frac{\beta}{\gamma}W. \tag{7.30}$$

By substituting equations (7.29) and (7.30) into (7.26), we can derive the expression of β as

$$\beta = \frac{\beta' + \alpha\frac{E^{2D}}{W}H_{\mathrm{rel}}^2}{1 - H_{\mathrm{rel}}^2} \tag{7.31}$$

with $H_{\mathrm{rel}} = \frac{H_z}{\sqrt{WE^z}}$.

7.3 Numerical simulations

[1] In order to verify the analytical predictions in Sec. 7.2, we execute DNS.

7.3.1 Setup

The numerical code used for the simulation is the GHOST code (Geophysical High-Order Suite for Turbulence), which is a standard pseudo-spectral solver [125]. For detailed information on the numerical method, please refer to the doctoral thesis by Wesley (citation).

The 2D-Euler equation is calculated with a grid of 256^2 with no external forces applied. The initial energy spectrum of the 2D flow is set as a Gaussian function $E^{\mathrm{2D}}(k) = Ce^{-(k-3)^2/8}$ with C serving as a normalization constant, ensuring that the 2D energy E^{2D} equals 1. For initializing the spectrum of the z component, we utilize the technique introduced in Sec. 4.2.1. We generate two velocity fields, $\boldsymbol{u}_a$, and $\boldsymbol{u}_b$, with identical energy spectra but different random phases. Then we establish a linear combination of these two fields as $\boldsymbol{u}_c = \boldsymbol{u}_a + \lambda \boldsymbol{u}_b$, where the coefficient λ is determined by the value of relative helicity. The relative helicity of field $\boldsymbol{u}_c$ can be represented as

$$H_r = \frac{\frac{1}{2}\langle \boldsymbol{u}_c \cdot \boldsymbol{\omega}_c \rangle}{\sqrt{\frac{1}{2}\langle \boldsymbol{u}_c \cdot \boldsymbol{u}_c \rangle \frac{1}{2}\langle \boldsymbol{\omega}_c \cdot \boldsymbol{\omega}_c \rangle}} = \frac{\langle (\boldsymbol{u}_a + \lambda \boldsymbol{u}_b) \cdot (\boldsymbol{\omega}_a + \lambda \boldsymbol{\omega}_b) \rangle}{\sqrt{\langle (\boldsymbol{u}_a + \lambda \boldsymbol{u}_b)^2 \rangle \langle (\boldsymbol{\omega}_a + \lambda \boldsymbol{\omega}_b)^2 \rangle}}. \tag{7.32}$$

Given that the variables $\boldsymbol{u}_a$, $\boldsymbol{\omega}_a$, $\boldsymbol{u}_b$, and $\boldsymbol{\omega}_b$ are known, once the value of relative helicity H_r is determined, equation (7.32) allows for the calculation of λ.

In this chapter, we execute six simulations with relative helicity values of $H_r = 0$, 0.28, 0.51, 0.66, 0.83, 1. In all these six cases, $E^{\mathrm{2D}} = 1$, $E^z = 2.54$, and $W = 28.41$.

7.3.2 Results

Fig. 7.1(a) shows the 2D energy spectra in six cases, with the black line denoting the analytical predictions. The nearly overlapping 2D energy spectra in the cases with different relative helicity values affirm our prediction in Sec. 7.2.3. Simulation results align with the analytical prediction at small scales. However, a deviation appears at large scales, approximately when

[1] The research conducted in this chapter represents a collaboration with my colleague, Wesley Agoua, a Ph.D. student in my group. Wesley took charge of executing all numerical simulations. I gratefully acknowledge his valuable contributions.

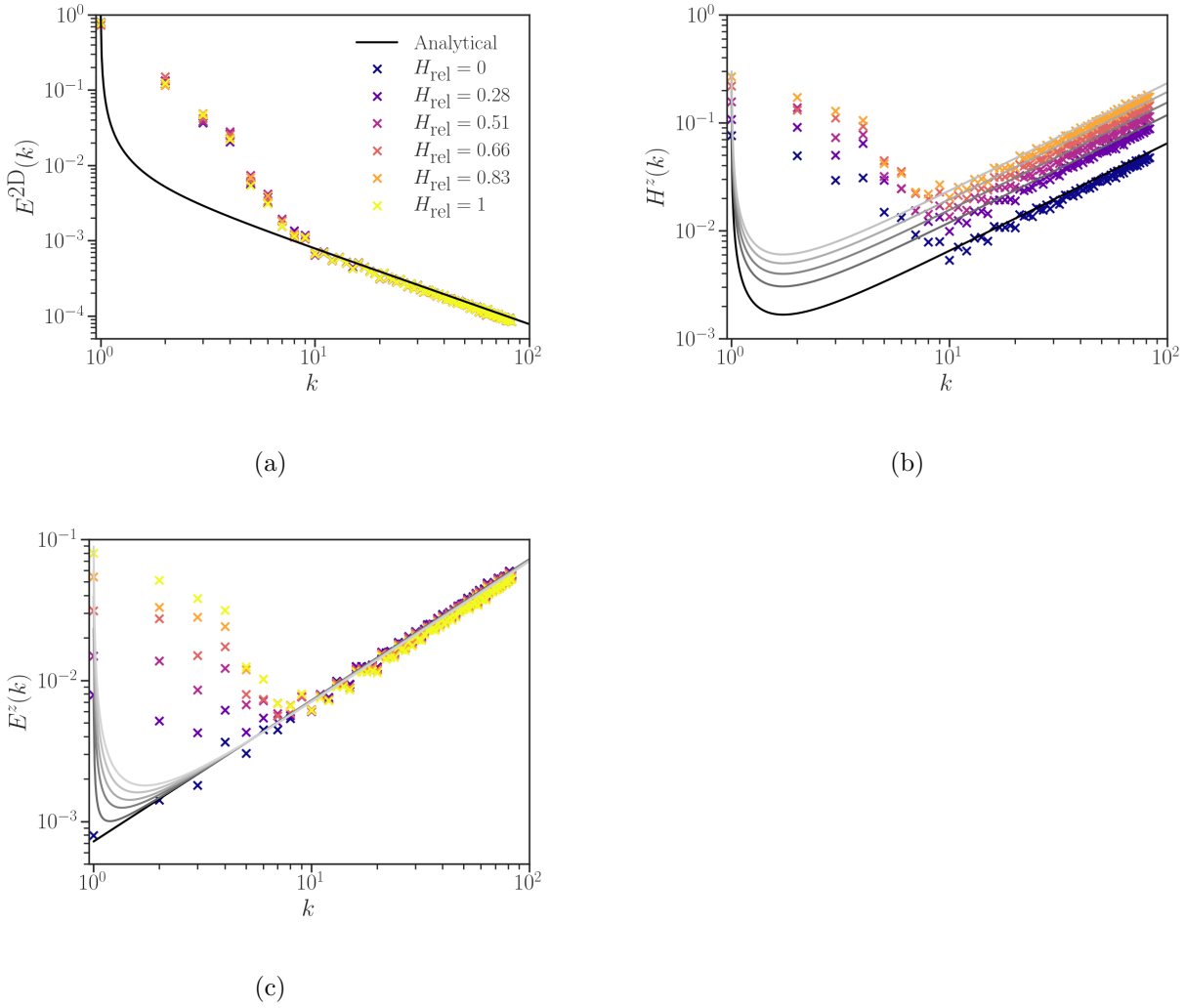

Figure 7.1: Spectra of inviscid invariants in 2D3C turbulence at the absolute equilibrium state with different relative helicities. (a) Energy spectrum of the 2D part ($E^{2\mathrm{D}}(k)$). (b) Helicity spectrum ($H^z(k)$). (c) Energy spectrum of the z-component ($E^z(k)$). The black line in (a) is the analytical 2D energy spectrum which is the same in all six cases. Grey lines in (b) and (c), progressing from dark to light, correspond respectively to cases with relative helicity values of $H_r = 0$ (only in (c)), 0.28, 0.51, 0.66, 0.83, 1.

wave numbers are $k < 10$. This deviation is plausibly caused by the presence of large-scale structures. In these scales, equilibrium statistical mechanics does thus not seem to predict the correct kinetic energy distribution.

The helicity spectra in the z direction are presented in Fig. 7.1(b). Note that the case where $H_{\mathrm{rel}} = 0$ is omitted as $H^z(k) = 0$ is trivial. We can observe that the profiles of $H^z(k)$ are almost the same (but with shifts) in different cases. This characteristic can be inferred from Eq. (7.28) and (7.29). $W(k)$ is the same in all six cases, and the shape of $H^z(k)$ remains consistent. Diverse ratios of H^z and W result in different values of $-2\delta/\gamma$, corresponding to the observed shifts. Simulations coincide with the analytical prediction on a smaller scale. However, again a deviation emerges at larger scales.

Fig. 7.1(a) shows the energy spectrum of the z-component. We can find that the shapes of spectra change with the values of relative helicity values, which verifies Eq. (7.31). Comparing the $H^z = 0$ case with the other five cases, we can observe that the large-scale structures of energy in the z direction can be attributed to the influence of helicity.

7.3.3 Supplemental simulations

In order to investigate the large-scale deviation of spectra, we execute DNS using a grid of 512^2 and different initial energy spectra: $E^{\mathrm{2D}}(k) = C_1 e^{-(k-4)^2/8}$, $E^{\mathrm{2D}}(k) = C_2 e^{-(k-80)^2/8}$, and $E^{\mathrm{2D}}(k) = C_3 e^{-(k-130)^2/8}$ with C_1, C_2, and C_3 serving as normalization constants, ensuring that the 2D energy E^{2D} equals 1. The values of 2D enstrophy W are 29.8, 6432, and 16931, respectively. Different ratios of E^{2D} to W determine the shapes of energy spectra at the absolute equilibrium state [126].

Fig. 7.2 shows the energy spectra at the absolute equilibrium state. We can observe that the large-scale deviation is less apparent in Fig. 7.2(b) and (c) than in (a). The 2D energy is not condensed at the first modes in the cases (b) and (c). Consequently, a plausible explanation of this derivation could be that the large-scale structures obstruct the relaxation process towards the final absolute equilibrium state. This feature, which is not explained by equilibrium statistical mechanics, needs further investigation.

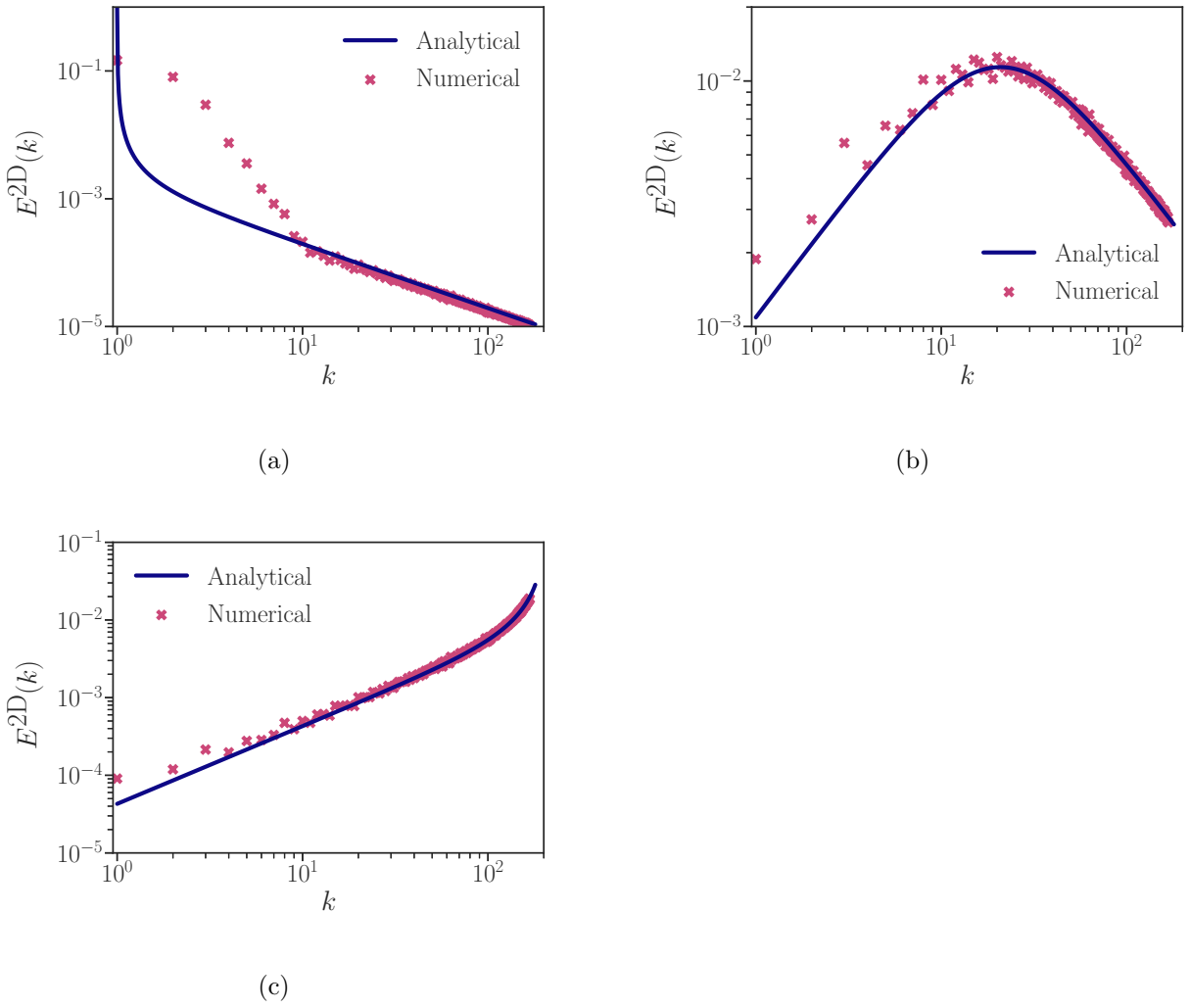

(a)

(b)

(c)

Figure 7.2: 2D energy spectra of spectrally truncated 2D3C turbulence at absolute equilibrium states with different initial fields. Black lines are analytical predictions. The initial energy spectra are set to be (a) $E^{2D}(k) = C_1 e^{-(k-4)^2/8}$, (b) $E^{2D}(k) = C_2 e^{-(k-80)^2/8}$, and (c) $E^{2D}(k) = C_3 e^{-(k-130)^2/8}$.

7.4 Conclusion

In this section, we have investigated spectrally truncated 2D3C flows using statistical mechanics and numerical simulations. In 2D3C flows, there are four independent inviscid invariants: 2D energy E^{2D}, 2D enstrophy W, energy of the z-component E^z, and helicity in the z direction H^z (or helicity in the 2D plan H^{2D}). By applying statistical mechanics, using these inviscid invariants, we analytically derive the exact formulas of equilibrium spectra. In particular, we find that helicity determines the large-scale behavior of the energy distribution of the third velocity component. DNSs are executed to verify these analytical predictions. The numerical results align with the analytical prediction at small scales. However, a large-scale deviation appears when 2D energy is condensed at the first modes. This deviation can plausibly be caused by the emergence of large-scale structures.

The investigation of 2D3C turbulence connects turbulence without vortex stretching with real-world turbulence. Given the absence of vortex stretching in the 2D part, the most important part of a 2D3C flow, 2D3C turbulence is a "real-world system" resembling turbulence without vortex stretching. Indeed, in both systems, helicity affects the equilibrium energy distributions at the largest scales.

Chapter 8

Conclusion and Perspectives

Turbulent behaviors in 2D and 3D systems exhibit significant differences. One of the key distinctions between 2D and 3D turbulence is the naturally absent vortex-stretching term in 2D turbulence. Many recent studies suggest that vortex stretching plays a crucial role in the forward energy cascade in 3D turbulence, which contrasts with the inverse energy cascade observed in 2D turbulence. In this thesis, we investigated a novel turbulent system, turbulence without vortex stretching, under isotropic, homogeneous, and incompressible conditions. Our objective was to investigate the vortex-stretching mechanism by eliminating it in 3D turbulence and comparing the resultant system with standard 3D turbulence. This novel turbulent system was investigated in three states: the absolute equilibrium state (Chapter 4), the cascade state (Chapter 5), and the condensation state (Chapter 6).

We first studied the Euler equation after removing the vortex stretching in a spectrally truncated system. This system eventually relaxed to an absolute equilibrium state. Our primary focus in the absolute equilibrium state was to apply statistical physics with the helical decomposition of velocity to predict exact formulations of the energy, helicity, and enstrophy spectra (Eq. (4.19) and (4.20)). Subsequently, these analytical predictions were validated through DNS. The numerical results of the spectra are summarized in Figure 4.5. From these figures, we observe that in the absence of helicity, the final state corresponds to an equipartition of enstrophy, indicative of a thermal equilibrium of Fourier modes where enstrophy is evenly distributed on average. In contrast, in a helical system, a condensation of energy and helicity occurs in the largest scales of the system. This condensation suggests that the largest scales of turbulence without vortex stretching are strongly influenced by

helicity, unlike classical 3D turbulence, where helicity affects the smallest scales. The large-scale structure associated with this condensation is an ABC flow, which can be considered as a 3D extension of the 2D pair of rotating vortices, observed as a condensate in 2D turbulence.

In this thesis, we unveiled the existence of two inviscid invariants in turbulence without vortex stretching: enstrophy and helicity. From the equilibrium state results, we observed that most helicity is contained at the largest scales, and most enstrophy is contained at the smallest scales. This outcome enabled us to predict the cascade directions of the two inviscid invariants: enstrophy cascades from larger to smaller scales, while helicity undergoes an inverse cascade towards larger scales. We also illustrated the spectral scalings associated with these two cascades using dimensional analysis. In the inertial range of the forward cascade, energy and helicity spectra follow $E(k) \propto k^{-3}$ and $|H(k)| \propto k^{-2}$, associated with a conserved enstrophy flux towards large k. Closer to the forcing scale, logarithmic corrections allowed us to describe the deviation of the spectral energy distribution from the dimensional prediction. For the inverse cascade, we have $E(k) \propto k^{-7/3}$ and $|H(k)| \propto k^{-4/3}$. These wave number ranges are associated with a constant (conserved) helicity flux towards small wave numbers. We also made an effort to investigate the transition of flow properties between the two limiting cases: normal turbulence and turbulence without vortex stretching. By filtering the strain-rate tensor, we observed that the statistics change dramatically for a critical value of the filter width.

Since helicity undergoes an inverse cascade towards larger scales and carries energy, in the absence of friction or other forms of large-scale damping, helicity will accumulate, as energy does for 2D turbulence. This large-scale structure persists for a period after the force is eliminated. As this condensation behavior resembles 2D turbulence, we applied statistical physics and a generalized 3D point-vortex model to analyze turbulence without vortex stretching. We successfully predicted a hyperbolic sine relation between vorticity and velocity in each direction. We executed DNS in both forced and freely-decaying systems. In a force-dissipative system, the predicted hyperbolic sine relation can be found between the averaged vorticity and velocity. In the freely decaying system, the relation between vorticity and velocity very clearly relaxes to the predicted hyperbolic sine function, similar to the sinh relation between vorticity and stream function in freely decaying 2D turbulence.

Our study of 3D turbulence without vortex stretching makes a bridge between 2D and 3D turbulence. We observed that after eliminating vortex stretching from 3D turbulence, energy

is carried towards larger scales, forming a condensation structure. This 2D behavior emerges within a 3D system, providing valuable insights and enhancing our understanding of the vortex-stretching mechanism in turbulence. Moreover, our successful application of statistical physics in predicting the behaviors of turbulence without vortex stretching demonstrates the continued relevance and power of statistical physics in studying turbulence, even though natural turbulence is far from equilibrium.

There are several interesting avenues for future research in this PhD project. First, we can assess the chirality of flow structures in the inverse helicity cascade case, as the relationship between helicity and energy spectra is approximately $|H(k)| = kE(k)$, corresponding to homochiral modes. Second, we can investigate whether intermittency is altered after removing the vortex stretching. Finally, by employing a similar method, we might explore a system that excludes the strain self-amplification term, which also plays a crucial role in the energy cascade. However, it is not clear at present whether it is possible to remove strain self-amplification only from the system while keeping the vortex stretching.

Appendix A

Exciting turbulence in an elongated domain

[1] In addition to the main PhD project on turbulence without vortex stretching, we have also investigated another novel turbulent system: turbulence in an elongated domain. In this study, we consider the conventional Navier-Stokes equations.

Motivated by recent experimental results in grid turbulence with very long streamwise velocity correlations, we consider numerical simulations of turbulence in a domain that is elongated in one direction. Energy is injected in the largest wavelengths of the system. Compared to turbulence in traditional cubic domains, larger Reynolds numbers, wider inertial ranges, more significant intermittency, and longer surviving large-scale motions are obtained in elongated domains. A mixed Taylor-scale Reynolds number is defined to describe the ratio between inertial and viscous dynamics for elongated turbulence.

The rest of this chapter is organized as follows. Sec. A.1 presents an introduction to this project. In Sec. A.2, we describe the numerical setup for turbulence in elongated and traditional cubic domains. Then we present the numerical results in Sec. A.3. Finally, Sec. A.4 presents the conclusions.

[1] This investigation is carried out in collaboration with professors Le Fang and Joachim Peinke.

A.1 Introduction

Grid-generated turbulence in wind tunnels is a classical set-up to experimentally study homogeneous and isotropic turbulence [127–130]. To assess asymptotic predictions of high Reynolds number turbulence, experiments have been designed using active grids [131–135] allowing to obtain a larger turbulence intensity and thereby a larger Reynolds number than with classic static grids. Recently grid-turbulence experiments have succeeded in generating unexpectedly high Reynolds number flows [136]. The important point in succeeding this was the excitation of extremely long streamwise scales. A surprising observation in this experiment was the intermittency properties of the smallest scales. Indeed, in the modern description of turbulent flows, the statistics of the smallest scales depend on the Reynolds number [137]. This difference is not contained in the classic K41 theory of turbulence [138], but is inherent to the build-up of intermittency as formulated first in the K62 framework [28, 139], and further addressed in more sophisticated theoretical frameworks [140–143]. The most salient feature of the recent wind-tunnel results [136] is the behavior of the velocity-increment flatness of the (streamwise) longitudinal increments. Indeed, this quantity showed a build-up of intermittency through scale space starting at these very large scales. Its small-scale value is thereby significantly larger than in turbulence excited at the length-scale comparable to the transverse dimensions of the wind tunnel [136]. This experimental set-up managed thereby to achieve a much higher value of the effective Reynolds number than obtainable by a random stirring protocol. The experiments improved thereby upon previous attempts to increase the Reynolds number by tuning the forcing protocol of active grids [133, 135, 144, 145].

In the present investigation, we assess the influence of long wavelength forcing on small scales using Direct Numerical Simulations (DNSs) in an elongated domain. Our flow domain is a square prism (Fig. A.1) whose length in one direction is larger than that in the other two directions. We also refer to this elongated domain as a quasi-one-dimensional (quasi-1D) domain. In pipe flow [146], channel flow [147, 148], and turbulent boundary layers [149, 150], structures are observed significantly larger than the cross-stream dimension of the geometry. In contrast to wall-bounded turbulence, research on wall-free turbulence in quasi-1D domains is currently limited. Presently, wall-free turbulence in elongated domains has been used to study the anisotropy of magnetohydrodynamic turbulence [151, 152], homogeneous shear turbulence simulations [153] and fast-rotating turbulence where domains are elongated in order to investigate turbulence at low Rossby number [109, 154, 155]. In this chapter, we

use quasi-1D turbulence to simulate the experimental features in an even more controlled setting than grid turbulence. Before discussing the results, we stress that the goal is not to reproduce the wind-tunnel experiments but to investigate the most important features and to understand them better. In particular we study the influence of flow scales with a wavelength of the order of the domain length on the smallest scales of the flow.

A.2 Numerical setup

In this section, we detail the numerical setup we have used. During the simulations, we first force the turbulent system at very long length scales, then remove the force and let turbulence freely decay. Results are obtained during both the statistically stationary state and the decay phase.

A.2.1 Elongated and cubic calculation domains

In order to simulate grid turbulence with a long streamwise correlation length, we extend a cubic box in the z-direction by a factor of eight. The calculation domain is thus chosen as $L_x \times L_y \times L_z = (2\pi)^2 \times 16\pi$. Simulations are executed for resolutions of grids of $N_x \times N_y \times N_z = 64^2 \times 512$, $128^2 \times 1024$ and $256^2 \times 2048$. The numbers of grid points in the z-direction are thus also eight times larger than those in x- and y-directions. Additional simulations are executed in traditional cubic domains to compare the results with the elongated ones. For cubic cases, the calculation domain is $L_x \times L_y \times L_z = (2\pi)^3$ with three corresponding resolutions $N_x \times N_y \times N_z = 64^3$, 128^3 and 256^3. Periodic boundary conditions are used in each direction.

A.2.2 External force

In our simulations, an external force is added at long length scales. Properties of turbulence in elongated domains are first investigated during a statistically steady state where the input energy rate is equal to the dissipation rate. After reaching the steady state, we remove the external force. Then turbulence decays freely with time, corresponding to grid turbulence decaying along the streamwise direction.

The equation that will be considered is the Navier-Stokes equation, where an external

force $\boldsymbol{F}$ is added

$$\frac{\partial \boldsymbol{u}}{\partial t} + \boldsymbol{u} \cdot \nabla \boldsymbol{u} = -\frac{1}{\rho}\nabla p + \nu \nabla^2 \boldsymbol{u} + \boldsymbol{F} \tag{A.1}$$

together with the divergence-free condition $\nabla \cdot \boldsymbol{u} = 0$, $\boldsymbol{u}$ the velocity, p the pressure, ρ the density and ν the kinematic viscosity. For the forcing term, we use the random force introduced by Alvelius [156]. Alvelius introduced a random scheme with a force $\hat{f}_i(\boldsymbol{k}, t) = A(\boldsymbol{k}, t)e_i^{(1)}(\boldsymbol{k}) + B(\boldsymbol{k}, t)e_i^{(2)}(\boldsymbol{k})$, where $e_i^{(1)}$ and $e_i^{(2)}$ are unit vectors orthogonal to each other and to the wave vector $\boldsymbol{k}$. In our code, this force is applied to the first two wave-number shells $0.5\Delta k \leq ||\boldsymbol{k}|| < 1.5\Delta k$ and $1.5\Delta k \leq ||\boldsymbol{k}|| < 2.5\Delta k$ with $\Delta k = 2\pi/L_z = 1/8$ for the elongated cases and $\Delta k = 1$ for the cubic cases. Note that in the elongated domains, the force is only applied in the k_z direction since, in the other directions, no k_x, k_y wave-vector components lay in the first two shells. Conversely, the force is added in an isotropic manner in the cubic cases. The forcing in the elongated runs is thus necessarily anisotropic. At each time step and grid point, coefficients $A(\boldsymbol{k}, t)$ and $B(\boldsymbol{k}, t)$ are randomly varied. Then multiplied by the same factor to make sure $|A(\boldsymbol{k}, t)|^2 + |B(\boldsymbol{k}, t)|^2 = \frac{P}{2\pi k^2}$ where $P = 1$ and k is chosen as the median of each shell, i.e., $k = 1/8$ and $k = 1/4$ in elongated cases and $k = 1$ and $k = 2$ in cubic cases.

We choose values of ν to obtain $k_{max}\eta \approx 1.8$ with η the Kolmogorov length scale defined as $\eta = (\nu^3/\epsilon)^{1/4}$ in each cubic simulation. Then the viscosity value of each corresponding elongated case is set to be the same. In our simulations, ν is chosen as $1/60$ for 64^3 and $64^2\times512$ cases, $1/210$ for 128^3 and $128^2\times1024$ cases, $1/600$ for 256^3 and $256^2\times2048$ cases. All the reported results are independent of the randomly chosen initial conditions.

A.3 Numerical results

In this section, we present the results of the numerical integration of Eq. (A.1). We first show the results during the statistically steady state in Sec. A.3.1. Then, in Sec. A.3.2, numerical results during the free-decaying stage are presented.

A.3.1 Turbulence at steady states

Visualization of the flows

Fig. A.1 shows, from top to bottom, visualization of iso-enstrophy surfaces, x- and z-components of velocity in the $256^2\times2048$ case at the steady state. Visualizations of u_y are similar to those of u_x, so u_y is not presented. The top picture shows small-scale structures, which seem to be organized in cluster-like patterns. The middle picture of Fig. A.1 shows that in elongated cases, u_x at large scales is large compared to u_z. The flow can be imagined as a small slice through a much larger shear flow. This shear with velocity in the x- and y-directions comes from the force we added at large scales in the k_z-direction. For an incompressible fluid, velocity vectors in Fourier space are perpendicular to their corresponding wave vectors. Consequently, the force added at the k_z-directional vectors in Fourier space induces velocity fluctuations in x- and y-directions in physical space. No energy is added into the z-direction directly by the external force. Therefore, u_z is smaller than u_x, which can be observed in the bottom picture of Fig. A.1. Note that the large-scale shear profile changes its position with time.

Time evolution of integral quantities

In this subsection, we show the time evolution of integral quantities during the steady states. Note that the time evolution before reaching these steady states is ignored. Time in each case is normalized by its characteristic time scale $\tau = \frac{\langle||\boldsymbol{u}||^2\rangle}{\epsilon}$ where ϵ is the dissipation rate and $\langle\bullet\rangle$ indicates the volume average. Because simulations of the $256^2\times2048$ case are demanding with respect to numerical resources, this calculation is stopped at 1.1τ after the beginning of the steady state. And we show 2τ of time evolution for the other cases. Note that values of τ are different in different cases.

The time evolution of energy in the elongated and cubic cases is shown in Fig. A.2. We find that the energy of the elongated simulations is nearly 50 times larger than that of the cubic cases. Fig. A.3(a) represents the time evolution of Taylor-scale Reynolds numbers, defined as $\mathrm{Re}_\lambda = \sqrt{\frac{20}{3}}\frac{K}{\sqrt{\nu\epsilon}}$ with $K = \frac{1}{2}\langle u_x^2 + u_y^2 + u_z^2\rangle$ the energy, for the six simulations. The formula of Taylor-scale Reynolds number can also be written as $\mathrm{Re}_\lambda = u'\lambda_g/\nu$ with λ_g the Taylor length scale and u' the root-mean square velocity. Fig. A.3(a) shows that Taylor-scale Reynolds numbers are of order 10^3 for elongated cases, while Reynolds numbers in the

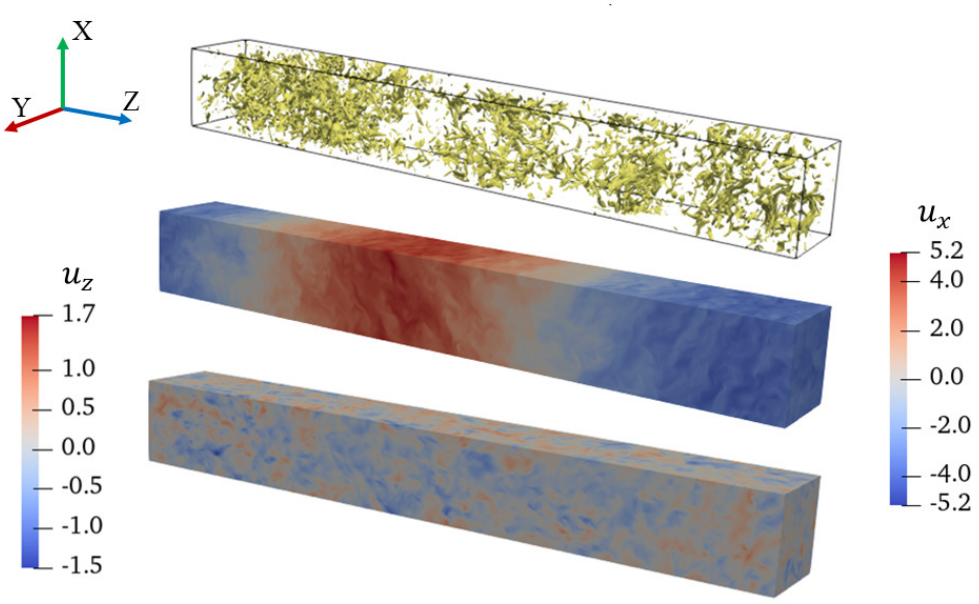

Figure A.1: Visualization of flows in elongated domain with the grid of $256^2 \times 2048$ at the steady state. Top: iso-enstrophy surfaces. Middle: x-component of velocity (u_x). Bottom: z-component of velocity (u_z).

cubic cases do not exceed a value of 100. These observations show that if we compute the Reynolds number Re_λ based on the velocity fluctuations, it is enormous in elongated cases since it reflects the large value of the shear flow at $k = 1/8$ and $k = 1/4$. However, it should be realized that λ_g is a length scale based on a velocity correlation [27]. In elongated cases, flows are not isotropic, and the correlation length in the z-direction is much smaller than that in x- and y-directions. Thus in order to better characterize the nature of the fluctuations without the very anisotropic shear flow, we define a mixed Taylor-scale Reynolds number where the Taylor length scale is based on the fluctuations in the z-direction, keeping $u' = \sqrt{K}$ the same in the definition. The formula of the mixed Taylor-scale Reynolds number is written as follows

$$\mathrm{Re}_\lambda^{\mathrm{mix}} = \sqrt{\frac{20}{3}} \frac{\sqrt{\frac{3}{2}\langle u_z^2 \rangle}\sqrt{K}}{\sqrt{\nu\epsilon}}. \tag{A.2}$$

Fig. A.3(b) shows the time evolution of mixed Taylor-scale Reynolds numbers in the three elongated cases. It is observed that the mixed Reynolds numbers in elongated domains are an order of magnitude smaller than those computed by using the classical definition, but still significantly larger than the values obtained in the cubic domains. The relation between Taylor-scale Reynolds number and high-order quantities will be studied in Sec. A.3.1.

Energy and energy-flux spectra

This subsection presents time averages of energy and energy-flux spectra during steady states. Time averages in all cases are performed during an interval 5τ, except for that in the $256^2 \times 2048$ case, where the interval is τ.

In Fig. A.4(a), energy spectra and wave-numbers are normalized by $(\epsilon\nu^5)^{1/4}$ and Kolmogorov length scale η respectively. The 3D energy spectrum is defined as

$$E_{3\mathrm{D}}(k) = \frac{1}{2} \sum_{k-0.5\Delta k \le ||\boldsymbol{p}|| < k+0.5\Delta k} \hat{\boldsymbol{u}}(\boldsymbol{p}) \cdot \hat{\boldsymbol{u}}^*(\boldsymbol{p}). \tag{A.3}$$

The spectra of the cubic simulations are very close to those of the elongated runs for $k > 1$. Therefore, for clarity, in Fig. A.4(a) the energy spectra of cubic cases are multiplied by 10. The inset shows the compensated spectra $k^{5/3}\epsilon^{-2/3}E_{3\mathrm{D}}(k)$. We observe inertial ranges with a wavenumber dependence close to $k^{-5/3}$. Inertial ranges are also present in the spectra of

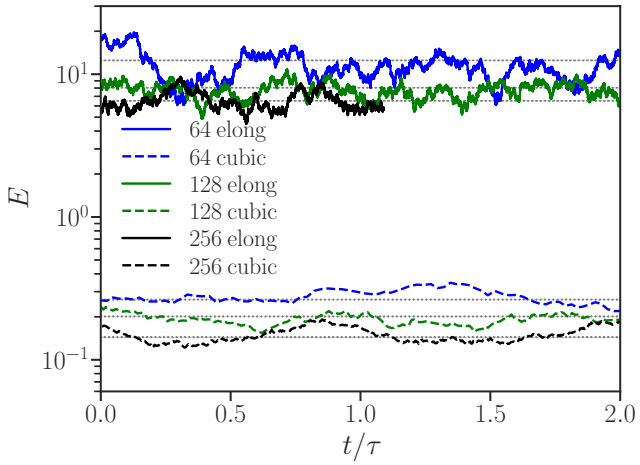

Figure A.2: Time evolution of turbulent kinetic energy in elongated and cubic cases during the statistically steady states. Gray dotted lines indicate the mean values in each case.

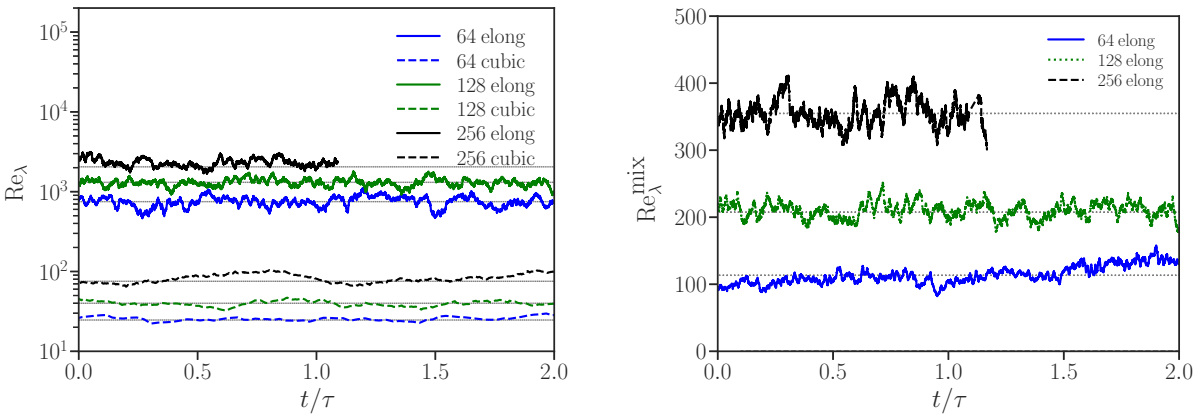

(a) (b)

Figure A.3: Time evolution of Reynolds numbers during steady states. (a) Taylor-scale Reynolds numbers in six cases. (b) Mixed Taylor-scale Reynolds numbers in elongated cases. Gray dotted lines in both (a) and (b) indicate the mean values in each case.

energy fluxes $\Pi(k)$ normalized by dissipation rate ϵ in Fig. A.4(b). The energy flux is defined as

$$\Pi(k) = \int_{\Sigma_k} \mathfrak{Re}\left[\mathcal{F}[\boldsymbol{u}\cdot\nabla\boldsymbol{u}](\boldsymbol{k})\cdot\hat{\boldsymbol{u}}^*(\boldsymbol{k})\right] d\boldsymbol{k} \tag{A.4}$$

where $\mathcal{F}_{[\bullet]}$ and $\hat{\bullet}$ indicate Fourier transforms and $\mathfrak{Re}[\bullet]$ represents the real part of the quantity in brackets. Σ_k is the spherical domain in Fourier space consisting of all wave vectors with $\|\boldsymbol{k}\| \leqslant k$. We observe plateaus, which indicate inertial ranges, between $k \approx 0.3$ and $k \approx 1$ in the three elongated cases. Moreover, we observe that energy spectra in different cases overlap at large wave numbers. Dips are present in energy spectra of elongated cases in Fig. A.4(a) at small wave numbers. These dips result from the anisotropy of the flows. An explanation for the presence of these dips, from the perspective of triad interactions, is as follows. We know that energy is transferred across different scales through triad interactions. In our simulations, for $1/8 \leq k < 1$, we only have wave vectors in the z direction. To form triads with vectors in the forcing range, which are also in the same direction, the triad becomes degenerate, essentially forming a line. Such triads cannot transfer energy [35]. Consequently, the dips can only be filled indirectly through an inverse cascade of energy at modes with $k \geq 1$. It is important to note that the inverse cascade is not the primary mechanism for energy transfer in 3D turbulence, so that the dips are a persistent feature of the flows in the elongated flow geometry.

One-dimensional energy spectra are also investigated. The 1D energy spectrum is defined as

$$E_{1\mathrm{D}}(k_z) = \frac{1}{2} \sum_{k_z - 0.5\Delta k \leq p_z < k_z + 0.5\Delta k} \hat{\boldsymbol{u}}(\boldsymbol{p})\cdot\hat{\boldsymbol{u}}^*(\boldsymbol{p}). \tag{A.5}$$

Fig. A.5 shows the normalized 1D energy spectra in six cases, and the inset shows the compensated spectra $k_z^{5/3}\epsilon^{-2/3}E_{1\mathrm{D}}(k_z)$. The dips which were present in $E_{3\mathrm{D}}(k)$ are no longer visible in this representation, and we can see more clearly inertial ranges in the elongated cases.

These observations show that inertial ranges are more easily obtained using an elongated calculation domain. Turbulence in elongated cases allows thus to obtain higher Reynolds numbers. The two reasons for this are that, firstly a large kinetic energy is present in the longest wavelengths of the system, secondly the larger spectral interval allows more easily the establishment of an inertial range.

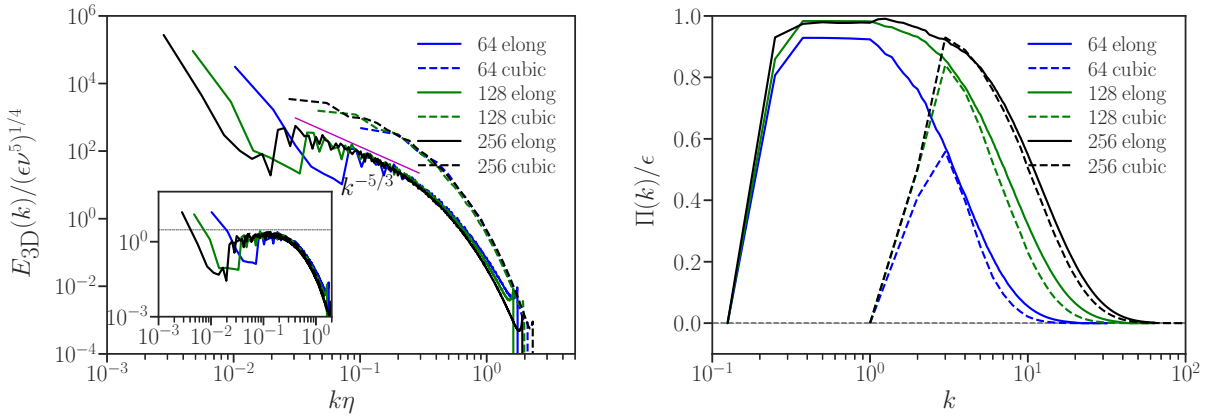

(a) (b)

Figure A.4: Time-averaged, normalized, 3D energy and energy-flux spectra at steady states. (a) Energy spectra normalized by dissipation $(\epsilon\nu^5)^{1/4}$ with wave numbers normalized by Kolmogorov length scale η. Since the spectra corresponding to the simulations in the two domain types almost perfectly overlap, the spectra of the cubic cases are multiplied by 10. (b) Energy-flux spectra normalized by dissipation rate ϵ. The inset in (a) shows compensated spectra $k^{5/3}\epsilon^{-2/3}E_{3D}(k)$.

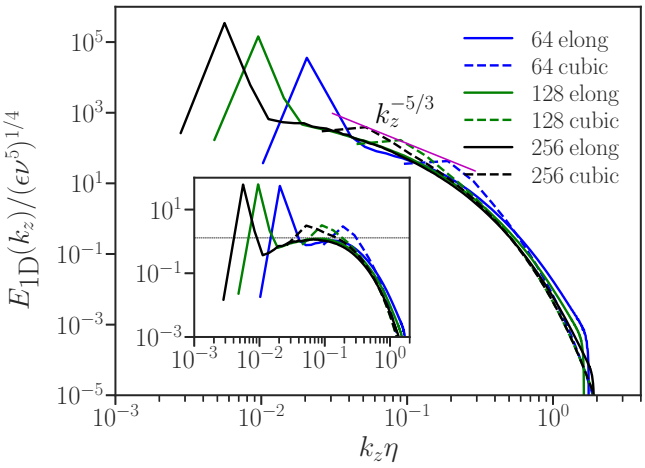

Figure A.5: Time-averaged, normalized, 1D (along the z-direction) energy spectra at steady states. Energy is normalized by dissipation $(\epsilon\nu^5)^{1/4}$ and k_z is normalized by Kolmogorov length scale η. The inset shows compensated spectra $k_z^{5/3}\epsilon^{-2/3}E_{1D}(k_z)$.

High-order quantities

In this subsection, we investigate small-scale behavior by high-order quantities of longitudinal velocity increment.

In Fig. A.6(a) and (b), we present respectively skewness and flatness factor of increments of u_z in the z-direction. The skewness and flatness factor are defined as

$$\begin{aligned} S_{zz}(r_z) &= \frac{\left\langle \left(u_z\left(\boldsymbol{x}+r_z\boldsymbol{e_z}\right)-u_z(\boldsymbol{x})\right)^3\right\rangle}{\left\langle \left(u_z\left(\boldsymbol{x}+r_z\boldsymbol{e_z}\right)-u_z(\boldsymbol{x})\right)^2\right\rangle^{3/2}}, \\ F_{zz}(r_z) &= \frac{\left\langle \left(u_z\left(\boldsymbol{x}+r_z\boldsymbol{e_z}\right)-u_z(\boldsymbol{x})\right)^4\right\rangle}{\left\langle \left(u_z\left(\boldsymbol{x}+r_z\boldsymbol{e_z}\right)-u_z(\boldsymbol{x})\right)^2\right\rangle^2}, \end{aligned} \tag{A.6}$$

where $\boldsymbol{e_z}$ is the unit vector in the z-direction and $\langle\bullet\rangle$ denotes a volume average. In all cases, at large scales, the skewness is close to zero, which is the Gaussian value. The flatness factors at large scales are slightly smaller than the Gaussian value 3 in cubic domains but somewhat larger than 3 in elongated fields. For the dissipation scales, the absolute values of both skewness and flatness factors in the elongated systems are substantially larger than those in cubic domains. Sec. A.3.1 shows that differences in small-scale structures are minor among six cases if we consider a second-order quantity (energy spectra). Indeed, all spectra closely

collapse using Kolmogorov variable. However, third- and fourth-order quantities are fairly different. Fig. A.6 indicates that the presence of large transverse motion in an elongated domain can affect the smallest scales and increase the intermittency of the flow, as also observed in the wind-tunnel experiments [136].

Subsequently, we investigate the relation between high-order quantities of the longitudinal velocity gradient $\frac{\partial u_z}{\partial z}$ and Reynolds number. Theoretically, skewness and flatness factors of $\frac{\partial u_z}{\partial z}$ are $\lim_{r_z \to 0} S_{zz}(r_z)$ and $\lim_{r_z \to 0} F_{zz}(r_z)$. For numerical simulations, these values can be approximated by skewness and flatness factor of velocity increments of the two closest points in the z-direction. Fig. A.7 presents the relation between $-S$, F and Taylor-scale Reynolds number for cubic cases, mixed and traditional Taylor-scale Reynolds number for elongated cases. We compare our results with numerical and experimental results from the literature. Hill proposed $-S \sim 0.26\mathrm{Re}_\lambda^{0.11}$ and $F \sim 1.36\mathrm{Re}_\lambda^{0.31}$ for the relation between skewness and flatness factor of longitudinal velocity gradient and Taylor-scale Reynolds number [157]. Gylfason showed that $-S \sim 0.33\mathrm{Re}_\lambda^{0.09}$ and $F \sim 0.91\mathrm{Re}_\lambda^{0.39}$ fitted their experimental data [158]. These empirical formulas are plotted in Fig. A.7, compared with the numerical results of Ishihara [159] and our simulations. We find that our data is in good agreement with previous experimental and simulation results if the mixed definition $\mathrm{Re}_\lambda^{\mathrm{mix}}$ is used. These results confirm thereby the experimental observations that turbulence forced at large streamwise scales (on numerically, in elongated domains) and turbulence allows to build up larger intermittency at the small scales.

A.3.2 Free-decaying turbulence

After reaching the steady state, we remove the external force from the system. We designate the moment when the removal of force commences as time $t = 0$. And the time is normalized by the characteristic time τ defined in Sec. A.3.1 evaluated at $t = 0$. If a comparison is to be made, the decay over time in these numerical simulations corresponds to the decay over distance downstream of the turbulence-generating source in wind-tunnel experiments.

Fig. A.8(a) shows the time evolution of energy normalized by its initial value ($E_0 \equiv E(t = 0)$) in free-decaying cases. In cubic domains, turbulence can be considered isotropic. Thus the mixed Taylor-scale Reynolds number equals the traditional Taylor-scale Reynolds number in cubic cases. Fig. A.8(b) shows the time evolution of mixed Taylor-scale Reynolds numbers in free-decaying cases. The decay of energy and mixed Taylor-scale Reynolds numbers in cubic

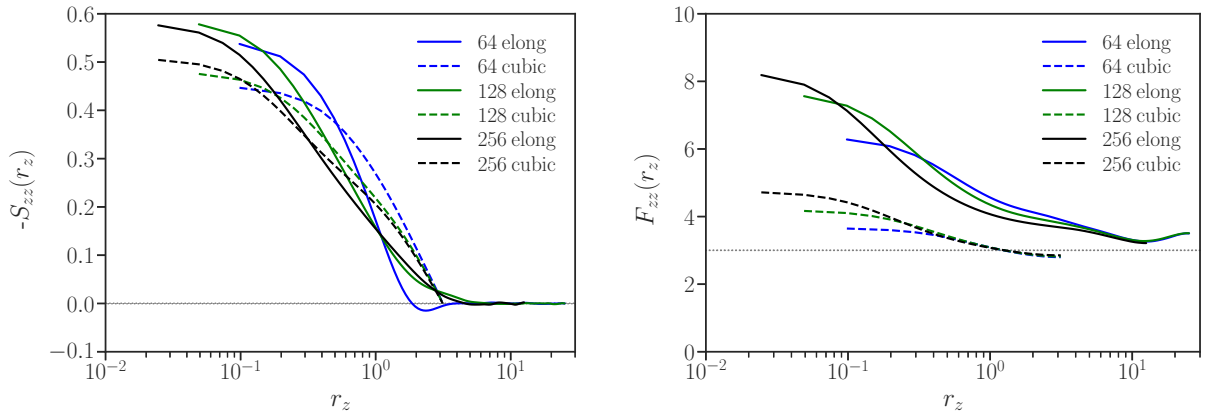

(a) (b)

Figure A.6: High-order quantities of increment of longitudinal velocity (u_z) in the z-direction at steady states. (a) Skewness. (b) Flatness factor.

cases is faster compared to that in elongated cases. The reason is that the large-scale motions have a longer turnover time and thereby survive for a longer time in elongated domains.

Fig. A.9(a) shows the time evolution of 1D energy spectra (along the z-direction) of the $128^2\times1024$ case, and the inset shows compensated energy spectra with abscissa normalized by the Kolmogorov length scale. The simulation of the decaying process in the $256^2\times2048$ case is computationally demanding. Therefore, we use the $128^2\times1024$ case to investigate the long-time evolution of energy spectra. From Fig. A.9(a), we observe that the large-scale energy and inertial ranges of elongated systems persist for a long time during the decay. Fig. A.9(b) shows the time evolution of one-dimensional (along the y-direction) energy spectra and compensated energy spectra of the 128^3 case. Comparing Fig. A.9(a) and (b), we observe that, as for the statistically stationary cases, larger inertial ranges can be obtained in elongated domains, and these inertial ranges persist for a longer time than in cubic domains.

A.4 Conclusions

In this chapter, we have reported the results of direct numerical simulations of wall-free turbulence in a domain elongated in one direction, compared with turbulence in a normal cubic

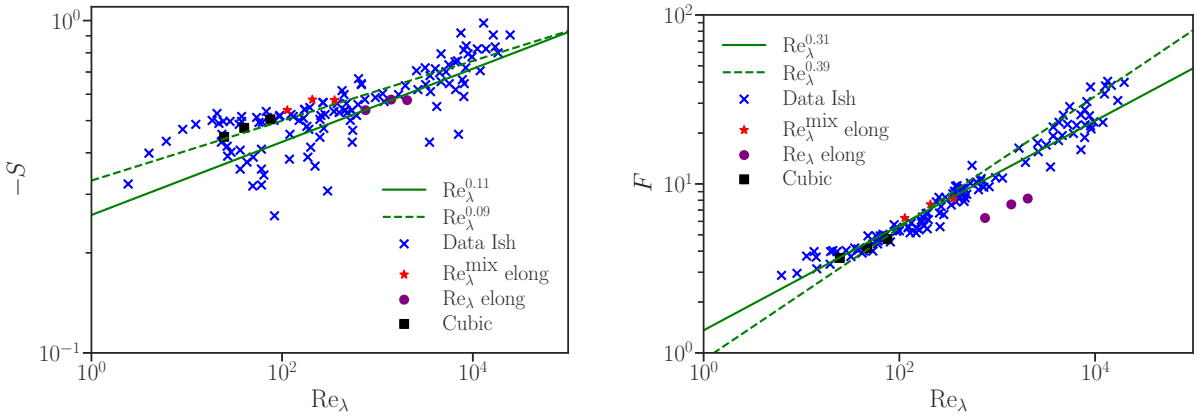

(a) (b)

Figure A.7: Relation between high-order quantities of the longitudinal velocity gradient $\frac{\partial u_z}{\partial z}$ and Taylor-scale Reynolds number. Solid and dashed lines: empirical formula. Blue crosses: numerical data from the work of Ishihara [159]. Red asterisks: data based on mixed Taylor-scale Reynolds numbers in elongated cases. Purple circles: data based on traditional Taylor-scale Reynolds numbers in elongated cases. Black squares: cubic cases. (a) Skewness. Solid line: $-S = 0.26\mathrm{Re}_\lambda^{0.11}$. Dashed line: $-S = 0.33\mathrm{Re}_\lambda^{0.09}$. (b) Flatness factor. Solid line: $F = 1.36\mathrm{Re}_\lambda^{0.31}$. Dashed line: $F = 0.91\mathrm{Re}_\lambda^{0.39}$.

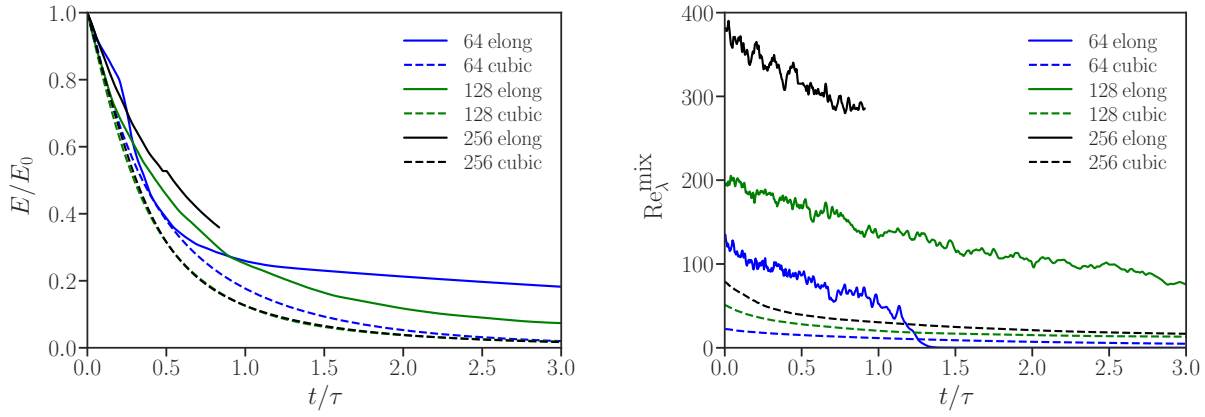

(a) (b)

Figure A.8: Time evolution of integral quantities in free-decaying cases. The time is normalized by characteristic time τ. (a) Energy normalized by its initial value. (b) Mixed Taylor-scale Reynolds numbers.

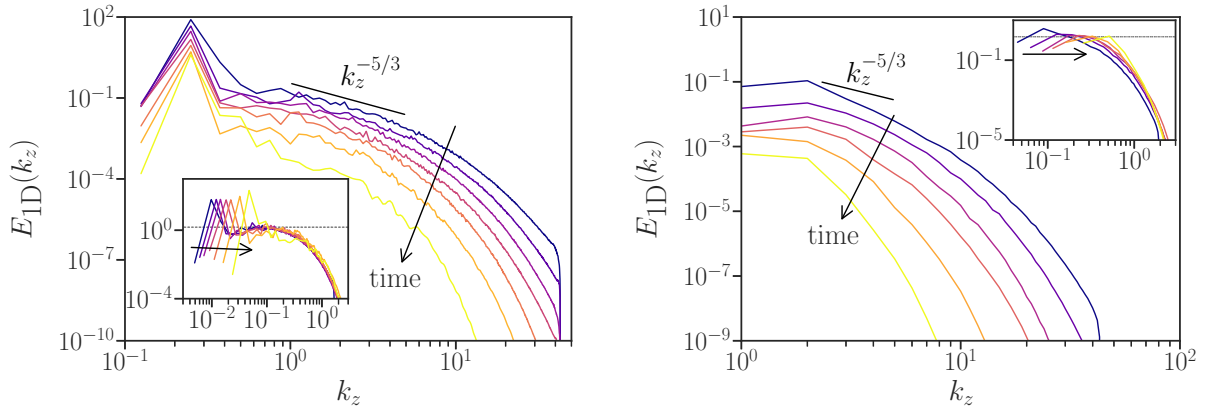

(a) (b)

Figure A.9: Time evolution of 1D energy spectra (along the y-direction) in free-decaying cases. (a) Energy spectra of the $128^2\times1024$ case at $t/\tau = 0, 1/3, 2/3, 4/3, 2, 10/3, 5$. (b) Energy spectra of the 128^3 case at $t/\tau = 0, 0.6, 1.2, 1.8, 3, 6$. The insets in (a) and (b) show compensated energy spectra $E_{1\mathrm{D}}(k_z)k_z^{5/3}\epsilon^{-2/3}$ with abscissa k_z normalized by Kolmogorov length scale η.

domain. Firstly, we added a force at large length scales and investigated turbulence at steady states. We found that large Reynolds numbers were more easily obtained in elongated domains. As a result, more extended inertial ranges and larger small-scale intermittency were observed in elongated cases. These results replicate to a certain extent what happened in recent wind-tunnel experiments [136]. Moreover, results in Sec. A.3.1 verified that whereas energy spectra at small scales collapsed using Kolmogorov variables, the high-order statistics of the smallest scales depend on the Reynolds number and agree with observations in Ref. [159]. Secondly, when the force was removed, and turbulence decays freely, large-scale structures and inertial ranges persist longer in elongated domains than in cubic domains.

An interesting outcome of the present investigation is that higher Reynolds number turbulence is obtained for a relatively low computational cost. However, this method has the disadvantage that the turbulence is highly anisotropic at the largest scales.

Bibliography

[1] J. C. Wyngaard. Atmospheric turbulence. *Annu. Rev. Fluid Mech.*, 24(1):205–234, 1992.

[2] P. W. Nasmyth. *Oceanic turbulence*. PhD thesis, University of British Columbia, 1970.

[3] S. A. Thorpe. *An introduction to ocean turbulence*, volume 10. Cambridge University Press Cambridge, 2007.

[4] K. Subramanian. Can the turbulent galactic dynamo generate large-scale magnetic fields? *Mon. Notices Royal Astron. Soc.*, 294(4):718–728, 1998.

[5] P. Spalart and S. Allmaras. A one-equation turbulence model for aerodynamic flows. In *30th aerospace sciences meeting and exhibit*, page 439, 1992.

[6] R. J. Stevens and C. Meneveau. Flow structure and turbulence in wind farms. *Annu. Rev. Fluid Mech.*, 49:311–339, 2017.

[7] P. Milan, M. Wächter, and J. Peinke. Turbulent character of wind energy. *Phys. Rev. Lett.*, 110(13):138701, 2013.

[8] B. M. Sumer and D. R. Fuhrman. *Turbulence in coastal and civil engineering*, volume 51. World Scientific, 2020.

[9] L. F. Richardson. *Weather prediction by numerical process*. University Press, 1922.

[10] A. N. Kolmogorov. The local structure of turbulence in incompressible viscous fluid for very large Reynolds numbers. *Dokl. Akad. Nauk. SSSR*, 30:301, 1941.

[11] L. Onsager. Statistical hydrodynamics. *Il Nuovo Cimento*, 6:279, 1949.

[12] R. H. Kraichnan. Intermittency in the very small scales of turbulence. *Phys. Fluids*, 10:2080, 1967.

[13] H. Tennekes and J. L. Lumley. *A first course in turbulence*. The MIT Press, 1972.

[14] P. A. Davidson. *Turbulence: An Introduction for Scientists and Engineers*. Oxford University Press, 2004.

[15] G. I. Taylor. The spectrum of turbulence. *Proc. Roy. Soc. Lond. A*, 164:476, 1938.

[16] T. Leung, N. Swaminathan, and P. A. Davidson. Geometry and interaction of structures in homogeneous isotropic turbulence. *J. Fluid Mech.*, 710:453–481, 2012.

[17] P. L. Johnson. Energy transfer from large to small scales in turbulence by multiscale nonlinear strain and vorticity interactions. *Phys. Rev. Lett.*, 124(10):104501, 2020.

[18] M. Carbone and A. D. Bragg. Is vortex stretching the main cause of the turbulent energy cascade? *J. Fluid Mech.*, 883, 2020.

[19] P. E. Hamlington, J. Schumacher, and W. J. A. Dahm. Local and nonlocal strain rate fields and vorticity alignment in turbulent flows. *Phys. Rev. E*, 77(2):026303, 2008.

[20] D. Buaria, A. Pumir, and E. Bodenschatz. Self-attenuation of extreme events in Navier-Stokes turbulence. *Nat. Commun.*, 11(1):1–7, 2020.

[21] G. L. Eyink. Locality of turbulent cascades. *Physica D: Nonlinear Phenomena*, 207(1-2):91–116, 2005.

[22] K. K. Nomura and G. K. Post. The structure and dynamics of vorticity and rate of strain in incompressible homogeneous turbulence. *J. Fluid Mech.*, 377:65–97, 1998.

[23] U. Frisch, A. Pomyalov, I. Procaccia, and S. Ray. Turbulence in noninteger dimensions by fractal Fourier decimation. *Phys. Rev. Lett.*, 108(7):074501, 2012.

[24] L. Biferale, S. Musacchio, and F. Toschi. Inverse energy cascade in three-dimensional isotropic turbulence. *Phys. Rev. Lett.*, 108(16):164501, 2012.

[25] A. Alexakis. Helically decomposed turbulence. *J. Fluid Mech.*, 812:752, 2017.

[26] R. H. Kraichnan. An almost-Markovian Galilean-invariant turbulence model. *J. Fluid Mech.*, 47:513, 1971.

[27] S. B. Pope. *Turbulent Flows*. Cambridge University Press, 2000.

[28] U. Frisch. *Turbulence, the legacy of A.N. Kolmogorov*. Cambridge University Press, 1995.

[29] M. Lesieur. *Turbulence in fluids: stochastic and numerical modelling*, volume 488. Nijhoff Boston, MA, 1987.

[30] R. Stepanov, F. Plunian, M. Kessar, and G. Balarac. Systematic bias in the calculation of spectral density from a three-dimensional spatial grid. *Phys. Rev. E*, 90(5):053309, 2014.

[31] L. Fang. Background scalar-level anisotropy caused by low-wave-number truncation in turbulent flows. *Phys. Rev. E*, 95(3):033102, 2017.

[32] A. Alexakis and L. Biferale. Cascades and transitions in turbulent flows. *Phys. Rep.*, 2018.

[33] J. C. André and M. Lesieur. Influence of helicity on the evolution of isotropic turbulence at high Reynolds number. *J. Fluid Mech.*, 81:187, 1977.

[34] C. Cambon and L. Jacquin. Spectral approach to non-isotropic turbulence subjected to rotation. *J. Fluid Mech.*, 202:295–317, 1989.

[35] F. Waleffe. The nature of triad interactions in homogeneous turbulence. *Phys. Fluids A: Fluid Dynamics*, 4(2):350–363, 1992.

[36] Q. Chen, S. Chen, and G. L. Eyink. The joint cascade of energy and helicity in three-dimensional turbulence. *Phys. Fluids*, 15(2):361–374, 2003.

[37] T. Wu, L. Fang, and Z. Wang. Exact time scale of energy exchange in triad interactions of homogeneous isotropic turbulence. *Phys. Fluids*, 33(3):035136, 2021.

[38] J. R. Herring. Approach of axisymmetric turbulence to isotropy. *Phys. Fluids*, 17(5):859–872, 1974.

[39] T. D. Lee. On some statistical properties of hydrodynamical and magnetohydrodynamical fields. *Q. Appl. Math*, 10:69, 1952.

[40] R. H. Kraichnan. Helical turbulence and absolute equilibrium. *J. Fluid Mech.*, 59:745, 1973.

[41] R. H. Kraichnan. Inertial ranges in two-dimensional turbulence. *Phys. Fluids*, 10(7):1417–1423, 1967.

[42] U. Frisch, A. Pouquet, J. Léorat, and A. Mazure. Possibility of an inverse cascade of magnetic helicity in magnetohydrodynamic turbulence. *J. Fluid Mech.*, 68(4):769–778, 1975.

[43] D. Fyfe and D. Montgomery. High-beta turbulence in two-dimensional magnetohydrodynamics. *J. Plasma Phys.*, 16(2):181–191, 1976.

[44] V. Shukla, S. Fauve, and M. Brachet. Statistical theory of reversals in two-dimensional confined turbulent flows. *Phys. Rev. E*, 94(6):061101, 2016.

[45] J. Zhu, W. Yang, and G. Zhu. Purely helical absolute equilibria and chirality of (magneto) fluid turbulence. *J. Fluid Mech.*, 739:479–501, 2014.

[46] A. van Kan, A. Alexakis, and M. Brachet. Geometric microcanonical theory of two-dimensional truncated Euler flows. *Philosophical Transactions of the Royal Society A*, 380(2226):20210049, 2022.

[47] J. J. Moreau. Constantes d'un îlot tourbillonnaire en fluide parfait barotrope. *Comptes rendus hebdomadaires des séances de l'Académie des sciences*, 252:2810–2812, 1961.

[48] H. K. Moffatt. The degree of knottedness of tangled vortex lines. *J. Fluid Mech.*, 35(1):117–129, 1969.

[49] V. Borue and S. A. Orszag. Spectra in helical three-dimensional homogeneous isotropic turbulence. *Phys. Rev. E*, 55(6):7005, 1997.

[50] A. Alexakis and M. Brachet. On the thermal equilibrium state of large-scale flows. *J. Fluid Mech.*, 872:594–625, 2019.

[51] L. M. Smith and V. Yakhot. Bose condensation and small-scale structure generation in a random force driven 2D turbulence. *Phys. Rev. Lett.*, 71(3):352, 1993.

[52] G. Boffetta, A. Celani, and M. Vergassola. Inverse energy cascade in two-dimensional turbulence: deviations from Gaussian behavior. *Phys. Rev. E*, 61:R29, 2000.

[53] G. Boffetta. Energy and enstrophy fluxes in the double cascade of two-dimensional turbulence. *J. Fluid Mech.*, 589:253–260, 2007.

[54] A. van Kan and A. Alexakis. Condensates in thin-layer turbulence. *J. Fluid Mech.*, 864:490–518, 2019.

[55] Y. Yatsuyanagi, Y. Kiwamoto, H. Tomita, M. M. Sano, T. Yoshida, and T. Ebisuzaki. Dynamics of two-sign point vortices in positive and negative temperature states. *Phys. Rev. Lett.*, 94(5):054502, 2005.

[56] S. W. Seo, B. Ko, J. H. Kim, and Y. Shin. Observation of vortex-antivortex pairing in decaying 2d turbulence of a superfluid gas. *Scientific reports*, 7(1):1–8, 2017.

[57] G. Gauthier, M. T. Reeves, X. Yu, A. S. Bradley, M. A. Baker, T. A. Bell, H. Rubinsztein-Dunlop, M. J. Davis, and T. W. Neely. Giant vortex clusters in a two-dimensional quantum fluid. *Science*, 364(6447):1264–1267, 2019.

[58] Y. B. Pointin and T. S. Lundgren. Statistical mechanics of two-dimensional vortices in a bounded container. *Phys. Fluids*, 19:1459, 1976.

[59] G. L. Eyink and H. Spohn. Negative-temperature states and large-scale, long-lived vortices in two-dimensional turbulence. *J. Stat. Phys.*, 70(3):833–886, 1993.

[60] E. Caglioti, P. L. Lions, C. Marchioro, and M. Pulvirenti. A special class of stationary flows for two-dimensional Euler equations: a statistical mechanics description. Part II. *Commun. Math. Phys.*, 174:229–260, 1995.

[61] M. K. H. Kiessling and J. L. Lebowitz. The micro-canonical point vortex ensemble: beyond equivalence. *Lett. Math. Phys.*, 42:43–56, 1997.

[62] R. Robert and J. Sommeria. Statistical equilibrium states for two-dimensional flows. *J. Fluid Mech.*, 229:291, 1991.

[63] J. Miller. Statistical mechanics of Euler equations in two dimensions. *Phys. Rev. Lett.*, 65:2137–2140, 1990.

[64] G. Joyce and D. Montgomery. Negative temperature states for the two-dimensional guiding center plasma. *J. Plasma Phys.*, 10:107, 1973.

[65] D. Montgomery and G. Joyce. Statistical mechanics of "negative temperature" states. *Phys. Fluids*, 17:1139, 1974.

[66] D. Montgomery, W. H. Matthaeus, W. T. Stribling, D. Martinez, and S. Oughton. Relaxation in two dimensions and the "sinh-Poisson" equation. *Phys. Fluids A*, 4:3, 1992.

[67] D. Montgomery, X. Shan, and W. H. Matthaeus. Navier–Stokes relaxation to Sinh–Poisson states at finite Reynolds numbers. *Phys. Fluids A: Fluid Dynamics*, 5(9):2207–2216, 1993.

[68] T. P. Billam, M. T. Reeves, B. P. Anderson, and A. S. Bradley. Onsager-Kraichnan condensation in decaying two-dimensional quantum turbulence. *Phys. Rev. Lett.*, 112(14):145301, 2014.

[69] D. H. E. Dubin and T. M. O'Neil. Two-dimensional guiding-center transport of a pure electron plasma. *Phys. Rev. Lett.*, 60(13):1286, 1988.

[70] F. Bouchet and A. Venaille. Statistical mechanics of two-dimensional and geophysical flows. *Phys. Rep.*, 515:227, 2012.

[71] B. Gallet and R. Ferrari. The vortex gas scaling regime of baroclinic turbulence. *Proc. Natl. Acad. Sci.*, 117(9):4491–4497, 2020.

[72] J. G. Esler and T. L. Ashbee. Universal statistics of point vortex turbulence. *J. Fluid Mech.*, 779:275–308, 2015.

[73] R. Robert and J. Sommeria. Relaxation towards a statistical equilibrium state in two-dimensional perfect fluid dynamics. *Phys. Rev. Lett.*, 69(19):2776, 1992.

[74] D. Ter Haar. *Elements of thermostatistics*, volume 1. Holt, Rinehart and Winston, 1966.

[75] T. W. David, L. Zanna, and D. P. Marshall. Eddy-mixing entropy and its maximization in forced-dissipative geostrophic turbulence. *J. Stat. Mech. Theory Exp.*, 2018(7):073206, 2018.

[76] M. S. Singh and M. E. O'Neill. The climate system and the second law of thermodynamics. *Rev. Mod. Phys.*, 94(1):015001, 2022.

[77] N. Leprovost, B. Dubrulle, and P. H. Chavanis. Dynamics and thermodynamics of axisymmetric flows: Theory. *Phys. Rev. E*, 73:046308, 2006.

[78] S. Thalabard, B. Dubrulle, and F. Bouchet. Statistical mechanics of the 3D axisymmetric Euler equations in a Taylor–Couette geometry. *J. Stat. Mech.*, 2014(1):P01005, 2014.

[79] B. Qu, W. J. T. Bos, and A. Naso. Direct numerical simulation of axisymmetric turbulence. *Phys. Rev. Fluids*, 2:094608, 2017.

[80] R. Monchaux, F. Ravelet, B. Dubrulle, A. Chiffaudel, and F. Daviaud. Properties of steady states in turbulent axisymmetric flows. *Phys. Rev. Lett.*, 96:124502, 2006.

[81] R. H. Kraichnan and D. Montgomery. Two-dimensional turbulence. *Rep. Prog. Phys.*, 43:547, 1980.

[82] R. V. Abramov and A. J. Majda. Statistically relevant conserved quantities for truncated quasigeostrophic flow. *Proc. Natl. Acad. Sci.*, 100(7):3841–3846, 2003.

[83] A. Delache, C. Cambon, and F. Godeferd. Scale by scale anisotropy in freely decaying rotating turbulence. *Phys. Fluids*, 26(2):025104, 2014.

[84] N. E. L. Haugen and A. Brandenburg. Inertial range scaling in numerical turbulence with hyperviscosity. *Phys. Rev. E*, 70(2):026405, 2004.

[85] U. Frisch, S. Kurien, R. Pandit, W. Pauls, S.S. Ray, A. Wirth, and J.-Z. Zhu. Hyperviscosity, Galerkin truncation and bottlenecks in turbulence. *Phys. Rev. Lett.*, 101:144501, 2008.

[86] V. Borue and S. A. Orszag. Forced three-dimensional homogeneous turbulence with hyperviscosity. *Europhys. Lett.*, 29:687, 1995.

[87] M. Rivera and X. L. Wu. External dissipation in driven two-dimensional turbulence. *Phys. Rev. Lett.*, 85(5):976, 2000.

[88] V. Borue. Inverse energy cascade in stationary two-dimensional homogeneous turbulence. *Phys. Rev. Lett.*, 72:1475, 1994.

[89] W. J. T. Bos and J. P. Bertoglio. Large scale bottleneck effect in two-dimensional turbulence. *J. Turbul.*, 10:N30, 2009.

[90] S. Chen, G. D. Doolen, R. H. Kraichnan, and Z. She. On statistical correlations between velocity increments and locally averaged dissipation in homogeneous turbulence. *Phys. Fluids A: Fluid Dynamics*, 5(2):458–463, 1993.

[91] L. P. Wang, S. Chen, J. G. Brasseur, and J. C. Wyngaard. Examination of hypotheses in the Kolmogorov refined turbulence theory through high-resolution simulations. Part 1. Velocity field. *J. Fluid Mech.*, 309:113–156, 1996.

[92] T. Wu and W. J. T. Bos. Statistical mechanics of the Euler-equations without vortex stretching. *J. Fluid Mech.*, 929, 2021.

[93] R. Salmon. *Lectures on geophysical fluid dynamics*. Oxford University Press, 1998.

[94] S. Thalabard. *Contributions to the statistical mechanics of ideal two and a half dimensional flows*. PhD thesis, Université Paris Sud-Paris XI, 2013.

[95] C. Cichowlas, P. Bonaïti, F. Debbasch, and M. Brachet. Effective dissipation and turbulence in spectrally truncated Euler flows. *Phys. Rev. Lett.*, 95:264502, 2005.

[96] W. J. T. Bos and J. P. Bertoglio. Dynamics of spectrally truncated inviscid turbulence. *Phys. Fluids*, 18:071701, 2006.

[97] W. J. T. Bos. Three-dimensional turbulence without vortex stretching. *J. Fluid Mech.*, 915:A121, 2021.

[98] T. Wu and W. J. T. Bos. Cascades of enstrophy and helicity in turbulence without vortex stretching. *Phys. Rev. Fluids*, 7:094601, 2022.

[99] C. E. Leith. Diffusion approximation for two-dimensional turbulence. *Phys. Fluids*, 11(3):671–672, 1968.

[100] R. H. Kraichnan. Inertial-range transfer in two- and three-dimensional turbulence. *J. Fluid Mech.*, 47:525, 1971.

[101] T. Ishihara, K. Morishita, M. Yokokawa, A. Uno, and Y. Kaneda. Energy spectrum in high-resolution direct numerical simulations of turbulence. *Phys. Rev. Fluids*, 1:082403, 2016.

[102] A. G. Lamorgese, D. A. Caughey, and S. B. Pope. Direct numerical simulation of homogeneous turbulence with hyperviscosity. *Phys. Fluids*, 17(1):015106, 2005.

[103] U. Frisch, M. Lesieur, and P. L. Sulem. Crossover dimensions for fully developed turbulence. *Phys. Rev. Lett.*, 37(19):1312, 1976.

[104] U. Frisch, A. Pomyalov, I. Procaccia, and S. Ray. Turbulence in noninteger dimensions by fractal Fourier decimation. *Phys. Rev. Lett.*, 108(7):074501, 2012.

[105] A. S. Lanotte, R. Benzi, S. K. Malapaka, F. Toschi, and L. Biferale. Turbulence on a fractal Fourier set. *Phys. Rev. Lett.*, 115(26):264502, 2015.

[106] G. Sahoo, A. Alexakis, and L. Biferale. Discontinuous transition from direct to inverse cascade in three-dimensional turbulence. *Phys. Rev. Lett.*, 118(16):164501, 2017.

[107] Z. Qin, A. Naso, and W. J. T. Bos. Transition from axisymmetric to three-dimensional turbulence. *J. Turbul.*, pages 1–16, 2021.

[108] D. Buaria and A. Pumir. Nonlocal amplification of intense vorticity in turbulent flows. *Phys. Rev. Research*, 3(4):L042020, 2021.

[109] A. van Kan and A. Alexakis. Critical transition in fast-rotating turbulence within highly elongated domains. *J. Fluid Mech.*, 899, 2020.

[110] Franck Plunian, Andrei Teimurazov, Rodion Stepanov, and Mahendra Kumar Verma. Inverse cascade of energy in helical turbulence. *Journal of Fluid Mechanics*, 895, 2020.

[111] L. Biferale, S. Musacchio, and F. Toschi. Split energy–helicity cascades in three-dimensional homogeneous and isotropic turbulence. *J. Fluid Mech.*, 730:309–327, 2013.

[112] L. M. Smith and V. Yakhot. Finite-size effects in forced two-dimensional turbulence. *J. Fluid Mech.*, 274:115, 1994.

[113] M. Chertkov, C. Connaughton, I. Kolokolov, and V. Lebedev. Dynamics of energy condensation in two-dimensional turbulence. *Phys. Rev. Lett.*, 99:084501, 2007.

[114] S. Musacchio and G. Boffetta. Condensate in quasi-two-dimensional turbulence. *Phys. Rev. Fluids*, 4(2):022602, 2019.

[115] H. Xia, D. Byrne, G. Falkovich, and M. Shats. Upscale energy transfer in thick turbulent fluid layers. *Nat. Phys.*, 7(4):321–324, 2011.

[116] F. Bouchet and E. Simonnet. Random changes of flow topology in two-dimensional and geophysical turbulence. *Phys. Rev. Lett.*, 102(9):094504, 2009.

[117] L. M. Smith and F. Waleffe. Transfer of energy to two-dimensional large scales in forced, rotating three-dimensional turbulence. *Phys. Fluids*, 11(6):1608–1622, 1999.

[118] B. Gallet. Exact two-dimensionalization of rapidly rotating large-Reynolds-number flows. *Journal of Fluid Mechanics*, 783:412–447, 2015.

[119] H. K. Moffatt. On the suppression of turbulence by a uniform magnetic field. *J. Fluid Mech.*, 28:571, 1967.

[120] A. Alexakis. Two-dimensional behavior of three-dimensional magnetohydrodynamic flow with a strong guiding field. *Phys. Rev. E*, 84(5):056330, 2011.

[121] W. Agoua, B. Favier, A. Delache, A. Briard, and W. J. T. Bos. Spontaneous generation and reversal of helicity in anisotropic turbulence. *Phys. Rev. E*, 103(6):L061101, 2021.

[122] L. Biferale, M. Buzzicotti, and M. Linkmann. From two-dimensional to three-dimensional turbulence through two-dimensional three-component flows. *Phys. Fluids*, 29(11):111101, 2017.

[123] J. Chai, T. Wu, and L. Fang. Single-scale two-dimensional-three-component generalized-Beltrami-flow solutions of incompressible Navier-Stokes equations. *Phys. Lett. A*, 384(34):126857, 2020.

[124] Z. Qin, H. Faller, B. Dubrulle, A. Naso, and W. J. T. Bos. Transition from non-swirling to swirling axisymmetric turbulence. *Phys. Rev. Fluids*, 5(6):064602, 2020.

[125] P. D. Mininni, D. Rosenberg, R. Reddy, and A. Pouquet. A hybrid MPI–OpenMP scheme for scalable parallel pseudospectral computations for fluid turbulence. *Parallel computing*, 37(6-7):316–326, 2011.

[126] R. H. Kraichnan. Statistical dynamics of two-dimensional flow. *J. Fluid Mech.*, 67(1):155–175, 1975.

[127] L. F. G. Simmons and C. Salter. Experimental investigation and analysis of the velocity variations in turbulent flow. *Proceedings of the Royal Society of London. Series A, Containing Papers of a Mathematical and Physical Character*, 145(854):212–234, 1934.

[128] G. K. Batchelor. *The theory of homogeneous turbulence*. Cambridge University Press, 1953.

[129] G. Comte-Bellot and S. Corrsin. The use of contraction to improve the isotropy of grid-generated turbulence. *J. Fluid Mech.*, 25:657–682, 1966.

[130] M. S. Mohamed and J. C. LaRue. The decay power law in grid-generated turbulence. *J. Fluid Mech.*, 219:195–214, 1990.

[131] H. Makita. Realization of a large-scale turbulence field in a small wind tunnel. *Fluid Dyn. Res.*, 8(1-4):53, 1991.

[132] L. Mydlarski. A turbulent quarter century of active grids: from Makita (1991) to the present. *Fluid Dyn. Res.*, 49(6):061401, 2017.

[133] L. Mydlarski and Z. Warhaft. On the onset of high-Reynolds-number grid-generated wind tunnel turbulence. *J. Fluid Mech.*, 320:331–368, 1996.

[134] R. J. Hearst and P. Lavoie. The effect of active grid initial conditions on high Reynolds number turbulence. *Exp. Fluids*, 56:1–20, 2015.

[135] K. P. Griffin, N. J. Wei, E. Bodenschatz, and G. P. Bewley. Control of long-range correlations in turbulence. *Exp. Fluids*, 60:1–14, 2019.

[136] L. Neuhaus, M. Holling, W. J. T. Bos, and J. Peinke. Generation of atmospheric turbulence with unprecedentedly large Reynolds-number in a wind tunnel. *Phys. Rev. Lett.*, Accepted, 2020.

[137] L. Chevillard, B. Castaing, E. Lévêque, and A. Arneodo. Unified multifractal description of velocity increments statistics in turbulence: Intermittency and skewness. *Phys. D*, 218:77, 2006.

[138] A. N. Kolmogorov. The local structure of turbulence in incompressible viscous fluid for very large Reynolds numbers. *Cr Acad. Sci. URSS*, 30:301–305, 1941.

[139] A. N. Kolmogorov. A refinement of previous hypotheses concerning the local structure of turbulence in a viscous incompressible fluid at high Reynolds number. *J. Fluid Mech.*, 13:82, 1962.

[140] Z. S. She and E. Leveque. Universal scaling laws in fully developed turbulence. *Phys. Rev. Lett.*, 72:336, 1994.

[141] B. Dubrulle. Intermittency in fully developed turbulence: Log-Poisson statistics and generalized scale covariance. *Phys. Rev. Lett.*, 73(7):959, 1994.

[142] C. Meneveau and K. R. Sreenivasan. The multifractal nature of turbulent energy dissipation. *J. Fluid Mech.*, 224:429–484, 1991.

[143] R. Friedrich and J. Peinke. Description of a turbulent cascade by a Fokker-Planck equation. *Phys. Rev. Lett.*, 78(5):863, 1997.

[144] H. E. Cekli, R. Joosten, and W. van de Water. Stirring turbulence with turbulence. *Phys. Fluids*, 27(12):125107, 2015.

[145] R. E. G. Poorte and A. Biesheuvel. Experiments on the motion of gas bubbles in turbulence generated by an active grid. *J. Fluid Mech.*, 461:127–154, 2002.

[146] M. Avila, D. Barkley, and B. Hof. Transition to turbulence in pipe flow. *Annu. Rev. Fluid Mech.*, 55:575–602, 2023.

[147] P. Moin and J. Kim. Numerical investigation of turbulent channel flow. *J. Fluid Mech.*, 118:341–377, 1982.

[148] J. C. Del Alamo and J. Jiménez. Spectra of the very large anisotropic scales in turbulent channels. *Phys. Fluids*, 15(6):L41–L44, 2003.

[149] K. C. Kim and R. J. Adrian. Very large-scale motion in the outer layer. *Phys. Fluids*, 11(2):417–422, 1999.

[150] N. Hutchins and I. Marusic. Evidence of very long meandering features in the logarithmic region of turbulent boundary layers. *J. Fluid Mech.*, 579:1–28, 2007.

[151] X. M. Zhai and P. K. Yeung. Evolution of anisotropy in direct numerical simulations of MHD turbulence in a strong magnetic field on elongated periodic domains. *Phys. Rev. Fluids*, 3(8):084602, 2018.

[152] J. M. TenBarge, G. G. Howes, W. Dorland, and G. W. Hammett. An oscillating Langevin antenna for driving plasma turbulence simulations. *Comput. Phys. Commun.*, 185(2):578–589, 2014.

[153] C. Dhandapani and G. Blanquart. From isotropic turbulence in triply periodic cubic domains to sheared turbulence with inflow/outflow. *Phys. Rev. Fluids*, 5(12):124605, 2020.

[154] T. Pestana and S. Hickel. Rossby-number effects on columnar eddy formation and the energy dissipation law in homogeneous rotating turbulence. *J. Fluid Mech.*, 885:A7, 2020.

[155] A. van Kan and A. Alexakis. Energy cascades in rapidly rotating and stratified turbulence within elongated domains. *J. Fluid Mech.*, 933:A11, 2022.

[156] K. Alvelius. Random forcing of three-dimensional homogeneous turbulence. *Phys. Fluids*, 11:1880–1889, 1999.

[157] R. J. Hill. Scaling of acceleration in locally isotropic turbulence. *J. Fluid Mech.*, 452:361, 2002.

[158] A. Gylfason, S. Ayyalasomayajula, and Z. Warhaft. Intermittency, pressure and acceleration statistics from hot-wire measurements in wind-tunnel turbulence. *J. Fluid Mech.*, 501:213–229, 2004.

[159] T. Ishihara, Y. Kaneda, M. Yokokawa, K. Itakura, and A. Uno. Small–scale statistics in high–resolution direct numerical simulation of turbulence: Reynolds number dependence of one–point velocity gradient. *J. Fluid Mech.*, 592:335, 2007.